Phenomenology of Thermally produced Dark matter

Parampreet Singh Walia

2018

Thesis submitted for the degree of Philosophiæ Doctor

Series of dissertations submitted to the
Faculty of Mathematics and Natural Sciences, University of Oslo
No. 2037

ISSN 1501-7710

Cover: Hanne Baadsgaard Utigard.
Print production: Reprosentralen, University of Oslo.

Abstract

In this thesis, we perform a systematic scrutinization of various well-known attributes of thermal dark matter (DM) models. Part of this thesis is focused on the development of efficient and computationally less intensive methods for testing various dark matter scenarios.

Cosmic Microwave Background (CMB) observations help us constrain the amount of various particle species very precisely, thus requiring an equally accurate theoretical prediction. We provide a simple yet highly efficient method for estimating the leading radiative corrections to the annihilation cross section of Majorana DM.

The paramount significance of self-interacting DM (SIDM) in alleviating two of the small scale problems, cusp vs. core and too-big-to fail (TBTF) is known for quite some time in the literature. In the most common setting of SIDM, DM interacts with a light mediator via a Yukawa coupling which results in large self-scattering rates. In such a setting, the annihilation of DM also gets a strong enhancement due to the Sommerfeld effect. We discuss that the most common SIDM scenario when the mediator particle decays to Standard model particles is strongly constrained by the data.

A decay of mediator particles to some relativistic dark species is still allowed and such a scenario can solve cusp vs. core and TBTF problems. We show that the missing satellites problem can also be solved in this setting due to the efficient scattering of DM with the relativistic dark species.

Processes like on-resonance Sommerfeld annihilation and DM decay result in a decreasing comoving number density of DM. We for the first time provide model independent constraints on such scenarios using a Boltzmann solver. We have thus tested one of the basic assumptions in the ΛCDM cosmology of a constant comoving DM number density by using the latest CMB data from Planck and low-redshift measurements of the Hubble rate and normalization of the matter power spectrum.

Acknowledgments

The work in this thesis has been possible due to immense support of several people. To my supervisor, Torsten Bringmann, thank you for your research insights, guidance and tremendous support throughout this research. The discussions with you have not only been intellectually stimulating but our meetings have always rejuvenated my enthusiasm and motivation. I really appreciate your willingness to meet me at short notice every time and going through drafts of my thesis, despite your busy schedule.

I would also like to thank Ahmad Galea, Håvard Tveit Ihle, Jörn Kersten, Felix Kahlhoefer and Kai Schmidt-Hoberg for joyful collaborations, without you guys this work would have been impossible. And to Andrzej Jan Hryczuk, thanks for always being available for interesting discussions.

To Walia and Arora families, thank you for your invaluable love and support and my brother Jaspreet for always sending happy thoughts and memes. I would also like to thank my grandfather whose role in my life was, and remains, immense. And to Siddhartha and Rikesh, who have been wonderful friends to me over the years. A special thanks to Sanjana Arora, who in the course of my Ph.D. became my best friend and wife. Thanks for your unwavering support and patience. Lastly, thank you Gucci (our furry baby) for jumping around and giving me company and enthusiasm during the late nights that resulted in this work.

List of publications

The thesis is based on the following publications:

Paper I T. Bringmann, A. J. Galea and P. Walia, "Leading QCD Corrections for Indirect Dark Matter Searches: a Fresh Look", *Phys Rev.* **D93** (2015) 043529, arXiv:1510.02473 [hep-ph]

Paper II T. Bringmann, H. T. Ihle, J. Kersten and P. Walia, "Suppressing structure formation at dwarf galaxy scales and below: late kinetic decoupling as a compelling alternative to warm dark matter", *Phys Rev.* **D94** (2016) 103529, arXiv:1603.04884 [hep-ph]

Paper III T. Bringmann, F. Kahlhoefer, K. Schimdt-Hoberg and P. Walia, "Strong constraints on self-interacting dark matter with light mediators", *Phys Rev.* **L118** (2017) 141802, arXiv:1612.00845 [hep-ph]

Paper IV T. Bringmann, F. Kahlhoefer, K. Schimdt-Hoberg and P. Walia, "Converting non-relativistic dark matter to radiation", *Phys Rev.* **D98** (2018) 023543, arXiv:1803.03644 [astro-ph]

Contents

Abstract iii

Acknowledgments v

List of Publications vii

I Background 1

1 Introduction 3

2 Dark matter 7

2.1 Evidence for Dark Matter 7

2.2 General constraints on dark matter candidates 9

2.3 Detection methods 10

3 ΛCDM cosmology 13

3.1 Background universe 13

3.2 Perturbed universe 16

3.3 Successes and challenges to the ΛCDM paradigm 19

3.3.1 Small scale problems of ΛCDM 21

3.3.2 Low-redshift data and CMB 22

II Dynamics I: Chemical freeze out 25

4 Solving the Boltzmann equation 27

4.1 Equilibrium thermodynamics 27

4.2 Relic density calculation 29

5 Relic density of thermal dark matter **33**
5.1 Freeze out of thermal dark matter 33
5.2 Co-annihilations 37

III Dynamics II: Full thermal decoupling **41**

6 Kinetic decoupling **43**
6.1 Kinetic decoupling temperature 44
6.2 Kinetic decoupling and structure formation 47

IV Discussion of results **49**

7 Efficient treatment of QCD corrections for Majorana dark matter **51**
7.1 Outline 51
7.2 Lifting of helicity suppression 53
7.3 Efficient treatment of QCD radiative corrections 57
7.4 Impact of QCD corrections on relic density 60

8 SIDM and small scale problems in ΛCDM **65**
8.1 Outline 65
8.2 SIDM interactions 67
8.2.1 Annihilation: $\chi\chi \to \tilde{\gamma}\tilde{\gamma}$ 67
8.2.2 Self-scatterings: $\chi\chi \to \chi\chi$ 73
8.2.3 Scattering with a relativistic partner: $\chi\tilde{\gamma} \to \chi\tilde{\gamma}$ 76
8.3 Discussion 80

9 Cosmological constraints on non-standard dark matter evolution **85**
9.1 Outline 85
9.2 Phenomenological approach to varying comoving DM density . . 88
9.3 Method and data 92
9.4 Discussion 93

10 Summary **103**

V Papers **129**

Paper I **131**

Paper II **155**

Paper III **181**

Paper IV **189**

Part I

Background

Chapter 1

Introduction

It is now well established through various observations that most of the matter in the universe is non-luminous and interacts with the Standard model (SM) mainly via gravitational interactions. The observed distribution of cosmic structures [1,2], Cosmic Microwave Background (CMB) [3,4] and gravitational lensing [5,6] are very hard to explain if we do not include a non-relativistic and non-luminous component.

The CMB experiments have helped us to know the content of the universe very precisely. According to the most recent measurement by Planck [4], SM particle content constitutes only about 15% of the total matter in the universe. The remaining 85% is still elusive to the experiments till date and is termed as *Dark Matter* (DM). 'Dark' because it does not interact with photons and 'Matter' because it influences the visible structure through gravitation like any other ordinary matter. $N-$body simulations of the large scale structure [7,8] also demonstrate that a significant amount of the DM in the universe has to be non-relativistic during structure formation. This class of non-relativistic DM is referred to as *Cold Dark Matter* (CDM) in the literature [9].

The most commonly considered mechanism for DM production in the early universe is that of *thermal production*, which can naturally provide the observed DM relic abundance with weak-scale interactions [10]. One assumes DM to be in thermal equilibrium with the ordinary matter at very early times. After the DM annihilation rate drops below the expansion rate, DM *chemically* decouples from the plasma and the comoving density of DM becomes constant. After chemical decoupling, DM is still kept in kinetic equilibrium through elastic scatterings with

the heat bath particles. DM completely decouples from the plasma when the scattering rate also falls behind the Hubble rate and this epoch is referred to as *kinetic decoupling*.

The CMB observations constrain the amount of DM to a percent level accuracy [4]. We thus require an equally accurate theoretical prediction. Inclusion of radiative corrections can alter the relic density prediction of a model considerably [11, 12]. In this thesis, we will provide an efficient method to calculate the radiative corrections to the annihilation rate of a Majorana DM.

On large scales, our universe is well described by the *cosmological concordance* model or more commonly referred to as the ΛCDM model [13]. The model consists of five components: baryons, photons, neutrinos, CDM and a cosmological constant Λ. Moreover, DM is assumed to be collisionless in the ΛCDM paradigm. Though the model is very successful in explaining the structure of the universe on large scales, there are some discrepancies between observations and the $N-$body simulations on the sub-Mpc scales [14]. The observed discrepancies have various astrophysical solutions within the ΛCDM paradigm [14]. Alternatively, these problems can also be addressed by efficient self-scattering of DM [15]. In this thesis, we will consider the latter possibility.

A common assumption in cosmology is that the comoving DM number density remains constant after chemical freeze out. Scenarios in which DM can decay [16–19] or have large enhancements to the annihilation cross section [20] are some of the exceptions to this assumption. Such scenarios result in a modified cosmic history and thus can be constrained by using cosmological data such as CMB. The problem with constraining such scenarios is that one has to solve the cosmic evolution on a model to model basis. In this thesis, we will motivate an efficient and model independent way of constraining such scenarios.

The thesis is organized into five parts as follows. Some of the background knowledge for this thesis is briefly discussed in **Part I**. In chapter 2, we motivate the general constraints on a DM particle through discussion of some astrophysical and cosmological pieces of evidence. In chapter 3, we give an overview of the ΛCDM model. In **Part II**, we focus on the calculation of the DM relic abundance. In chapter 4, we will give a brief derivation of the Boltzmann equation for describing the number density evolution of a particle species. In chapter 5, we will use the equation to calculate the DM relic abundance for the scenarios relevant to this thesis. In **Part III**, we will discuss kinetic decoupling of DM and discuss its impact

on structure formation. **Part IV** discusses the results of the publications which form the basis of this thesis. In chapter 7, we will discuss an efficient treatment of radiative corrections for a Majorana DM (based on paper I [21]). Chapter 8 is dedicated to the solution of small-scale problems of structure formation through self-scattering DM scenarios (based on papers II [22] and III [23]). In chapter 9, we motivate a model independent way of constraining a changing comoving DM density scenario (based on paper IV [24]). We summarize our findings in chapter 10. The four publications which the thesis is based on are included in **Part V**.

Chapter 2

Dark matter

DM has now become an essential ingredient for the understanding of our universe. In section 2.1, we will discuss some of the astrophysical and cosmological pieces of evidence for DM. In section 2.2, we will discuss some of the general constraints on a DM particle. In section 2.3, we will discuss some of the detection methods for unveiling the particle nature of DM. As a detailed discussion is beyond the scope of this thesis, we refer the interested reader to [10] for a pedagogical review on DM.

2.1 Evidence for Dark Matter

From kinematics of stars and galaxies: Though today the most credible pieces of evidence for DM come from cosmology, the first hints for DM to be the dominant form of matter actually came from astrophysics as early as the 1920s. In 1922, astronomer James Jeans studied the vertical motion of stars in the galactic plane and concluded that there should be at least 'two dark stars to each bright star' to explain the large velocities that he observed [25]. A decade later in 1932, J.H. Oort also studied the stars in the galactic plane and corroborated that the velocities of the stars were too large for the stars to have been gravitationally bound by the visible mass [26]. In the subsequent year, Fritz Zwicky, who is usually credited to discover DM, measured the velocity dispersion in the Coma cluster. He concluded that in order to hold the galaxies in the cluster there must be huge amounts of *invisible* mass in the cluster [27].

It was not until the 1970s that the idea of DM gained the interest of the physics community. In late 70s, it was discovered by Vera Rubin (and her collaborators)

that at large distances from the galactic center, the circular velocity of stars becomes independent of the distance from the center [28, 29]. According to Newtonian dynamics, one expects the circular velocity at distance r from the center to be

$$v_c = \sqrt{\frac{GM(r)}{r}}\,, \tag{2.1}$$

where G is the Gravitational constant and $M(r)$ is the mass inside the radius r. Thus, beyond the visible disk one will expect v_c to decrease as $r^{-1/2}$. The observation of flattening of the velocities can be explained if there is non-luminous matter with the mass scaling as $M(r) \propto r$. This gave rise to the idea of the visible galaxies being embedded in much larger DM *halos*.

From Gravitational lensing: Gravitational potential generated by a massive object bends the path of the light passing close to it and this phenomenon is called Gravitational lensing. The optical and gravitational lensing measurements are thus complementary approaches to probe the mass of an astrophysical object. The most compelling astrophysical evidence for DM comes from the cluster merging system, 1E0657-558 or the *Bullet* Cluster [5, 6]. The gravitational lensing analysis showed that most of the mass of the two colliding clusters went through with its distribution unaffected after the collision, whereas the X-ray measurements showed a displaced center of mass of the two clusters w.r.t the lensing measurements. This implies that the visible mass is a small fraction of the total mass of the clusters and thus is a clear evidence of DM. As the DM passed through with its distribution unaffected, implies that DM does not interact strongly with either the visible gas or itself.

CMB and Baryon Acoustic Oscillations: In the early universe, baryons and photons were tightly coupled through Thompson scattering and acted as a single fluid. The pressure exerted by this fluid does not let the perturbations in the baryons to grow but exhibit an oscillatory behavior called Baryon Acoustic Oscillations (BAO) [30].[1]

At high temperatures, the formation of *stable* neutral atoms cannot take place as they are disintegrated instantaneously. With the universe cooling down due to expansion, there comes a time when the electrons and nuclei can combine to form neutral atoms. As the photons do not scatter efficiently with the neutral atoms,

[1] Gravity makes the fluid fall in a gravitational well and pressure tries to push it outward.

photons decouple from the plasma at this low temperature and the epoch is known as *recombination*. The CMB photons that we observe today are these primordial photons from the surface of last scattering.

BAOs result in overdense and underdense regions and can be seen as the oscillatory behavior in the CMB and the Matter power spectrum (MPS). Baryons and DM have distinct effects on the CMB and the MPS (see for example [31]). Measurement of the BAO scale from the large scale surveys [32–36] and the CMB measurements [4] provide complementary handles on the total baryon and DM density. The values inferred from these two types of measurements are remarkably consistent. We will state the observed densities in the next chapter but we should note that today CMB is the most robust piece of evidence for DM which fixes the amount of DM to a percent level accuracy.

From the observed large scale structure: If DM is indeed the dominant part of the matter in the universe, it will definitely influence the structure formation in the universe. Comparison of $N-$body simulations [7, 8, 37–40] to the actual measurements [1, 2] shows that the structure in the universe could only have been formed if a substantial amount of non-relativistic DM is present.

2.2 General constraints on dark matter candidates

The general constraints on a DM particle candidate are—

- **Electrically neutral:** DM has to be electrically neutral or have an extremely small fractional charge [41] in order to be *dark* as compared to the ordinary baryonic matter.

- **Non-baryonic:** The observations of Bullet cluster, CMB, BAO and primordial nucleosynthesis [42] imply that DM needs to be non-baryonic.

- **Stable:** A DM particle has to be stable on cosmological timescales. If it were to decay, it will have significant effects on the cosmology and thus stringent limits exist on DM decay rate (see for example [43] and paper IV [24]).

- **Non-relativistic:** The $N-$body simulations are consistent with the measurements only if the dominant part of DM is non-relativistic at the time of

structure formation. We will see in chapter 6 that a (semi-)relativistic component will erase all the structure below its free-streaming length and thus lower limits of the order of keV can be put on the mass of DM [44, 45].

In addition to the above general constraints, the amount of DM in the universe should also match with the inferred value from the CMB experiments *at least* around recombination. In chapter 9, we will discuss the *time-dependence* of this constraint.

As we can see none of the SM particles can satisfy all the above constraints, thus DM is a *Beyond the* SM (BSM) particle. There are many proposed candidates and particle theories and we refer the reader to [46] for a nice classification of many DM candidates according to the above constraints. In this thesis, we will only focus on *Weakly Interacting Massive Particles* (WIMPs). As the name suggests, typical WIMP interactions are of electroweak strength and have mass of the order of electroweak scale. In chapter 7, we will consider a specific WIMP candidate, the neutralino which is the most often considered DM candidate in Supersymmetry (SUSY) [47]. In the rest of the thesis, our treatment of a WIMP particle will be quite general.

Another important BSM particle species that we will consider in this thesis is the dark radiation (DR). Like DM, DR will have highly suppressed interactions with the photons and thus remains dark. However, it will be relativistic unlike DM. A common example of DR is the sterile neutrino, i.e. right-handed neutrinos [48]. In chapters 8 and 9, we will see that interactions in the dark sector due to this relativistic component can have profound effects on cosmology and astrophysics.

2.3 Detection methods

The particle nature of DM can be probed if it interacts (except through gravitation) with the SM at some level or if it is itself self-interacting. If DM is self-interacting, it can have an effect on the astrophysical structures [49] and we will discuss the case in much more detail in chapters 8 and 9. There are three kinds of ways for detecting DM through interactions with SM. We will now give a brief overview of the three methods and we refer the reader to [50] for a recent review on the status of WIMP DM —

Direct searches: *Direct* detection is based on the idea of detecting nuclear recoils after scattering with DM [51]. For a WIMP of mass $100\,\mathrm{GeV}$, there is an expected flux of $\sim 10^9\,\mathrm{m}^{-2}\mathrm{s}^{-1}$ of DM on earth [52]. Despite the large flux, the nuclear recoils will be very small in the $1 - 100\,\mathrm{keV}$ range due to the very small cross sections [53]. Thus, direct detection experiments have to be very sensitive and are set up underground to avoid the cosmic ray background.

There have previously been claims of a DM detection by CoGeNT [54] and CRESST [55] experiments, which have disappeared with time. Currently, there are two detection signals by DAMA/ LIBRA [56] and CDMS II [57] experiments which are still there and are in conflict with the other experiments. We refer the reader to [53] for a recent review of the current constraints from direct detection experiments.

Indirect searches: *Indirect* searches use astronomical observations to detect primary or secondary annihilation and decay products of DM such as gamma rays, neutrinos and cosmic rays. The annihilation (decay) rate of DM is proportional to the second (first) power of the DM density. Thus, an ideal region to look for the annihilation/decay products is with large DM density and has small astrophysical backgrounds. We refer the reader to [58] for a recent review on the current constraints from various indirect detection experiments.

Collider searches: In *collider* searches, one of the ways to detect a BSM particle is to look for events with missing transverse energies. With a detection of a BSM particle in collider searches, we cannot be sure if the discovered particle is indeed the DM. This is because we cannot know the lifetime or the relic abundance of the discovered particle. The Large Hadron collider (LHC) is now running at Center of Mass (COM) energy of $13\,\mathrm{TeV}$ and the two detectors ATLAS [59] and CMS [60] are extensively collecting data. At the time of writing this thesis, there has not been a detection of a BSM particle. A non-detection results in stringent constraints on model parameters in a considered model framework. We refer the reader to [61] for the recent status of LHC searches.

Chapter 3

ΛCDM cosmology

As mentioned in chapter 1, the ΛCDM model describes the universe very well on large scales. In section 3.1, we will give a brief overview of the spacetime geometry and the dynamics of the constituents in the ΛCDM model. In section 3.2, we will derive the perturbation equations which we will later use for an extension of the ΛCDM model in chapter 9. In section 3.3, we will give an overview of the some of the excellent agreements and discrepancies of the ΛCDM model's predictions with the observations.

3.1 Background universe

A spatially homogeneous, isotropic and expanding (or contracting) universe can be described by the Friedmann Lemaître Robertson Walker (FLRW) metric [62–64], with the line element given by

$$ds^2 = -dt^2 + a(t)^2 \left[\frac{dr^2}{1 - Kr^2} + r^2 d\theta^2 + r^2 \sin^2\theta d\phi^2 \right] , \tag{3.1}$$

where $a(t)$ is the scale factor which describes the spatial expansion and K is a constant that describes the curvature of the universe, with the flat universe given by $K = 0$. The current measurements [3,4] are consistent with the universe being flat and we will assume $K = 0$ for this thesis. For a flat universe, the above equation in Cartesian coordinates is

$$ds^2 = -dt^2 + a(t)^2 \left[dx^2 + dy^2 + dz^2 \right] . \tag{3.2}$$

The scale factor is a free parameter and can be fixed at any reference time. In this thesis, we will set the value of a today as one, i.e. $a(t_0) = 1$. For an expanding universe, this means $a < 1$ at earlier times. It is also common to consider cosmological redshift (z) as a measure of time and is related to the scale factor as $a \equiv 1/(1+z)$. We will use redshift and the scale factor inter-changeably in this thesis.

In this chapter, we will use the Einstein summation convention and Latin indices to denote spatial coordinates. The *physical* distance between two points is dependent on the time of measurement, i.e. $r^P(t) = a(t)\, r = a(t)\sqrt{\delta_{ij}\Delta x^i \Delta x^j}$.

The coordinates x, y, z in the above line-element are known as the *comoving* coordinates and the comoving distance is defined as $r^c \equiv r = \sqrt{\delta_{ij}\Delta x^i \Delta x^j}$. In analogy to comoving spatial coordinates, we can define *conformal* time (τ) as

$$d\tau \equiv dt/a\,. \tag{3.3}$$

In this thesis, we will use a dot (dash) over a variable to denote a derivative w.r.t proper (conformal) time, i.e $\dot{a} \equiv da/dt$ and $a' \equiv da/d\tau$. For measuring the rate of expansion, one defines the *Hubble* parameter (H) as

$$H(a) \equiv \frac{\dot{a}}{a}\,. \tag{3.4}$$

We can also define a conformal Hubble rate as

$$\mathcal{H}(a) \equiv \frac{a'}{a} = aH\,. \tag{3.5}$$

With the coordinate basis (τ, x, y, z), the FLRW metric now becomes square of scale factor times the Minkowski metric $(\eta_{\mu\nu})$

$$ds^2 = a^2(\tau)[-d\tau^2 + \delta_{ij}dx^i dx^j] = a^2(\tau)\eta_{\mu\nu}\,. \tag{3.6}$$

For a perfect fluid with energy density ρ and pressure P, the dynamics described by the Einstein equations for the above metric is described by the two Friedmann equations (see for example [65])

$$H^2 = \frac{8\pi G}{3}\rho\,, \tag{3.7}$$

$$\dot{H} = -\frac{3\pi G}{3}(\rho + 3P)\,, \tag{3.8}$$

where G is the Newton's gravitational constant. Equations 3.7 and 3.8 can be combined to get the following evolution of ρ

$$\dot{\rho} = -3H(1+w)\rho\,, \tag{3.9}$$

where we have defined $w \equiv P/\rho$. In the ΛCDM model the various components can be divided into three categories according to the value of w—

- $w \sim 1/3$: This corresponds to the relativistic components, i.e. photons (γ) and (at early times) the SM neutrinos (ν). These components are collectively referred to as *radiation*. Using equation 3.9, we have $\rho_r \propto a^{-4}$ for such components.

- $w \ll 1$: The non-relativistic components constitute this category, i.e. CDM(χ) and the baryons(b) and are collectively called *matter* in cosmology. For such components we have $\rho_m \propto a^{-3}$. At late times, neutrinos also become non-relativistic and hence contribute as a matter component.

- $w = -1$: This is the vacuum component and has a constant energy density $\rho_\Lambda \equiv \dfrac{3\Lambda}{8\pi G}$, where Λ is called the *cosmological constant*. The Λ term results in an accelerating expansion at late times.

In the literature, there are two common terminologies that are used when referring to the energy densities of species X. Firstly, the *comoving density* is defined as $\rho_X a^{3(1+w_X)}$.[1] Secondly, the relative density of a component is given in terms of the *density parameter* Ω defined as

$$\Omega_X \equiv \frac{\rho_X}{\rho_c} = \frac{8\pi G\rho_X}{3H^2}\,, \tag{3.10}$$

where $\rho_c \equiv \frac{3H^2}{8\pi G}$ is the *critical density* of the universe. In this thesis, unless otherwise stated, we will use Ω_X to denote the density parameter today. Using equation 3.7, we can find the relation between the expansion rate and the energy densities of various species. For the ΛCDM model (assuming relativistic neutrinos), we have

$$H(a) = 100h\sqrt{\Omega_\Lambda + (\Omega_b + \Omega_\chi)a^{-3} + (\Omega_\gamma + \Omega_\nu)a^{-4}}\,, \tag{3.11}$$

[1] Note that if there is no net creation or destruction of a species, with our choice of fixing the scale factor $a_0 = 1$, the comoving density is the density today. This is the case in the ΛCDM model. In chapter 9, we will consider the case when the comoving density of a species changes.

where h is defined as $h \equiv \dfrac{H_0}{100\,\mathrm{km/s/Mpc}}$.

We will now qualitatively discuss the different eras of cosmic history relevant for this thesis. The fit of a ΛCDM model to the CMB data helps us to know the values of the above parameters very precisely: $\Omega_\Lambda \sim 0.69$, $\Omega_b h^2 \sim 0.022$, $\Omega_\chi h^2 \sim 0.12$, $\Omega_\gamma h^2 \sim 2.5 \times 10^{-5}$ and at early times $\Omega_\nu \sim 0.7\,\Omega_\gamma$ [3, 4]. The above values tell us that the universe has been dominated by the Λ component from redshift 0.3 and the relative contribution of Λ will increase in the future. For redshifts larger than 0.3, matter components dominate until the redshift $\lesssim 3400$. Before $z \gtrsim 3400$, it is the radiation components that dominated the universe. The time at which radiation and matter contribute equally to the expansion of universe is called *matter-radiation equality*. The decoupling of photons from the plasma, i.e. recombination occurs around $z_{\rm rec} \sim 1100$ [3, 4]. For the case of thermal DM that we will consider in this thesis, chemical and kinetic decoupling will occur deep in the radiation dominated regime (see [44, 45] or paper II [22]).

The dark radiation (DR) that we described in the previous chapter is not a part of the vanilla ΛCDM model. In cosmology, such a DR component is usually quantified in terms of additional neutrino degrees of freedom as

$$\Delta N_{\rm eff} = \frac{\rho_{\rm DR}}{\rho_{1\nu}}\,, \tag{3.12}$$

where $\rho_{1\nu}$ is the energy of one neutrino species. CMB measurements put strong constraints on the amount of DR at recombination, $\Delta N_{\rm eff} \lesssim 0.4$ [4].

3.2 Perturbed universe

The universe described by equation 3.6, describes a completely homogeneous and isotropic universe. Such a metric cannot result in the cosmic structure we observe in the universe today. From the observation of the anisotropies in CMB, we know that at the time of photon decoupling, the inhomogeneities in the universe were very small, about one part in 10^5 [66]. We thus make a modification to the above metric and introduce small inhomogeneities

$$g_{\mu\nu} = a^2(\tau)[\eta_{\mu\nu} + h_{\mu\nu}(\tau, \mathbf{x})]\,, \tag{3.13}$$

where $a^2(\tau)h_{\mu\nu}(\tau, \mathbf{x})$ is the small *perturbation* to the metric dependent on both space and time coordinates and $a^2(\tau)\eta_{\mu\nu}$ is the *background* part dependent only on time. The other quantities of interest can also be divided into a background part and a perturbation. The perturbed energy and momentum tensor is given by (see for example [30])

$$T_{\mu\nu} = (\rho + P)u_\mu u_\nu + P g_{\mu\nu} + \Pi_{\mu\nu}\,, \tag{3.14}$$

where u_μ is the four velocity and $\Pi_{\mu\nu}$ is the anisotropic stress [67]. Note that $\Pi_{\mu\nu}$ is a perturbation, i.e. a first order quantity. Whereas ρ, p and u_μ contain a background as well as a perturbation part–

$$\rho \equiv \bar{\rho} + \delta\rho\,, \qquad P \equiv \bar{P} + \delta P\,, \tag{3.15}$$

$$u_\mu \equiv a(-1, \mathbf{v}) \quad \text{and} \quad u^\mu = a^{-1}(1, \mathbf{v})\,, \tag{3.16}$$

where $\delta\rho$, δP and $\mathbf{v}$ are the perturbations to the background quantities $\bar{\rho}$, $\bar{P}$ and four-velocity $\bar{u}_\mu \equiv (-a, \mathbf{0})$, respectively. In this section we will denote the background quantities with an overhead bar to distinguish them from the perturbed quantities.

In general, a perturbation can be divided into a sum of scalar, vector and tensor parts [30]. The vector parts decay in time, i.e. become smaller in magnitude [30]. The scalar and tensor parts can oscillate or grow in time. In this thesis, we will only consider scalar perturbations. Moreover, in this section we will derive the expressions that will be used in chapter 9. A detailed discussion of cosmological perturbations is beyond the scope of this thesis and we refer the reader to Ref. [30] for a pedagogical discussion.

Our way of defining the perturbations is not unique, by making an infinitesimal coordinate transformation we can change the value of the perturbation. Whereas, the background quantity will by definition only depend on the background conformal time τ. The observables cannot be dependent on our choice of coordinates. This problem is cured by fixing the *gauge*, i.e. the time slicing and computing the gauge invariant variables. There is no unique choice to fix the gauge and it can be convenient to do a particular calculation in a specific gauge. In this thesis (more specifically chapter 9), we use the *synchronous gauge* [68]. In synchronous

gauge, the perturbed line element of the FRW metric is given by [68]

$$ds^2 = g_{\mu\nu}dx^\mu dx^\nu = a^2\left[-\mathrm{d}\tau^2 + (\delta_{ij} + h_{ij})dx^i dx^j\right] . \tag{3.17}$$

We can now calculate the dynamics by using the conservation of energy-momentum tensor $\nabla_\nu T^{\mu\nu} = 0$, where ∇_ν denotes the covariant derivative.

In this thesis, we are primarily interested in the perturbative analysis in the situation when $w'_X = 0$, i.e. a particle is either non-relativistic or ultra-relativistic. This assumption also implies $\delta p = w\delta\rho$ for isentropic fluids [68]. Assuming $w' = 0$ and keeping only the zeroth and first order terms, we calculate the covariant derivatives for isentropic fluids to be

$$a^2\nabla_\nu T^{0\nu} = \bar{\rho}\delta' + [\bar{\rho}' + 3\mathcal{H}(1+w)\bar{\rho}](1+\delta) + (1+w)\bar{\rho}\left(\theta + \frac{h'}{2}\right) , \tag{3.18}$$

$$a^2\partial_i(\nabla_\nu T^{i\nu}) = (1+w)\bar{\rho}\theta' + (1+w)(\bar{\rho}' + 4\mathcal{H}\bar{\rho})\theta + w\bar{\rho}\nabla^2\delta + \frac{2}{3}\nabla^4\Pi , \tag{3.19}$$

where we have defined the conventional perturbation variables $h \equiv h_{ii}$, $\delta \equiv \delta\rho/\rho$, $\theta \equiv \partial_i v^i$ and $\Pi_{ij} \equiv (\partial_i\partial_j - \frac{\delta_{ij}}{3}\nabla^2)\Pi$.[2]

In the scenario when the different particle species are decoupled from each other, we can use $\nabla_\nu T^{\mu\nu}_X = 0$ even for individual particles. The background part of equation 3.18 in this case is $\bar{\rho}'_X + 3\mathcal{H}\bar{\rho}_X(1+w_X) = 0$, which is the same as equation 3.9. In section 9.2, we will consider a scenario when a particle species converts to another species resulting in a different evolution of the densities.

The observable related to the density perturbations is the matter power spectrum $P(k)$, defined in terms of the correlation function of the density contrasts δ as [65]

$$\langle\delta(\mathbf{x_1})\delta(\mathbf{x_2})\rangle \equiv \int_0^\infty \frac{d^3k}{(2\pi)^3} e^{i\mathbf{k}\cdot(\mathbf{x_1}-\mathbf{x_2})} P(k) . \tag{3.20}$$

For describing the large scale structure, an often used parametrization in the literature is that of σ_8, which is rms fluctuation in matter in a sphere of radius

[2] We hope that the use of same conventional symbol h for describing the metric perturbations and the Hubble rate today does not create confusion for the reader. Except this section and section 9.2, $h = \frac{H_0}{100\,\mathrm{km/s/Mpc}}$ is used consistently in this thesis.

$R_8 \equiv 8h^{-1}\,\mathrm{Mpc}$ and is related to the power spectrum as [65]

$$\sigma_8^2 = \int_0^\infty \frac{dk}{2\pi^2} k^2 P(k) \left(\frac{3j_1(kR_8)}{kR_8} \right)^2 , \tag{3.21}$$

where j_1 is the first spherical Bessel function.

The anisotropies in the CMB background are also described by the perturbative analysis we just presented. They are conventionally described by angular power spectrum C_ℓ, which is defined by the correlation of temperature anisotropies δT in two directions $\hat{\mathbf{n}}$ and $\hat{\mathbf{n}}'$ on the surface of last scattering [65]

$$\left\langle \frac{\delta T(\hat{\mathbf{n}})}{T} \frac{\delta T(\hat{\mathbf{n}}')}{T} \right\rangle \equiv \sum_\ell \frac{2\ell+1}{4\pi} C_\ell P_\ell(\hat{\mathbf{n}} \cdot \hat{\mathbf{n}}') \,, \tag{3.22}$$

where ℓ are the multipoles and P_ℓ is the Legendre polynomial.

3.3 Successes and challenges to the ΛCDM paradigm

As already mentioned, the ΛCDM model is highly successful in describing the universe at large scales or equivalently at early times. In Fig. 3.1, we show the matter power spectrum for the best-fit ΛCDM model (see [2] for the details) compared with various large scale measurements. We see that there is an excellent agreement on the large scales $\gtrsim 1\,\mathrm{Mpc}$.[3] Another great success of the ΛCDM model is the high degree of agreement of the predicted CMB spectrum with the actual measurements [4]. In Fig. 3.2, we show the spectrum of the best-fit ΛCDM model (red) and the actual measurements (blue).

The ΛCDM model is described by only a set of six independent parameters. There exists multiple parametrizations with different sets of parameters (see for example [3, 69]), but in this thesis we will use the following set: Baryon density $\Omega_b h^2$, CDM density $\Omega_\chi h^2$, *approximate* angular size of the sound horizon θ_{MC}, reionization optical depth τ, logarithm of amplitude of primordial scalar curvature perturbations $\ln(10^{10} A_s)$ and the scalar spectral index n_s. We refer the reader to [70] for details about the various parameters.

[3] The lack of measurements or *interest* on very large scales ($\gtrsim 10^3\,\mathrm{Mpc}$) is due to the theoretical uncertainty, *the cosmic variance* [65].

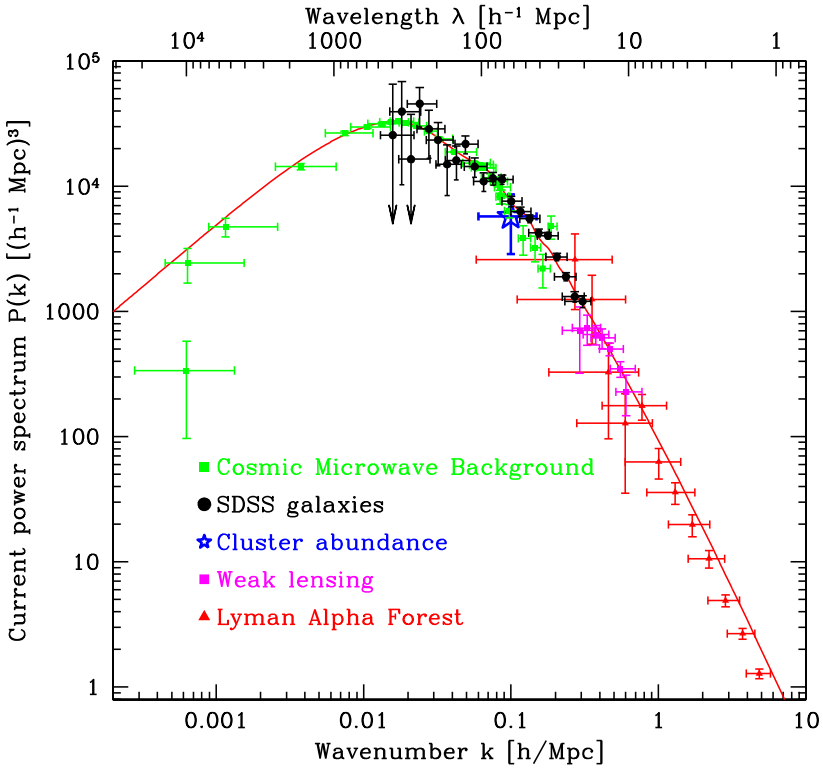

Figure 3.1: Matter power spectrum measurements from various large scale experiments. The red line is the spectrum of the best-fit ΛCDM model of [2]. Figure taken from [2].

As can be seen from Fig. 3.2, the best-fit model has a remarkable agreement with the measurement. Another success of the ΛCDM model is that the polarization spectrum obtained from the best-fit values from temperature data only agrees very well with the independently measured polarization spectrum. In this thesis, we will use the combined Planck 2015 temperature and polarization data: TTTEEE+low-P likelihood [71] and as we are going to use the best-fit values of the above parameters at multiple places in this thesis, we state the values here [4]

$$\begin{aligned} &\Omega_b h^2 = 0.02225\,, && \Omega_\chi h^2 = 0.1198\,, && 100\theta_{\rm MC} = 1.04077\,, \\ &\tau = 0.0790\,, && \ln(10^{10} A_s) = 3.094\,, && n_s = 0.9645. \end{aligned} \tag{3.23}$$

The ΛCDM prediction of BAOs also agrees quite well with the measurements at large scales [32–36].

Despite the immense success of such a simple model, there exist some dis-

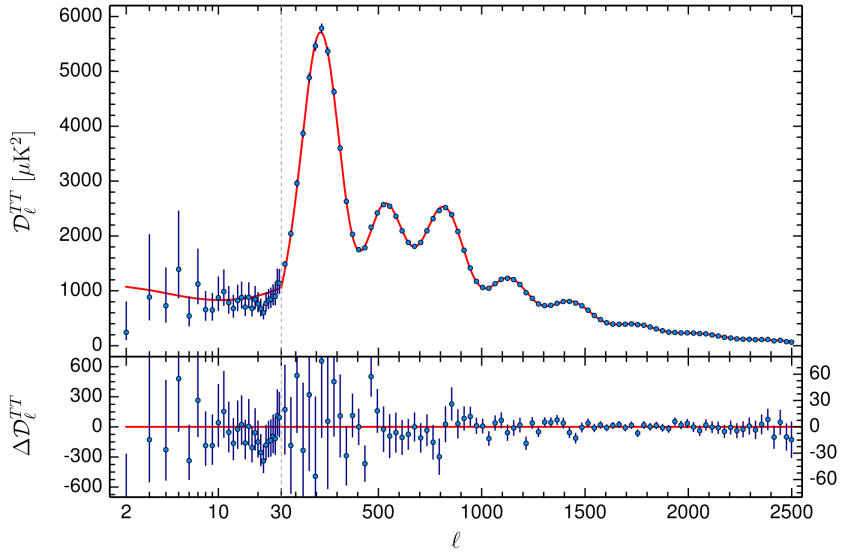

Figure 3.2: Measurement of angular power spectrum of temperature anisotropies by Planck [4] shown as blue data points. The red curve is the spectrum of the best-fit ΛCDM model obtained using the blue points as the data. Figure from [4].

crepancies and open questions that remain unanswered. We will discuss the two kinds of the discrepancies now and we refer the reader to [72] for a recent review on the discussion of current status of ΛCDM paradigm.

3.3.1 Small scale problems of ΛCDM

The ΛCDM predictions for large scale structure (> 1 Mpc) agree very nicely with the observations [2, 38, 73, 74]. At smaller (galactic) scales there exist some long standing, but not *undisputed* (see below), discrepancies between the predictions and the observations. We will now briefly discuss three of the small scale discrepancies and refer the reader to [14] for a very comprehensive review—

- **Missing Satellites:** According to $N-$body simulations of Milky Way sized halos, DM clumps should exist at all scales in the ΛCDM paradigm and we expect to see thousands of subhalos $\geq 10^7 M_\odot$ in our galaxy [40, 75–79]. The *Missing satellite* problems is that we see only ~ 50 satellite galaxies upto a mass of $\sim 300 M_\odot$ [80].

- **Cusp core problem:** The ΛCDM simulations predict the inner density profiles of small galaxies to increase steeply $\rho(r) \propto r^{-\gamma}$, with $\gamma \simeq 0.8 - 1.4$

[81, 82]. The increasing density towards the center is known as a *cusp* like profile. Though the observations suggest that the DM-dominated low-mass galaxies have more *core* like profiles with $\gamma \approx 0 - 0.5$ [83, 84].

- **Too big to fail (TBTF):** The most massive subhalos do not form galaxies but galaxies are observed in lower mass halos [85, 86]. The most massive satellites should be *too big to fail* to trigger star formation and hence be visible. This was originally observed in Milky Way, but it was subsequently also seen in Andromeda [87] and in the Local group [88].

There exist many astrophysical solutions for solving the above three problems in the ΛCDM paradigm. For example, the missing satellites can be solved if the star formation becomes inefficient for small mass subhalos (see for example [14]). Cusp-core problem can be solved if baryon feedback processes like supernova could reduce the central density (see for example [89]). The TBTF problem is harder to explain in the ΛCDM paradigm [14]. In chapter 8, we will show that the three problems can be solved by going beyond the ΛCDM paradigm, when we consider weakly self-interacting DM.

3.3.2 Low-redshift data and CMB

There also exist discrepancies of CMB and direct measurements of the Hubble rate [90] and $\sigma_8\Omega_m^\alpha$ [91–93], where $\alpha > 0$ and varies for different experiments. CMB data from Planck predicts a smaller value of $H_0 \sim 67.27\,\mathrm{km/s/Mpc}$ [4] for the ΛCDM model as compared to the most recent direct measurement of the Hubble space telescope $H_0 \sim 73.24\,\mathrm{km/s/Mpc}$ [90]. The discrepancy is about 3.4σ [90].

The best-fit value of the normalization of the matter power spectrum on the other hand has a larger value with CMB only data $\sigma_8 = 0.831 \pm 0.013$ than the direct measurements $\sigma_8(\Omega_m/0.27)^{0.3} = 0.782 \pm 0.010$ [93], which using the best-fit value of Ω_m from Planck gives $\sigma_8 \sim 0.74$.

In Fig. 3.3, we show the 1σ and 2σ constraints on H_0 and the parameters combination $\sigma_8(\Omega_m/0.27)^{0.3}$ to illustrate the discrepancy. The red contours signify the constraints from temperature and polarization data from Planck [71] and the cyan and orange bands show the direct measurements of H_0 [90] and $\sigma_8(\Omega_m/0.27)^{0.3}$ [93]. The green and blue contours are with the Planck data combined with the direct low-redshift measurements (see paper IV [24]).

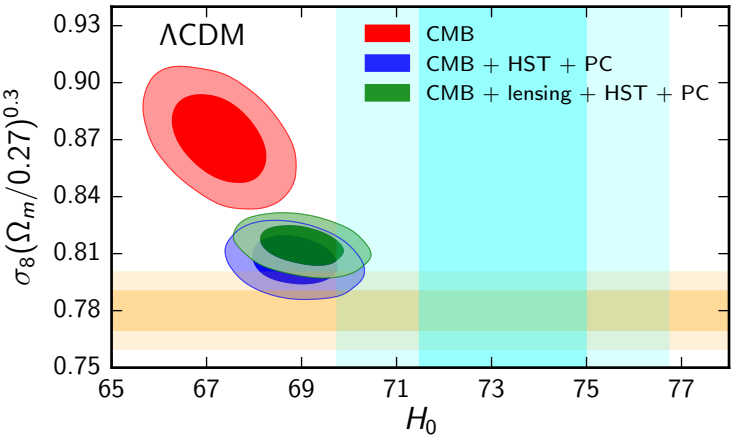

Figure 3.3: The discrepancies of the low-redshift measurements of the Hubble rate and the matter power spectrum normalization in the ΛCDM paradigm. The red contours show the 1σ and 2σ constraints on the parameters using CMB data only [71]. The cyan and orange bands show the direct measurements of the parameters from [90] and [93], respectively. The green and blue contours show the effect of combining CMB data with the the low-redshift measurements: lensing [71], Hubble space telescope (HST) [90] and Planck Clusters (PC) [93]. For details, see paper IV [24] from which the figure is taken.

Part II

Dynamics I: Chemical freeze out

Chapter 4

Solving the Boltzmann equation

In chapter 1, we stated that the comoving number density of different particle species becomes constant when their annihilation rate falls below the Hubble rate. In this chapter, we will justify this criterion by laying the mathematical framework for decoupling in an expanding universe. In the end of the chapter, we will arrive at an equation, describing the evolution of the number density of a species. First, we will start with discussing thermodynamics of particles in equilibrium. We refer the reader to [94] for a detailed derivation of the results presented in this chapter.

4.1 Equilibrium thermodynamics

In equilibrium, the phase space distribution functions (f) of bosons and fermions is described by Bose-Einstein and Fermi-Dirac statistics, respectively. For a particle at temperature T and momentum $\mathbf{p}$, it is given by

$$f(\mathbf{p}, T) = \frac{1}{e^{(E-\mu)/T} \pm 1}\,, \tag{4.1}$$

where $E = \sqrt{\mathbf{p}^2 + m^2}$ is the energy and m being the mass of the particle, μ is the chemical potential and $\pm$ is for fermions and bosons, respectively.

The number and energy density of a particle in *or out*[1] of equilibrium is ob-

[1] For particles not in equilibrium the phase space density is not given by equation 4.1.

tained by integrating f over momenta

$$n(\mathbf{x},T) = g\int \frac{d^3p}{(2\pi)^3}\, f(\mathbf{x},\mathbf{p},T)$$
$$\rho(\mathbf{x},T) = g\int \frac{d^3p}{(2\pi)^3}\, E(\mathbf{p})\, f(\mathbf{x},\mathbf{p},T) \tag{4.2}$$

where g is the internal degrees of freedom of the particle. In equilibrium, using the distribution functions from equation 4.1, we have

$$n^{\text{eq}} = \begin{cases} \frac{g}{\pi^2}\,\zeta(3)\,T^3\,, & \text{for relativistic bosons,} \\ \frac{3g}{4\pi^2}\,\zeta(3)\,T^3\,, & \text{for relativistic fermions,} \\ g\left(\frac{mT}{2\pi}\right)^{3/2} e^{(\mu-m)/T}\,, & \text{for non-relativistic bosons or fermions,} \end{cases} \tag{4.3}$$

and

$$\rho^{\text{eq}} = \begin{cases} \frac{g\pi^2}{30}\,T^4\,, & \text{for relativistic bosons,} \\ \frac{7}{8}\,\frac{g\pi^2}{30}\,T^4\,, & \text{for relativistic fermions,} \\ n^{\text{eq}}(m+\frac{3}{2}T)\,, & \text{for non-relativistic bosons or fermions.} \end{cases} \tag{4.4}$$

We will denote the equilibrium values of the quantities with a (sub-)superscript ^{eq} in this thesis. Using equation 3.9, we can also see that for relativistic species we have

$$T^{\text{eq}}_{\text{rel}} \propto a^{-1}\,. \tag{4.5}$$

The entropy density of a species with pressure P is given by

$$s = \frac{\rho - \mu n + P}{T}\,. \tag{4.6}$$

As the number density for non-relativistic particles is exponentially suppressed, the total entropy of the universe is dominated by relativistic particles and is given by

$$s_{\text{tot}} = g_{*s}\frac{2\pi^2}{45}T^3\,, \tag{4.7}$$

where

$$g_{*s} \equiv \sum_{\text{bosons}} g_i \left(\frac{T_i}{T}\right)^3 + \frac{7}{8}\sum_{\text{fermions}} g_i \left(\frac{T_i}{T}\right)^3\,, \tag{4.8}$$

where T_i is the temperature of the individual species and T is the temperature of

the thermal bath.

4.2 Relic density calculation

We now move on to the discussion of how particles fall out of equilibrium by discussing the Boltzmann equation. The Boltzmann equation governs the evolution of the phase space density of a particle species and is described by two functionals [94]

$$L[f] = C[f]\,, \tag{4.9}$$

where L is known as the Liouville operator and C as the collision operator. The Liouville operator gives the net rate of change in time of the phase space density. For a flat FRW universe, $L[f]$ is given by

$$L[f] = E(\partial_t - H\mathbf{p}\cdot\partial_{\mathbf{p}})f(\mathbf{p})\,. \tag{4.10}$$

The collision operator $C[f]$ gives the rate of change of f due to the presence of interactions. For the case of annihilations to a two-body final state, $i,j \to k,l$, $C[f_i]$ is given by[2]

$$\begin{aligned} C[f_i] \;=\; & -\frac{1}{2g_i}\int \frac{d^3p_j}{(2\pi)^3 2E_j}\,\frac{d^3p_k}{(2\pi)^3 2E_k}\,\frac{d^3p_l}{(2\pi)^3 2E_l} \\ & \times(2\pi)^4\delta^4(p_i+p_j-p_k-p_l) \\ & \times\left[|\mathcal{M}_{i,j\to k,l}|^2 f_i f_j(1\pm f_k)(1\pm f_l)\right. \\ & \left.-\,\mathcal{M}_{k,l\to i,j}|^2 f_k f_l(1\pm f_i)(1\pm f_j)\right]\,, \end{aligned} \tag{4.11}$$

where $\pm$ refers to bosons and fermions, respectively, $|\mathcal{M}|^2$ is the invariant amplitude squared of the process, summed over initial and final degrees of freedom.

We can get an equation for the evolution of the number density of species i by integrating equation 4.9 over momenta p_i. For doing so, we have to make some reasonable assumptions—

- the phase space density functions can be approximated by the Maxwell-Boltzmann distribution

[2] We have considered 2 body final state for simplicity. The final result for number density evolution will be true for any number of final particles.

- the final state particles k and l quickly go back into equilibrium with the thermal bath after being produced

- the species i and j still remain in kinetic equilibrium, though not in chemical equilibrium

- and the chemical potential of the particles is negligible.

The *principle of detailed balance* allows us to make the replacement $f_i^{\rm eq} f_j^{\rm eq} = f_k^{\rm eq} f_l^{\rm eq}$. Using *CP* invariance ($|\mathcal{M}_{i,j\to k,l}|^2 = |\mathcal{M}_{k,l\to i,j}|^2$), we can integrate equation 4.9 over momenta p_i to get a very simple equation for the evolution of the number density n_i (see [65, 94] for a detailed derivation)

$$\frac{1}{a^3}\frac{d(n_i a^3)}{dt} = -\langle\sigma v_{\rm M\o l}\rangle \left(n_i n_j - n_i^{\rm eq} n_j^{\rm eq}\right) , \tag{4.12}$$

where σ is the total annihilation cross section summed over final and averaged over initial degrees of freedom, $v_{\rm M\o l}$ is the Møller velocity defined by $v_{\rm M\o l} \equiv \sqrt{|\mathbf{v}_i - \mathbf{v}_j|^2 - |\mathbf{v}_i \times \mathbf{v}_j|^2}$ and $\langle\sigma v_{\rm M\o l}\rangle$ is the thermal average defined as

$$\langle\sigma v_{\rm M\o l}\rangle \equiv \frac{\int d^3p_i d^3p_j \; f_i f_j \; \sigma v_{\rm M\o l}}{\int d^3p_i d^3p_j \; f_i f_j} . \tag{4.13}$$

If the initial particles are identical ($n = n_i = n_j$), the equation becomes

$$\frac{1}{a^3}\frac{d(n a^3)}{dt} = -\langle\sigma v_{\rm M\o l}\rangle \left(n^2 - n_{\rm eq}^2\right) . \tag{4.14}$$

If the particle j is the anti-particle of i, then the total density is $n = 2n_i$ and thus there is an extra factor of $\frac{1}{2}$. We will denote this factor as ς, for Majorana fermions we have $\varsigma = 1$ and for Dirac fermions $\varsigma = \frac{1}{2}$. Thus, we finally have

$$\frac{1}{a^3}\frac{d(n a^3)}{dt} = -\varsigma\langle\sigma v_{\rm M\o l}\rangle \left(n^2 - n_{\rm eq}^2\right) . \tag{4.15}$$

Note that j doesn't have to be identical to or an anti-particle of i. It can also represent a different particle species. Such a scenario is called *co-annihilations* and we would discuss this in the next chapter (section 5.2).

Using entropy conservation, i.e., $\frac{ds}{dt} = -3Hs$, the above equation can be cast

to a more convenient form. Re-defining variables to $Y \equiv n/s_{\rm tot}$ and $x \equiv m/T$,[3] the above equation becomes

$$\frac{dY}{dx} = \frac{\varsigma}{3H}\frac{ds}{dx}\langle\sigma v_{\rm Møl}\rangle(Y^2 - Y_{\rm eq}^2)\,, \tag{4.16}$$

where $Y_{\rm eq} \equiv \dfrac{n_{\rm eq}}{s_{\rm tot}}$.

We are finally at the stage when we can justify the statement that we made earlier, i.e., why the particle species decouple around the time when their interaction rate falls below the Hubble rate. The annihilation rate is defined as $\Gamma_{\rm ann} \equiv n_{\rm eq}\langle\sigma v_{\rm Møl}\rangle$. If in the very early universe we start with the species in equilibrium, i.e. $Y = Y_{\rm eq}$ and $\Gamma_{\rm ann} \gg H$, the solution of Y is forced to follow the equilibrium value. One can also see that for $\Gamma_{\rm ann} \lesssim H$, Y changes very slowly relative to $Y_{\rm eq}$. Thus, when $\Gamma_{\rm ann} \sim H$, the comoving number density of the species becomes roughly constant and this epoch is known as chemical *freeze out* or chemical decoupling.

For a particle with mass m, the energy density today can thus be calculated as

$$\rho_i^0 = m_i n_i^0 = m_i s_0 Y_0\,, \tag{4.17}$$

where we have defined the quantities with subscript or superscript '$_0$' as values today. It is useful to study the relic densities of particles in terms of the density parameter Ω_i (defined in equation 3.10)

$$\Omega_i^0 = \frac{16\pi^3 G}{135 H_0^2} m_i g_{*s}^0 T_0^3 Y_0\,. \tag{4.18}$$

In the next chapter, we will apply the formalism that we have developed, to calculate relic densities of some of the DM freeze out scenarios.

[3] Note that we have used T as the temperature of the thermal bath, i.e., the photon temperature for the standard cosmology.

Chapter 5

Relic density of thermal dark matter

In the previous chapter, we discussed the mathematical framework for calculating relic density of a particle species. In this chapter, we will use equation 4.16 to study how thermal DM freezes out. We will begin by discussing the cases of relativistic and non-relativistic chemical decoupling in section 5.1. In section 5.2, we will discuss *co-annihilations*, a scenario when there are other dark sector particles nearly degenerate with the DM annihilating together to produce the relic abundance.

5.1 Freeze out of thermal dark matter

In this thesis, we only consider *thermally produced* DM through what is known as freeze out mechanism.[1] For such class of DM, one assumes that at very early times, DM was in local thermal equilibrium. DM can be kept in equilibrium with the SM heat bath (or even a relativistic dark species) through the processes shown in Fig. 5.1. The processes $\chi\chi \rightleftarrows$ SM SM ensure that DM remains in chemical equilibrium and χ SM $\rightarrow \chi$ SM keeps DM in kinetic equilibrium with the thermal bath. As the temperature drops, the average energy of particles decreases (see equation 4.4). At some point in time the average energy of the SM particles will become less than m_χ. The process SM SM$\rightarrow \chi\chi$ is now kinematically possible only in the high-energy tail of the distribution, which is heavily suppressed and thus the process becomes inefficient. DM then starts to deplete via $\chi\chi \rightarrow$ SM SM and in order to maintain equilibrium, n_χ starts falling exponentially (equation

[1] An alternative to freeze out scenario is *freeze-in* [95], where DM interacts very feebly with the plasma. A detailed discussion of the mechanism is beyond the scope of this thesis and we refer the interested reader to [95, 96]. For other non-thermal production mechanisms, see for example [97].

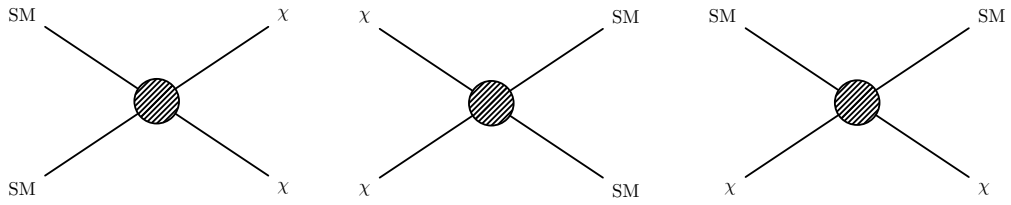

Figure 5.1: Left to right: Feynman diagrams for the processes SM SM$\rightarrow \chi\chi$, $\chi\chi \rightarrow$ SM SM and χ SM $\rightarrow \chi$ SM. The blob in the diagrams indicates sum over all possible processes.

4.3). The number density eventually becomes so small that the annihilation rate of DM falls below the Hubble rate and the process $\chi\chi \rightarrow$ SM SM also becomes inefficient.[2] DM density then freezes out.

First we consider the case where DM (while in equilibrium) has the same temperature as the SM thermal bath through interactions with SM particles and later generalize to include the possibility of DM having a different temperature (via interactions with another dark relativistic species or SM neutrinos).

Thermally produced DM can be classified into three main categories depending on the value of $x_f \equiv m_\chi/T$ at chemical freeze out. If DM was highly relativistic during chemical decoupling, i.e. $x_f \ll 3$, DM is referred to as *Hot Dark Matter* (HDM). One of the most popular HDM candidates are the SM neutrinos. If $x_f \gg 3$, DM is called *Cold Dark Matter* (CDM). The intermediate regime $x_f \sim 3$ is referred to as DM being *Warm Dark Matter* (WDM). The three different types have distinct effects on cosmological structure formation. Observations strongly suggest that most of the DM in the universe should be in the form of CDM [7,8]. We will discuss the three types and the implications on structure formation in more detail in the next chapter.

We first briefly discuss the decoupling of HDM and WDM ($x_f \lesssim 3$). Assuming the number of degrees of freedom to be roughly constant during freeze out, for a relativistic particle in thermal equilibrium with the thermal bath, one can see from equations 4.3 and 4.7 that $Y_{\rm eq}$ is a constant. Thus, when the annihilation rate falls below the Hubble rate and the particle is still relativistic, the value of Y today

[2]The process χ SM $\rightarrow \chi$ SM still keeps DM in kinetic equilibrium. Once this scattering process becomes inefficient, DM completely decouples from the thermal bath and we will consider this epoch in chapter 6.

is just $Y_{\rm eq}$ at freeze out-

$$Y_0 = Y_{\rm eq}(x_f) = \frac{45\zeta(3)}{2\pi^4}\frac{g_\chi^{\rm eff}}{g_{*s}(x_f)}\,, \tag{5.1}$$

where $g_\chi^{\rm eff} = g_\chi$ if DM is a boson and $g_\chi^{\rm eff} = 3g_\chi/4$ if DM is a fermion. The relic density using equation 4.18 is then

$$\Omega_\chi^0 = \frac{8G\zeta(3)}{3\pi H_0^2}\frac{g_{*s}^0}{g_{*s}(x_f)} m_\chi g_\chi^{\rm eff} T_0^3 \;\sim 8\times 10^{-2}\frac{g_\chi^{\rm eff}}{g_{*s}(x_f)}\left(\frac{m_\chi}{1{\rm eV}}\right). \tag{5.2}$$

As the above expression is independent of the annihilation rate, one can put constraints on the masses of HDM. For example, in order to not *overclose* the universe ($\Omega_\chi \leq 1$), the sum of the SM neutrino masses should be $\lesssim 45\,$eV [98].

Unlike the case of HDM and WDM, an exact analytic solution of equation 4.16 doesn't exist for CDM and we have to numerically solve the differential equation. In the non-relativistic limit, the Møller velocity becomes equivalent to the relative velocity $v_{\rm rel}$ and the thermally averaged cross section in this limit is [20, 94]

$$\langle\sigma v_{\rm rel}\rangle_{\rm eq} \simeq \left(\frac{16x^3}{\pi}\right)^{1/2}\int_0^1 dv_\chi\, \sigma v_{\rm rel}\, v_\chi^2 e^{-v_\chi^2 x}\,, \tag{5.3}$$

where v_χ is the velocity of a DM particle in the Center of Mass frame. The above integral can be simplified by expanding $\sigma v_{\rm rel}$ in powers of v_χ.[3] If we assume $\sigma v_{\rm rel} \propto v_\chi^{2n}$ one can solve the above integral analytically to get $\langle\sigma v_{\rm rel}\rangle \propto x^{-n}$ [20]. For $\sigma v_{\rm rel} = a_0 + a_1 v_\chi^2 + ...$ one gets

$$\langle\sigma v_{\rm rel}\rangle \simeq a_0 + \frac{3a_1}{2x} + \dots\,. \tag{5.4}$$

The above terms can be understood to arise from specific angular momentum configurations of the initial state. By expanding the annihilation amplitude (written in spherical basis) in DM velocity v_χ, one can see that the amplitude scales as $\sum_{i,\ell=0}^{\infty} c_{\ell+2i} v_\chi^{\ell+2i}$, with ℓ being the mulitploes and c's being some process dependent coefficients (see for example [99]). Thus the a_0 term comes exclusively from the $s-$wave ($L=0$) state and both $s-$ and $p-$wave ($L=1$) contribute to a_1. If

[3] With the expansion 5.4, one can indeed get an approximate analytic expression for relic density (see for example [65]).

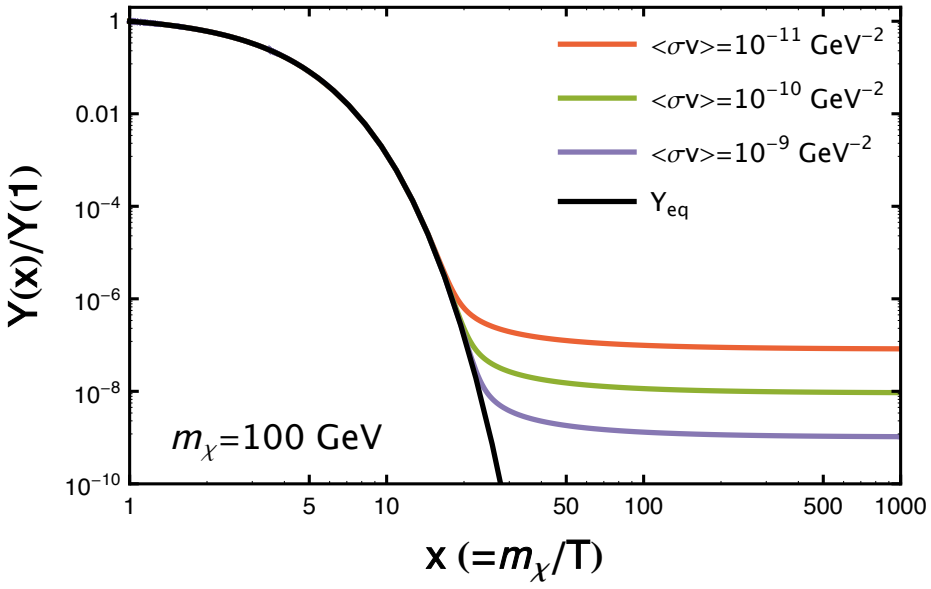

Figure 5.2: **Evolution of $Y(x)$:** Numerical solution of the Boltzmann equation 4.16 for a DM of mass $m_\chi = 100$ GeV. For the plot we have assumed the annihilation process to be purely $s-$wave. The black line represents the equilibrium evolution. After the annihilation rate drops below the Hubble rate, DM freezes out and the number density roughly remains constant. The larger the annihilation rate the longer DM stays in equilibrium and thus has smaller relic abundance.

a_0 dominates, then the process is said to be dominantly $s-$wave annihilation and if a_1 dominates over a_0, we then call it dominantly $p-$wave annihilation and so on.

In Fig. 5.2, we show the numerical solution of $Y(x)$ for a DM particle with mass $m_\chi = 100\,\text{GeV}$ for three different values of $\langle\sigma v_{\text{rel}}\rangle$. We see that at early times (small x) Y tracks the equilibrium solution for all the three cases. We can also see that a larger annihilation rate results in a smaller Y_0. A larger annihilation rate means that DM stays longer in equilibrium and thus depletes more. Using the freeze out condition $\Gamma_{\text{ann}} \sim H$, we can see an approximate dependence

$$Y_0 \sim Y_{\text{eq}}(x_f) \sim \left.\frac{H}{s(x)\langle\sigma v_{\text{rel}}\rangle}\right|_{x=x_f} \propto \left.\frac{x}{m_\chi\langle\sigma v_{\text{rel}}\rangle}\right|_{x=x_f}, \tag{5.5}$$

where the last proportionality holds for the typical case of freeze out taking place in radiation dominated era. Using equation 4.18, we can see that the relic density

of CDM depends mainly on $\langle \sigma v_{\rm rel} \rangle$. With a more careful analysis, the relic density for $m_\chi \gtrsim 10\,\text{GeV}$ to a good approximation is given by [100]

$$\Omega_\chi^0 h^2 \approx \frac{2.1 \cdot 10^{-10}\,\text{GeV}^{-2}}{\langle \sigma v_{\rm rel} \rangle}\,. \tag{5.6}$$

For achieving the cosmologically observed relic density $\Omega_\chi h^2 \sim 0.12$, one needs $\langle \sigma v_{\rm rel} \rangle \sim 1.7 \cdot 10^{-9}\,\text{GeV}^{-2}$. A *Weakly Interacting Massive Particle* (WIMP), i.e. a particle with weak-scale mass and charged under the weak force, will naturally result in an annihilation cross section of the same magnitude-

$$(\sigma v)^{\rm WIMP} \sim \frac{\alpha_W}{64\pi (100\,\text{GeV})^2} \sim 5 \cdot 10^{-10}\,\text{GeV}^{-2}\,. \tag{5.7}$$

This coincidence is often referred to as the *WIMP miracle* in the literature. As shown in Fig. 5.2, WIMPs typically have $x_f \sim 25$. In chapter 7, we will calculate the relic density of a very common DM candidate in Supersymmetry(SUSY), i.e. the neutralino, which is $\mathcal{O}(100\,\text{GeV})$ and is charged under the weak force, thus making it a WIMP.

Until now we considered DM to have the same temperature as the SM thermal bath when in equilibrium. We will now consider the possibility that DM is kept in equilibrium by scattering with a species ($\tilde{\gamma}$) with a different temperature than the SM thermal bath. The different DM temperature can be taken into account by replacing $x \to x/\xi$ in the above equations, where $\xi \equiv T_{\tilde{\gamma}}/T$. For example, equation 5.3 becomes

$$\langle \sigma v_{\rm rel} \rangle_{\rm eq} \simeq \left(\frac{16 x^3}{\pi \xi^3} \right)^{1/2} \int_0^1 dv_\chi\, \sigma v_{\rm rel}\, v_\chi^2 e^{-v_\chi^2 x/\xi}\,. \tag{5.8}$$

In chapter 8, we will work with the case of CDM interacting with a species like $\tilde{\gamma}$. For the case of relativistic decoupling, we refer the reader to [101] for a detailed discussion.

5.2 Co-annihilations

In the previous chapter, we had mentioned that the annihilating particles don't necessarily have to be identical or anti-particle of each other. We can have a scenario when there are many different dark-sector particles in equilibrium annihilating to

standard model particles. Such a scenario is called *co-annihilations* in the literature and was first studied in [102]. The co-annihilation scenario can be realized in particle physics models like SUSY [103].

Consider for example, we have N dark particles in thermal equilibrium with the thermal bath. And out of them the $N-1$ heaviest particles ultimately decay to the lightest dark particle. Assuming that the lightest particle is stable on cosmological time scales, the lightest dark particle can make the DM we are looking for. For covering such a scenario we would have to modify equation 4.12 to evaluate for the total dark sector number density, $n \equiv \sum_{i=1}^{N} n_i$ instead of n_i. Summing the equations for all i, one gets the following differential equation for n [104, 105]

$$\frac{d(na^3)}{dt} = -\langle \sigma_{\text{eff}} v \rangle (n^2 - n_{\text{eq}}^2) \,, \tag{5.9}$$

where $\langle \sigma_{\text{eff}} v \rangle$ is defined as

$$\langle \sigma_{\text{eff}} v \rangle \equiv \sum_{i,j=1}^{N} \langle \sigma_{ij} v_{ij} \rangle \frac{n_i^{\text{eq}}}{n^{\text{eq}}} \frac{n_j^{\text{eq}}}{n^{\text{eq}}} \,, \tag{5.10}$$

here σ_{ij} is the annihilation cross section and v_{ij} is the relative velocity of the species i and j.

For simplicity, consider a dark sector with only two particles denoted by χ and ϕ, with masses, m_χ and $m_\phi \equiv (1+\delta) m_\chi$, with $\delta \geq 0$. In addition to the annihilation diagrams of χ (Fig. 5.1), we have two additional diagrams involving ϕ that we show in Fig. 5.3. The effective cross-section for such a scenario will be

$$\langle \sigma_{\text{eff}} v \rangle = \langle \sigma_{\chi\chi} v_{\chi\chi} \rangle \frac{g_\chi^2 + e^{-\delta x}(1+\delta)^{3/2} g_\chi g_\phi \, r_{\chi\phi} + e^{-2\delta x}(1+\delta)^3 g_\phi^2 \, r_{\phi\phi}}{\left(g_\chi + (1+\delta)^{3/2} e^{-\delta x} g_\phi\right)^2} \,, \tag{5.11}$$

where g_χ and g_ϕ are the internal degrees of freedom of χ and ϕ, respectively, $r_{\chi\phi} \equiv \langle \sigma_{\chi\phi} v_{\chi\phi} \rangle / \langle \sigma_{\chi\chi} v_{\chi\chi} \rangle$, $r_{\phi\phi} \equiv \langle \sigma_{\phi\phi} v_{\phi\phi} \rangle / \langle \sigma_{\chi\chi} v_{\chi\chi} \rangle$ and $x = m_\chi / T$.

The effective cross section for the simple model depends on four independent parameters, δ, $r_{\phi\phi}$, $r_{\chi\phi}$ and g_ϕ. In Fig. 5.4, we show the variation of the relative enhancement $\frac{\langle \sigma_{\text{eff}} v \rangle}{\langle \sigma_{\chi\chi} v_{\chi\chi} \rangle}$ as a function of δ for two different values of $r_{\phi\phi}$. The choice of varying $r_{\phi\phi}$ instead of $r_{\chi\phi}$ is just for illustration purposes, varying $r_{\chi\phi}$ does not change the following discussion qualitatively. We can see that for $\delta \to 0$, co-annihilations can considerably modify the effective annihilation cross section. As

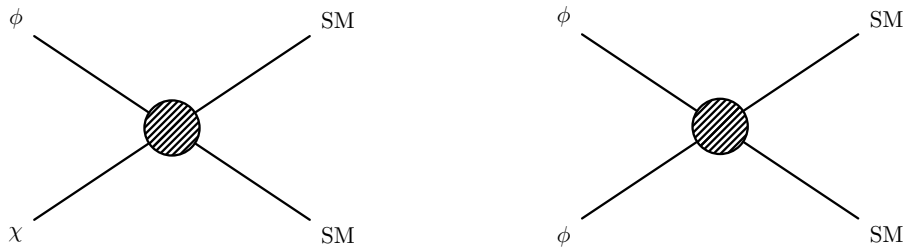

Figure 5.3: Co-annihilation diagrams of two particle species χ and ϕ.

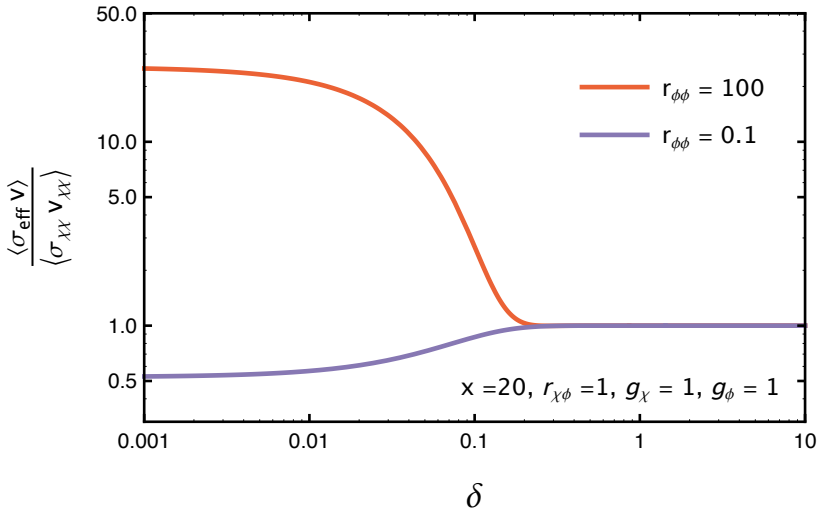

Figure 5.4: $\frac{\langle\sigma_{\rm eff}v\rangle}{\langle\sigma_{\chi\chi}v_{\chi\chi}\rangle}$ vs. δ. For $r_{\chi\phi}, r_{\phi\phi} \gg 1$, the effective cross section increases with decreasing δ until some value of δ and then saturates. If $r_{\chi\phi}, r_{\phi\phi} < 1$, it leads to a suppression due to the *parasitic* degrees of freedom [106].

δ increases, co-annihilation processes become irrelevant due to the exponential suppression factors in equation 5.11 and we get $\langle\sigma_{\rm eff}v\rangle \to \langle\sigma_{\chi\chi}v_{\chi\chi}\rangle$. Thus, co-annihilations are only important if the co-annihilating dark sector particles are nearly degenerate with the lightest particle. In the degenerate limit ($\delta \to 0$), the effective cross-section gets an enhancement or suppression depending on the values of $r_{\phi\phi}$ (or $r_{\chi\phi}$) —

- Enhancement for $r_{\phi\phi} > 1$ (or $r_{\chi\phi} > 1$): The heavier particle (co-)annihilates more efficiently and thus increases the effective annihilation cross section. This scenario is encountered in a lot of SUSY models. For example, co-annihilating sfermions with a Bino, chargino with a Wino or Higgsino and two Higgsinos increases $\langle\sigma_{\rm eff}v\rangle$ [103, 107]. In chapter 7, we will consider

one of these co-annihilation scenarios, squark co-annihilations with a Bino and study its impact on the relic density.

- Suppression for $r_{\phi\phi} < 1$ (or $r_{\chi\phi} < 1$): The suppression is due to g_ϕ present in the denominator of equation 5.11. The particle ϕ remains in equilibrium with the thermal bath but does not (co-)annihilate efficiently, thus decreasing the effective cross section. Such a scenario is referred to as increase in relic density due to *parasitic* degrees of freedom in the literature [106]. This suppression can be observed in sfermion co-annihilation for a Wino or Higgsino DM in SUSY [103, 106]. Note that the suppression will be even more pronounced for larger values of g_ϕ, as is the typical case in SUSY.

Part III

Dynamics II: Full thermal decoupling

Chapter 6

Kinetic decoupling

In this chapter, we will consider kinetic decoupling of DM. In the previous chapter, we discussed that after thermal DM freezes out, it (typically) still remains in equilibrium via scattering with a relativistic partner.[1] This is due to the fact that the scattering rate is proportional to the number density of the scattering partner ($\propto T^3$) as opposed to DM number density ($\propto T^{3/2}e^{-m_\chi T}$) for the case of annihilations. As the universe expands, the number density of the scattering partner also decreases. Eventually, the scattering rate also falls behind the Hubble rate and then DM decouples completely. This epoch is known as kinetic or *thermal* decoupling.

While in equilibrium, DM will have the same temperature as its scattering partner. Thus, the temperature of particles just redshifts, i.e., $T \propto a^{-1}$ before decoupling (see equation 4.5). One can see that this implies $\langle|\mathbf{p}|^2\rangle \propto T \propto a^{-1}$. After decoupling the momentum of a non-relativistic particle redshifts, i.e. $\langle|\mathbf{p}|^2\rangle \propto a^{-2}$. We thus see that $\langle|\mathbf{p}|^2\rangle$ is a good variable to quantify kinetic decoupling. We can define kinetic decoupling as the time when the two asymptotes intersect and the point of intersection to be the kinetic decoupling temperature ($T_{\rm kd}$). An equation for the *temperature* evolution can be obtained by integrating the second moment of the Boltzmann equation [109–111]. In section 6.1, we will develop an equation for the evolution of DM temperature and calculate $T_{\rm kd}$.

[1] There can be scenarios where kinetic equilibrium during freeze out is not a good assumption [20, 108]. In such a scenario, one has to solve a set of coupled differential equations to describe chemical and kinetic decoupling. In this chapter, we will assume DM to be in kinetic equilibrium during chemical decoupling and the comoving number density of DM to be constant during kinetic decoupling.

In equilibrium, DM along with its scattering partner(s) acts like a perfect fluid. Inside the horizon, the pressure of the fluid leads to acoustic oscillations which do not let DM perturbations grow. After decoupling, DM is free to fall in a gravitational well and create DM halos (which serve as seeds for structure formation). The mass inside the horizon at the time of decoupling corresponds to the minimum protohalo mass ($M_{\rm cut}$). Like the observable related to freeze out is the relic density, the observable related to kinetic decoupling is a cut-off in the matter power spectrum. In section 6.2, we will discuss the impact of DM on structure formation. Our discussion will be qualitative in nature and we refer the reader to [109, 112–114] for a mathematical treatment of perturbations to study structure formation.

6.1 Kinetic decoupling temperature

Consider that DM is kept in equilibrium by scattering with a relativistic species ($\tilde{\gamma}$). The scattering partner $\tilde{\gamma}$ might have no interactions with the SM particles and thus also have a different temperature than the SM thermal bath. In this thesis, we will quantify the difference by the parameter $\xi \equiv T_{\tilde{\gamma}}/T$. We now define a *temperature parameter* for DM

$$T_\chi \equiv \frac{g_\chi}{3 m_\chi n_\chi} \int \frac{d^3p}{(2\pi)^3} \mathbf{p}^2 f(\mathbf{p}) \,. \tag{6.1}$$

With the above definition, one recovers $T_\chi = \xi T$ while in equilibrium. We will now develop an equation for T_χ, which we will use to quantify the time of kinetic decoupling.

Like in the case of chemical decoupling, kinetic decoupling of DM can be described by the Boltzmann equation $L[f] = C[f]$ [109–111]. The Liouville operator for DM is the same as in equation 4.10. The collision term for the process $\chi(p)\tilde{\gamma}(k) \to \chi(\tilde{p})\tilde{\gamma}(\tilde{k})$ is given by [110]

$$\begin{aligned} C[f] \;=\; & \frac{1}{2g_\chi} \int \frac{d^3k}{(2\pi)^3 2\omega} \int \frac{d^3\tilde{k}}{(2\pi)^3 2\tilde{\omega}} \int \frac{d^3\tilde{p}}{(2\pi)^3 2\tilde{E}} \\ & \times (2\pi)^4 \delta^{(4)}(\tilde{p} + \tilde{k} - p - k)\, |\mathcal{M}|^2_{\chi\tilde{\gamma}\leftrightarrow\chi\tilde{\gamma}} \\ & \times \left[(1 \pm f_{\mathbf{k}})(1 \pm f_{\mathbf{p}})\, f_{\tilde{\mathbf{k}}} f_{\tilde{\mathbf{p}}} - (1 \pm f_{\tilde{\mathbf{k}}})(1 \pm f_{\tilde{\mathbf{p}}})\, f_{\mathbf{k}} f_{\mathbf{p}} \right] , \end{aligned} \tag{6.2}$$

where ω and $\tilde{\omega}$ denote the energies of the initial and final $\tilde{\gamma}$ particles, respectively

and $\tilde{E}$ denotes the energy of the final state DM particle. The invariant amplitude squared $|\mathcal{M}|^2$ is summed over initial and final degrees of freedom and also considers both particle and anti-particle scattering processes. Assuming DM to be highly non-relativistic and the momentum transfer between χ and $\tilde{\gamma}$ to be small during kinetic decoupling, one can calculate the evolution of T_χ by integrating the second moment of the Boltzmann equation to get (see paper II [22])

$$\frac{d\log y}{d\log x} = \left(1 - \frac{1}{3}\frac{d\log g_{*s}}{d\log x}\right)\frac{\gamma(T_{\tilde{\gamma}})}{H(T)}\left(\frac{y_{\rm eq}}{y} - 1\right), \tag{6.3}$$

where we have introduced the dimensionless parameter $y \equiv m_\chi T_\chi s_{\rm tot}^{-2/3}$ and the momentum transfer rate $\gamma(T_{\tilde{\gamma}})$. The latter is given by

$$\gamma(T_{\tilde{\gamma}}) = \frac{1}{48\pi^3 g_\chi T_{\tilde{\gamma}} m_\chi^3}\int d\omega\, k^4 f_{\mathbf{k}}(1 \pm f_{\mathbf{k}})\,\langle|\mathcal{M}|^2\rangle_t\,, \tag{6.4}$$

where we have defined $k \equiv |\mathbf{k}|$ and $\langle|\mathcal{M}|^2\rangle_t \equiv \frac{1}{8k^4}\int_{-4k^2}^{0} dt\,(-t)\,|\mathcal{M}|^2$, where t is the Mandelstam variable. Assuming constant relativistic degrees of freedom during kinetic decoupling, we can simplify equation 6.3 to

$$\frac{dT_\chi}{dT} - 2\frac{T_\chi}{T} = \frac{\gamma(T_{\tilde{\gamma}})}{H(T)}\left(\frac{T_\chi}{T} - \xi(T)\right). \tag{6.5}$$

We can see from the above equation that T_χ is forced to be equal to ξT for $\gamma \gg H$ and for $\gamma \ll H$, $T_\chi \propto T^2 \propto a^{-2}$, which is what we expected.

Like in the case of chemical decoupling, one should solve equation 6.5 numerically to find the evolution of T_χ. In the top panel of Fig. 6.1, we show the numerical solution of equation 6.5 for a very simple model— two scalars χ and $\tilde{\gamma}$ scattering via a dimensionless quartic coupling λ, i.e. $\Delta\mathcal{L} = \frac{\lambda}{4}\phi_\chi^2\phi_{\tilde{\gamma}}^2$. For illustration, we show the cases $\xi = 0.5\,, 1$ for two values of λ and fix $m_\chi = 100\,\text{GeV}$.[2] In the bottom panel of the figure, we show the ratio $\gamma(T_{\tilde{\gamma}})/H(T)$.

For $\gamma \gg H$, DM is kept in equilibrium and $T_\chi = \xi T$. Around $\gamma \sim H$, T_χ starts to deviate from ξT and DM decouples. We see that DM decouples later for

[2] In this thesis, we will assume ξ to be a constant. In principle, the parameter ξ can be a function of time (for a comprehensive discussion on the time dependence see [101]). For the figure, we have also fixed $m_{\tilde{\gamma}} = 100\,\text{keV}$, but for the relevant range of temperatures shown in the figure, the mass is not important and the results hold for any relativistic $\tilde{\gamma}$.

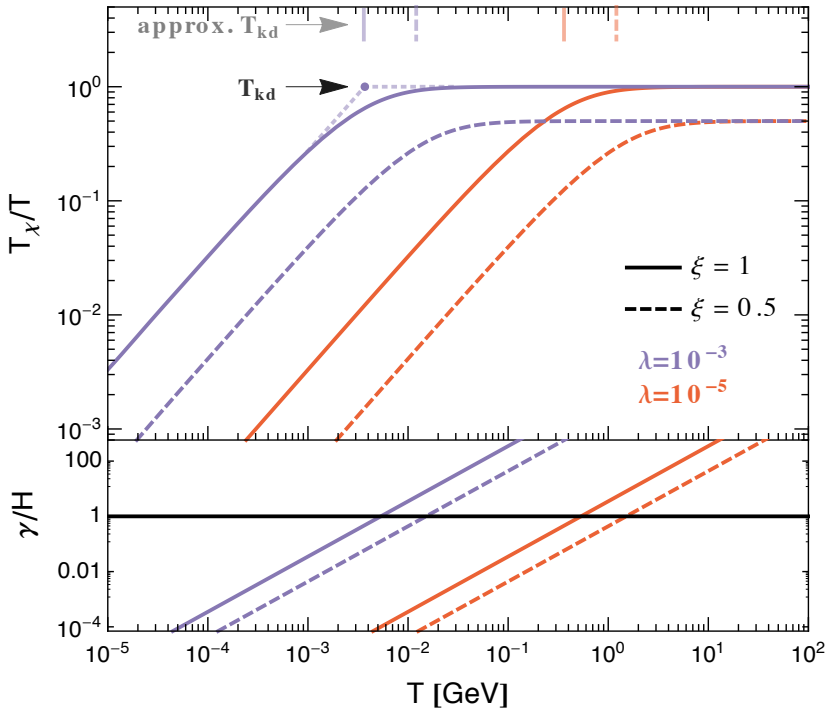

Figure 6.1: **TOP:** Evolution of T_χ for a scalar DM scattering with a scalar relativistic species via a quartic coupling λ. We have shown two combinations of the coupling λ and temperature parameter ξ. **BOTTOM:** The ratio of $\gamma(T_{\tilde{\gamma}})$ and the Hubble rate. For $\gamma \gg H$, DM remains in equilibrium and T_χ follows the equilibrium temperature. DM decouples from the scattering partner when $\gamma \sim H$ and after that $T_\chi \propto a^{-2}$. The decoupling temperature $T_{\rm kd}$ is defined as the intersection of these two asymptotes (which we explicitly show for the $\lambda = 10^{-3}$ & $\xi = 1$ case). For comparison, we also show the analytic solution $T_{\rm kd}$ obtained from expression 6.7 as vertical lines in the top panel.

a larger scattering rate. After this time, T_χ decreases more rapidly, $T_\chi \propto a^{-2}$. We can now define the decoupling temperature $T_{\rm kd}$ as the intersection of the two asymptotes (which we have shown for the solid blue line).

One can also find an approximate solution for $T_{\rm kd}$ by expanding $\langle|\mathcal{M}|^2\rangle_t$ in powers of small energies ($\omega \ll m_\chi$)

$$\frac{1}{g_\chi}\left\langle|\mathcal{M}|^2\right\rangle_t \equiv c_n \frac{\omega^n}{m_\chi^n} + \mathcal{O}\left(\frac{\omega^{n+1}}{m_\chi^{n+1}}\right), \tag{6.6}$$

to get (see paper II [22])

$$\frac{T_{\rm kd}}{m_\chi} = \left[\left(\frac{b}{n+2}\right)^{1/(n+2)} \Gamma\left(\frac{n+1}{n+2}\right)\right]^{-1}, \tag{6.7}$$

where

$$b = \sqrt{\frac{5}{2(2\pi)^9 g_{\rm eff}}(n+4)!\,\zeta(n+4)\,\xi^{n+4} c_n \gamma_n \frac{M_{\rm Pl}}{m_\chi}}\,, \tag{6.8}$$

where $g_{\rm eff}$ is the effective relativistic energy degrees of freedom and $\gamma_n = 1$ for bosonic $\tilde{\gamma}$ and $\gamma_n = 1 - 2^{-(n+3)}$ for a fermionic $\tilde{\gamma}$. The above solution holds for $n > -1$ (even for non-integer values). For the simple model we considered above, we have $\langle|\mathcal{M}|^2\rangle_t = \lambda^2$ and thus $n = 0$. In Fig. 6.1, we have also shown this approximate solution for this model as vertical lines in the top panel. We can see that the above approximation provides a very good estimate for $T_{\rm kd}$.

6.2 Kinetic decoupling and structure formation

Before kinetic decoupling, the tight coupling between DM and the scattering partner generates a pressure which does not let the perturbation δ_χ grow. After kinetic decoupling, DM perturbations grow and structure formation takes place. There are two main effects of the epoch of kinetic decoupling on the halo formation [112–115]—

- The pressure in the DM-$\tilde{\gamma}$ fluid results in oscillating DM density perturbations. Analogous to the BAOs, we call the oscillatory behavior in the dark sector as Dark Acoustic Oscillations (DAO). All the perturbation modes inside the horizon at the time of kinetic decoupling are thus suppressed.

- After the last scattering $T < T_{\rm kd}$, the viscosity coefficients vanish and DM free streams. If the distance traveled by the DM particles in time t is larger than the wavelength of a perturbation mode at t, that mode gets damped. DM can move from overdense regions to underdense regions, thus wiping out all the structure less than this scale of free streaming. This is referred to as *free streaming* or *collision-less* damping [112–114].

The length scales over which the two effects suppress the structure will depend on the time of decoupling (or $T_{\rm kd}$) [109, 113]. As all the perturbations are erased below these scales, the relevant scale ($l_{\rm cut}$) for a DM model is the larger of the two.

This damping scale can be seen as a sharp cutoff in the matter power spectrum (see for example [116]). The mass contained in a sphere of radius $l_{\rm cut}$ then corresponds to the minimum halo mass and is called the *cutoff mass* ($M_{\rm cut}$).

For HDM the dominant effect is free streaming and$M_{\rm cut}$ will be of the order of the size of typical galaxy clusters $\sim 10^{14} M_\odot$ [117]. Thus, in a universe consisting of mainly HDM, the large structures will have to break down to form the structure we see today. Observations strongly suggest that this is not the case with our universe and most of the DM has to be non-relativistic [7, 8]. For non-relativistic DM, the dominant suppression effect depends on the values of $T_{\rm kd}$ and m_χ [115]. For standard WIMPs, $M_{\rm cut}$ is typically very small due to the large $T_{\rm kd}$ and small free streaming lengths [109, 115]. Thus for CDM, small structures form first and then they cluster together to form the large scale structures. This is referred to as the *hierarchical* structure formation in the literature.

Using N-body simulations and including non-linear perturbations, Vogelsberger et al. [116] found the following relation to be a good fit for $M_{\rm cut}$ when DAO is the dominant suppression mechanism

$$M_{\rm cut} = 5 \times 10^{10} \left(\frac{T_{\rm kd}}{100\,{\rm eV}} \right)^{-3} h^{-1} M_\odot \,, \tag{6.9}$$

and for the case of WDM when free-streaming effects are the dominant mechanism it is [116]

$$M_{\rm cut}^{\rm WDM} = 10^{11} \left(\frac{m_{\rm WDM}}{\rm keV} \right)^{-4} h^{-1} M_\odot \,. \tag{6.10}$$

Part IV

Discussion of results

Chapter 7

Efficient treatment of QCD corrections for Majorana dark matter

7.1 Outline

In chapter 5, we calculated the effective annihilation cross section $\langle \sigma_{\rm eff} v \rangle$ for the various chemical freeze out scenarios. Theoretically, processes up to all orders in perturbation theory should be considered when computing $\langle \sigma_{\rm eff} v \rangle$. The present CMB experiments [4] predict the relic density of CDM to a percent level accuracy. Thus, the theoretical prediction of relic density for a particle physics model should match the accurate measurement. Due to a large strong coupling constant α_s, Quantum Chromodynamics (QCD) corrections can be very important for an accurate relic density prediction [11, 118–126].

In this chapter, we will discuss an efficient way to estimate the dominant QCD corrections in $\langle \sigma_{\rm eff} v \rangle$ for Majorana DM. A Majorana type DM particle can be realized in many particle physics scenarios [47, 127–129]. Most commonly considered realization is the neutralino in Supersymmetry (SUSY) [130, 131]. In this chapter, we will work in SUSY framework but our results can be generalized to any Majorana type DM (see [132] for an application of this work).

A SUSY transformation transforms fermions into bosons and vice-versa. In this thesis, we will only consider the Minimal Supersymmetric Standard Model (MSSM), which is constructed by introducing the minimal required number of

additional fields to the SM [133–136]. In the MSSM, there is an additional new bosonic (fermionic) degree of freedom for every SM fermionic (bosonic) degree of freedom and the new particles are collectively called *sparticles*.

The basic building blocks in a SUSY model are *chiral* and *gauge* supermultiplets. A chiral supermultiplet consists of a Weyl fermion and a complex scalar. The left and right handed chirality states of standard model fermions being Weyl spinors make up the fermionic part in the chiral supermultiplet. And there are two supersymmetric scalar particles each for a left or right handed Standard model fermion. Thus, in total we have four new scalar particles (or two new scalar particle-antiparticle pairs). The new scalar particles are named by adding prefix $s-$ to the fermion name, for example, *squarks* ($\tilde{q}$) and *stops* ($\tilde{t}_{1,2}$). A gauge supermultiplet consists of a gauge boson and a supersymmetric fermionic partner called gaugino. The name of a gaugino is constructed by appending *-ino* to the boson's name, for example, *Bino* ($\widetilde{B}$), *Wino*s ($\widetilde{W}^0, \widetilde{W}^{\pm}$) and *Gluino*s ($\tilde{g}$). Since a massless vector boson has only two degrees of freedom, a gaugino is a Majorana fermion.

Higgs being spin-0 are put in the chiral supermultiplets. The superpartners of the Higgs are Majorana fermions called *Higgsinos*. Unlike in the standard model, we require two complex Higgs doublets instead of one. The extra doublet is necessary for the cancellation of anomalies which are introduced by Higgsinos, and give masses to both up and down quarks [137–139]. Three out of eight degrees of freedom are used as usual to make the standard model gauge bosons massive and we are left with five physical Higgs, two of them are CP-even (h^0, H^0 with $m_h < m_H$), one is CP-odd (A^0) and two are electrically charged ($H^{\pm}$). The discovered Higgs [140, 141] is believed to be the lighter CP-even supersymmetric Higgs (h), satisfying all the properties of the standard model Higgs.[1] As the neutral Higgsinos ($\widetilde{H}_1^0$ and $\widetilde{H}_2^0$) and the neutral gauginos ($\widetilde{B}$ and $\widetilde{W}^0$) have the same quantum numbers, they mix to form four mass eigenstates known as *neutralinos* (denoted by $\tilde{\chi}_i$).

Unlike in SM, baryon and lepton violating terms arise inevitably in the SUSY Lagrangian. For getting rid of such terms, a new multiplicative discrete symmetry known as $R-$parity is introduced.[2] All SM particles have even $R-$parity and all

[1] Note that the heavier state H being of mass 125 GeV is not yet dismissed [142, 143].

[2] Note that there exist models with $R-$parity volation that are not in conflict with the experimental data (for a review see [144]).

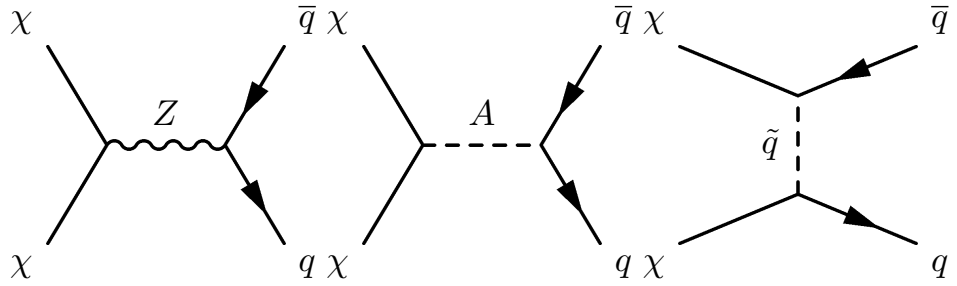

Figure 7.1: s-wave diagrams for Tree level Neutralino annihilation into quark pair through Z boson, pseudo-scalar Higgs A and squark $\tilde{q}$ exchange. Figure taken from paper I [21].

sparticles are odd under $R-$parity. Consequently, in any interaction, sparticles can occur only in pairs. Thus in $R-$parity conserving SUSY models, the Lightest Supersymmetric Particle (LSP) is stable and if neutral a viable DM candidate [47, 145, 146]. In this thesis, we assume the lightest neutralino to be the LSP and thus the DM candidate and we will refer to the lightest neutralino as simply the neutralino, and denote it by χ.

As the annihilating neutralinos are Majorana fermions, fermion pair production is helicity suppressed (see for example [47, 147]). In section 7.2, we will motivate a way to lift this suppression by considering higher order corrections. Specifically, it is the emission of an extra boson along with the final state fermions that can lift the suppression. Including the higher order diagrams increases the number of diagrams exponentially, therefore it is a big obstacle for performing global scans over a SUSY model's parameter space [148–151]. In section 7.3, we will motivate an efficient way to calculate higher order corrections. We will finally conclude the chapter by discussing the impact of QCD corrections on relic density of neutralino in section 7.4.

7.2 Lifting of helicity suppression

Neutralinos can (co-)annihilate into various SM final states. As was mentioned above, for this thesis we are primarily interested in quark pair production. In the non-relativistic limit, neutralinos can annihilate to a quark pair via Z, A and squark exchange. We show the three Feynman diagrams in Fig. 7.1. In this limit, the cross-section for the process $\chi\chi \to q\bar{q}$ scales as $\sigma v \propto m_f^2/m_\chi^2$ [47, 152]. Thus

the process is heavily suppressed, as we typically have $m_q \ll m_\chi$. This suppression is known as *helicity* suppression in the literature. The dominant contribution to $\langle \sigma_{\rm eff} v \rangle$ comes from the $p-$wave part, which is also suppressed by a factor of v^2 but is typically much larger than $s-$wave due to the m_q^2/m_χ^2 suppression.

We will now discuss the origin of this suppression and motivate how the suppression can be lifted. Majorana fermions are their own anti-particles, therefore an initial state comprising two Majorana fermions should be invariant under the charge conjugation transformation. The general rule for charge conjugation is $C = (-)^{L+S}$, where L refers to the total orbital angular momentum and S refers to the spin of the system. This implies that both L and S need to be either even or odd for having $C = +1$. Thus for the case of s-wave ($L = 0$), the only possibility for the two-Majorana initial state is $S = 0$. This, in turn, implies that the s-wave two-Majorana initial state is odd under the combined charge conjugation and parity symmetry $CP = -1$, because the parity transformation is $P = (-1)^{L+1}$. Note that the two-Majorana $L = 0$ state behaves like a pseudoscalar particle ($S = 0$ and $P = -1$) and we will make use of this property later in section 7.3 to simplify neutralino annihilation calculations. For the $p-$wave annihilation ($L = 1$) we will similarly have $S = +1$ and $CP = +1$.

Let us assume CP to be conserved in the process $\chi\chi \to f\bar{f}$. For the $L = 0$ case, the spins of the two fermion final state have to be aligned in the opposite direction for getting $S = 0$. In the center of mass frame, the final state fermions would be emitted back to back because of momentum conservation. For having $S = 0$, we will therefore need the final state particles to have the same helicity. If the process $\chi\chi \to f\bar{f}$ conserves chirality, the final state fermions would necessarily have the opposite chirality, i.e., $\chi\chi \to f_L \bar{f}_R$. We also know that in the ultra-relativistic limit, helicity and chirality are the same. We can now see the problem, because of chirality conservation, the relativistic final state fermions would have opposite helicity and hence $S = +1$. Hence for exactly massless fermions, the annihilation cross section will be zero. The final state fermions are not exactly massless, for example, for relativistic Dirac fermions the right handed helicity state $u_\uparrow$, is related to chiral states $u_{R,L}$ as

$$u_\uparrow \simeq \left(1 - \frac{m_f}{2m_\chi}\right) u_R + \frac{m_f}{2m_\chi} u_L \,. \tag{7.1}$$

Thus by having opposite chiralities but the same helicity of final state fermions suppresses the cross section by a factor of m_f^2/m_χ^2. For the p-wave annihilation,

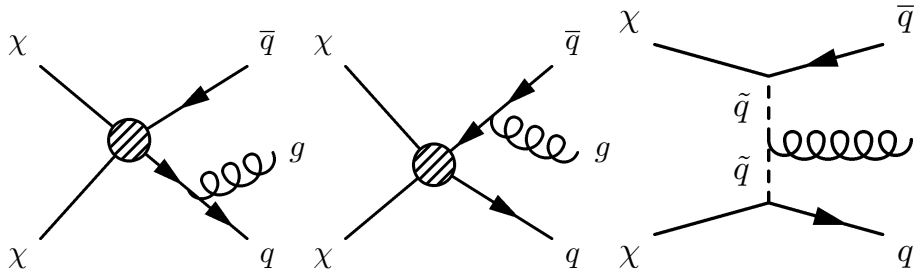

Figure 7.2: Gluon bremstrahlung diagrams. The left and the middle diagram correspond to FSR off q and $\bar{q}$ respectively and the diagram on the right corresponds to gluon VIB. Figure taken from paper I [21].

we do not have this suppression because we need $S = 1$ for the final state. It is worth noting that the same suppression is also seen in the well-known case of pion decay because of the same reason.

The $\tilde{f}$ and Z exchange neutralino annihilation processes (Fig. 7.1) preserve chirality and thus suffer from helicity suppression. On the other hand, A^0 exchange does not conserve chirality but because of Yukawa couplings contributes a factor of m_f^2/m_χ^2 in the cross section anyway. Thus, the $s-$wave neutralino annihilation into quarks is suppressed by m_q^2/m_χ^2.

As was first noted in [153, 154], helicity suppression can be lifted by emitting a boson along with the final state fermions. The emitted boson can help keep the momentum and the total spin of the final system to zero. For example, if the fermions are emitted in the same direction and a vector boson is emitted in the opposite direction, we will have $S = 0$ for the final system and also have final fermions with opposite chiralities. Thus, helicity suppression can be lifted with the help of unavoidable higher order corrections.

In this thesis, we would only focus on gluon emission, for a recent extensive discussion for other bosons, see [147]. For neutralino annihilation to quarks, we can have two different types of gluon emission. Firstly, we can radiate a gluon from one of the legs of the final state quarks, which is known as *Final state radiation* (FSR) emission. Secondly, a gluon can be emitted from the virtual squark mediating in the t-channel process, this is referred to as *Virtual Internal Bremsstrahlung* (VIB) emission. We show the two types in Fig. 7.2.

The amplitude of the FSR diagram is dominated by infrared and collinear

singularities [155]. Thus the final state fermions, one of which is on-shell and the other which emits gluon is almost on-shell, would be emitted almost back to back. Hence FSR cannot lift helicity suppression (for a detailed discussion see [156]). Therefore it is only gluon VIB that can help in lifting the suppression.[3]

In the $v \to 0$ limit, the differential cross section for photon VIB has been calculated in full generality [155]. The gluon VIB cross-section can be obtained from the photon VIB cross section with the simple replacement $\alpha_{\rm em} Q^2 \to \frac{4}{3}\alpha_s$, where Q is the electric charge of the quark. In the limit $m_q \ll m_\chi$,[4] the gluon VIB cross section $\left(\sigma^{\rm VIB}_{\chi\chi\to q\bar{q}g}\right)$ is [157, 158]

$$\begin{aligned}\left(v\sigma^{\rm VIB}_{\chi\chi\to q\bar{q}g}\right)_{v\to 0} \simeq & \frac{\alpha_s|\tilde{g}_R|^4}{48\pi^2 m_\chi^2}(\mu_R+1)\left[\frac{\pi^2}{6} - \ln^2\left(\frac{\mu_R+1}{2\mu_R}\right) - 2{\rm Li}_2\left(\frac{\mu_R+1}{2\mu_R}\right)\right. \\ & \left. + \frac{4\mu_R+3}{(\mu_R+1)^2} + \frac{4\mu_R^2-3\mu_R-1}{2\mu_R(\mu_R+1)}\ln\left(\frac{\mu_R-1}{\mu_R+1}\right)\right] \\ & + (R\leftrightarrow L) \\ \equiv & \frac{\alpha_s|\tilde{g}_R|^4}{48\pi^2 m_\chi^2}\Upsilon(\mu_R) + (R\leftrightarrow L)\,, \end{aligned} \tag{7.2}$$

where the subscripts R and L denote the right handed and left handed squarks, respectively, $\mu_{R(L)} \equiv (m_{\tilde{q}_{R(L)}}/m_\chi)^2$, $\tilde{g}_R P_L (\tilde{g}_L P_R)$ is the coupling of right handed (left handed) squark, neutralino and the quark and lastly we have defined a function Υ that captures the dependence on the mass difference parameter μ.

One can see from the above expression that $\sigma^{\rm VIB}_{\chi\chi\to q\bar{q}g}$ depends very strongly on the mass difference of the mediating squark and neutralino. In Fig. 7.3, we plot Υ as a function of μ. We can see that it is maximal for $\mu_{R,L} = 1$ and away from the degenerate limit, $\sigma^{\rm VIB}_{\chi\chi\to q\bar{q}g}$ decreases very quickly with increasing μ. For a reference, for $\mu = 4$ it will be suppressed by a factor of ~ 0.004 relative to the degenerate limit. Thus, we can see that VIB is only important when squark masses are very close to the neutralino mass. In the limit $m_{\tilde{q}} \sim m_\chi$, the cross section scales as $\sigma^{\rm VIB}_{\chi\chi\to q\bar{q}g}/\sigma^{s-{\rm wave}}_{\chi\chi\to q\bar{q}} \sim (\alpha_s/\pi)\, m_\chi^2/m_q^2$. We can thus see that though $\sigma^{\rm VIB}_{\chi\chi\to q\bar{q}g}$ is suppressed by the coupling constant, for quarks much lighter than the

[3] If the neutralino is not a pure Bino, we can also emit $W^\pm$ and Z from one of the initial neutralinos legs. This is known as *Initial state radiation* (ISR). ISR can also lift the helicity suppression.

[4] For the full general expressions for VIB, see the DarkSUSY 6.0.0 code (src_models/mssm/an_ib3/)

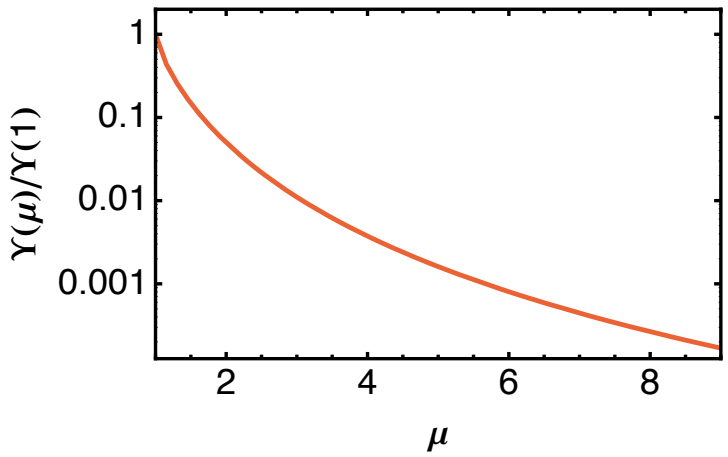

Figure 7.3: Relative enhancement of VIB $\Upsilon(\mu)/\Upsilon(1)$ (equation 7.2) as a function of squared mass ratio $\mu = (m_{\tilde{q}}/m_{\chi})^2$. The VIB enhancement decreases very rapidly with increasing μ.

neutralino $\sigma^{\rm VIB}_{\chi\chi\to q\bar{q}g}$ can be much larger than the s-wave tree-level cross-section and thus be the dominant contribution to the total cross section.

7.3 Efficient treatment of QCD radiative corrections- the pseudoscalar approximation

We had mentioned earlier that inclusion of higher order corrections increases the computation time. This poses a great challenge when performing global scans over a large parameter space, which is the case in SUSY [148–151]. We will now discuss a very efficient way of including QCD corrections in computations by making a very well motivated approximation which captures all the leading effects.

In section 7.2, we discussed that the two non-relativistic Majorana fermion state transforms as a pseudoscalar under Lorentz transformations. This implies that the non-relativistic neutralino annihilation can be effectively treated as a pseudoscalar particle ϕ with mass $M = 2m_{\chi}$ decaying at rest [159,160]. We show the contributing NLO diagrams[5] for such a decay in Fig. 7.4. In this chapter, we will

[5] Note that the approximation works only for QCD or QED corrections, as neutralinos are singlets under $SU(3)_c$ and $U(1)_{\rm em}$. The initial state neutralinos can emit virtual or on-shell electroweak bosons and thus the initial state can no longer be approximated as a neutral pseudoscalar.

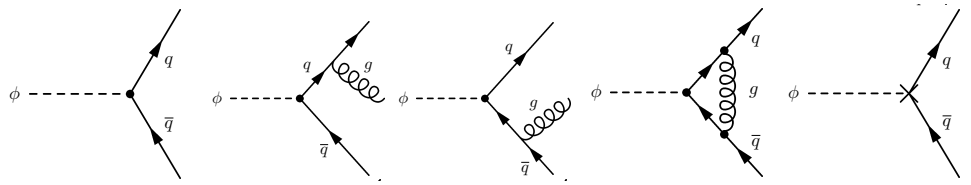

Figure 7.4: Diagrams for a pseudoscalar(ϕ) decay up to $\mathcal{O}(\alpha_s)$. The diagrams from left to right correspond to tree-level decay, FSR off q, FSR off $\bar{q}$, vertex correction and counterterm respectively.

use the (sub)superscripts $^{\text{simp}}$ and $^{\text{full}}$ to denote the calculations in the simplified pseudoscalar approximation and the full neutralino annihilation, respectively. The total one-loop decay rate ($\Gamma^{\text{simp}}_{\text{tot}}$) for the diagrams shown in Figure 7.4 is related to the tree-level decay rate (Γ^{simp}_{0}) as [21, 161, 162]

$$\frac{\Gamma^{\text{simp}}_{\text{tot}}}{\Gamma^{\text{simp}}_{0}} = 1 + \frac{4\alpha_s}{3\pi}\left[\frac{1+\beta_0^2}{\beta_0}\left\{4\text{Li}_2\left(\frac{1-\beta_0}{1+\beta_0}\right) + 2\text{Li}_2\left(-\frac{1-\beta_0}{1+\beta_0}\right) - \log\frac{8\beta_0^2}{(1+\beta_0)^3}\log\frac{1+\beta_0}{1-\beta_0}\right\}\right.$$
$$\left. - \log\frac{64\beta_0^4}{(1-\beta_0^2)^3} + \frac{3}{8}(7-\beta_0^2) + \frac{19+2\beta_0^2+3\beta_0^4}{16\beta_0}\log\frac{1+\beta_0}{1-\beta_0}\right], \quad (7.3)$$

where we have defined $\beta_0 \equiv \sqrt{1-\dfrac{4m_q^2}{M^2}}$.

At tree-level, one can see that the decay rate and the cross section for neutralino annihilation are the same up to a constant of proportionality, i.e. $\Gamma^{\text{simp}}_0 \propto m_\chi \sigma^{\text{full}}_0 v$. For relating Γ^{simp} and σ^{full}, we define a quantity analogous to the annihilation cross section as

$$\sigma^{\text{simp}}_0 v \equiv \frac{\Gamma^{\text{simp}}_0}{A^2 m_\chi} \quad \& \quad \sigma^{\text{simp}}_{\text{tot}} v \equiv \frac{\Gamma^{\text{simp}}_{\text{tot}}}{A^2 m_\chi}, \quad (7.4)$$

with A being a proportionality constant defined by $\sigma^{\text{simp}}_0 v \equiv \sigma^{\text{full}}_0 v$. In the limit $m_q \ll m_\chi$, the result 7.3 simplifies to

$$\sigma^{\text{simp}}_{\text{tot}} \simeq \sigma^{\text{simp}}_0 \left[1 + \frac{\alpha_s}{\pi}\left(3 + 4\log\frac{m_q}{4m_\chi}\right)\right]. \quad (7.5)$$

From the above expression, one can see that $\sigma^{\text{simp}}_{\text{tot}}$ becomes negative for $m_q/m_\chi \to 0$. This indicates that our $\mathcal{O}(\alpha_s)$ calculation breaks down for $m_\chi \gg m_q$ and higher

order corrections are important. We can calculate the higher orders by re-summing the leading logarithms to all orders in α_s. The above result after re-summation becomes (see [161, 162] for details)

$$\sigma_{\rm tot}^{\rm simp} \simeq \frac{\overline{m}^2(\sqrt{s})}{\overline{m}^2(2m_q)}\sigma_0^{\rm simp}\left[1+\frac{3\alpha_s}{\pi}\right], \tag{7.6}$$

where $\overline{m}$ is the running quark masses defined in MS renormalization scheme. Now the result is well behaved in the limit $m_\chi \gg m_q$ and we show the ratio $\sigma_{\rm tot}^{\rm simp}/\sigma_0^{\rm simp}$ (eq. 7.6) for charm, bottom and top quark final states in Fig. 7.5. For comparison, we also show the $\mathcal{O}(\alpha_s)$ result (eq. 7.3) for top quark. As can be seen from the figure, QCD corrections suppress the total cross-section over the tree level result (except when $m_\chi \gtrsim m_q$). Note that the resummed result is valid only for $m_q \ll m_\chi$ and the NLO result breaks down for $m_q \ll m_\chi$. The two lines cross at $m_\chi \sim 1.85\, m_q$, for paper I [21] we used the NLO result for $m_\chi < 1.85\, m_q$ and the resummed result for $m_\chi > 1.85\, m_q$.

For relating to $\sigma_{\rm tot}^{\rm full}$, i.e. the full neutralino annihilation to quarks cross-section, by the above approximation we are ignoring the contribution of the diagrams with gluino loops, squark self energy diagrams, supersymmetric corrections to the quark self energy and VIB diagrams. Note that except VIB, the ignored processes do not help in lifting the helicity suppression. As we saw earlier, VIB can be very important in a scenario with squark close in mass to the annihilating neutralino. Thus, in our computation, we add the full VIB cross-section ($\sigma_{\chi\chi\to q\bar{q}g}^{\rm VIB}$) to $\sigma_{\rm tot}^{\rm simp}$ and consider the sum to be the total cross-section.

In paper I [21], we compared our simplified approach to the full NLO calculation done by Herrmann et al. [11]. In Ref. [11], the prime focus was on models with relatively light neutralino masses ($m_\chi \gtrsim 200\,$GeV), which could produce cosmologically interesting relic densities owing to unsuppressed top quark production. It is worth noting that for the mass range considered, the VIB process ($t\bar{t}g$) is sub-dominant as compared to $t\bar{t}$ production. We thus expect our simplified approach to be in worst agreement with the full NLO calculation for these models. We saw that for models with neutralino annihilation dominated by A or $\tilde{q}$ exchange we get an error of $\leq 1\%$. But for models with Z exchange, we saw the errors to be larger ($\sim 15\%$). We thus see that our simplified approach gives a very good agreement with the full NLO calculation even for the most pessimistic scenario. We also saw for $m_\chi \gg m_q$, the NLO calculation fails and we need to

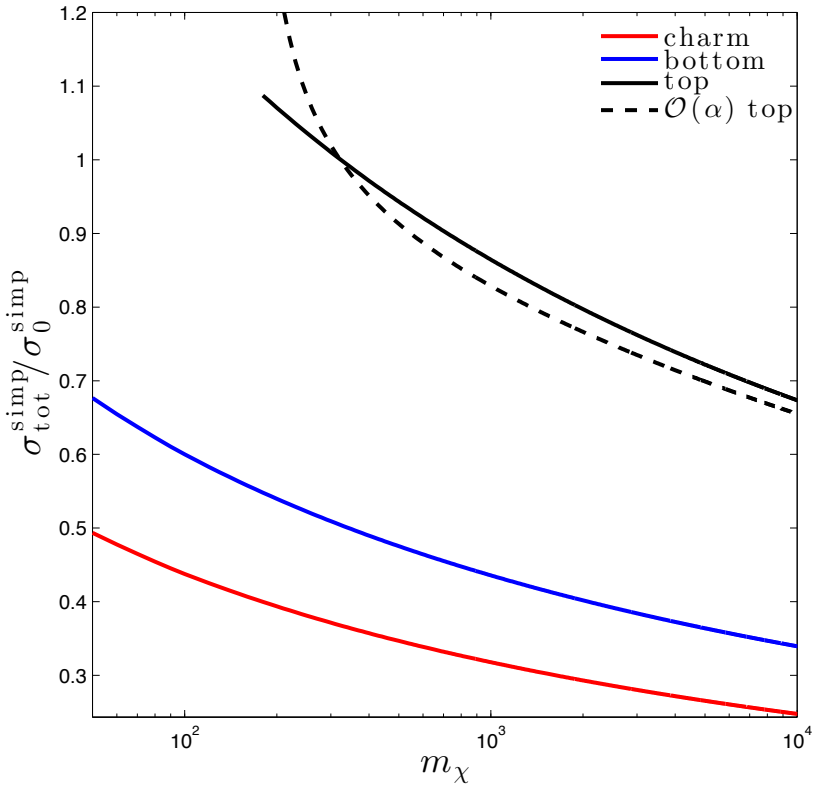

Figure 7.5: Ratio of resummed cross section $\sigma_{\rm tot}^{\rm simp}$ and the tree level cross section σ_0 for charm (red), bottom (blue) and top (black) final states. For top final states we also show the NLO result in the simplified model. Figure taken from paper I [21].

consider higher orders in α_s. We thus expect our simple result (eq. 7.6) to provide a more accurate estimate than the NLO result in the limit $m_\chi \gg m_q$.

7.4 Impact of QCD corrections on relic density

The impact of QCD corrections to neutralino annihilation on the relic density has been previously studied by various authors [11, 118–126]. We now consider the effect of QCD corrections on the relic density of neutralinos using our simplified approach. As discussed in Chapters 4 and 5, for calculating the relic density one needs to compute the thermally averaged cross section $\langle \sigma_{\rm eff} v \rangle$. For including QCD corrections, we include the sum of $\sigma_{\rm tot}^{\rm simp} v$ and $\sigma_{\chi\chi\to q\bar{q}g}^{\rm VIB} v$ to $\langle \sigma_{\rm eff} v \rangle$ at zero velocity

to the relic density routines of DarkSUSY [163].[6]

Fermionic final states are the main annihilation channels for a Bino like neutralino and are thus very important for the relic density computation [138]. Whereas for a Wino or Higgsino like neutralino, the total annihilation rate is dominated by chargino-neutralino co-annihilation [107] and fermionic final states are not important. Also, the impact of QCD corrections for quark final states is maximal for a scenario when the total annihilation rate is dominated by $\sigma^{\rm VIB}_{\chi\chi\to q\bar{q}g}v$. For showing the impact, we thus consider a scenario when the neutralino is a pure Bino and all the sparticles except squarks are much heavier than the neutralino. The two requirements ensure that the t-channel squark exchange dominates the total annihilation rate. In Fig. 7.6, we show the relic density $\Omega_\chi h^2$ as a function of the neutralino mass. For the plot, we have fixed the squark masses to be $m_{\tilde{q}} = 1.2 m_\chi$, so that we get a sizable VIB contribution. The brown band in the plot indicates the relic density inferred by CMB experiments, $\Omega_\chi h^2 = 0.1188 \pm 0.0010$ [4].

We first focus only on neutralino annihilation processes (dashed lines in the figure). We denote the relic density which is computed by only considering the tree level processes by σ_0 (dashed red line). The dashed blue line labeled as σ_0+VIB denotes that VIB contribution is added to the tree level cross section. Finally, $\sigma^{\rm full}$ (dashed black line) denotes the QCD corrected cross-section. In $\sigma^{\rm full}$, we include $\sigma^{\rm simp}_{\rm tot} + \sigma^{\rm VIB}_{\chi\chi\to q\bar{q}g}$ and also the $\mathcal{O}(\alpha_s^2)$ process of gluon pair production, which is unsuppressed in the zero velocity limit. We see that in the region $m_\chi < m_t$, VIB increases the total annihilation rate and there is a visible change in the relic density. We also note that the gluon pair production further increases the total annihilation rate and is thus important. For $m_\chi \gtrsim m_t$, the dominant contribution comes from top quark production, which is not helicity suppressed. In this region, $\sigma^0_{\chi\chi\to t\bar{t}g}$ and $\sigma^0_{\chi\chi\to gg}$ are sub-dominant contributions and a significant decrease in relic density is brought by $\sigma^{\rm simp}_{\rm tot}$ (see Fig. 7.5).

We have seen that for $m_\chi \sim m_{\tilde{q}}$, VIB enhances the total annihilation rate. But in the same limit, neutralino co-annihilations with squarks can also significantly increase the annihilation rate (see section 5.2). We now include co-annihilations in the computation (depicted by solid lines in Fig. 7.6). In the figure, we see that for a given m_χ, squark co-annihilations dominate the annihilation rate and have a

[6]The implementation is now available in public DarkSUSY 6.0.0.

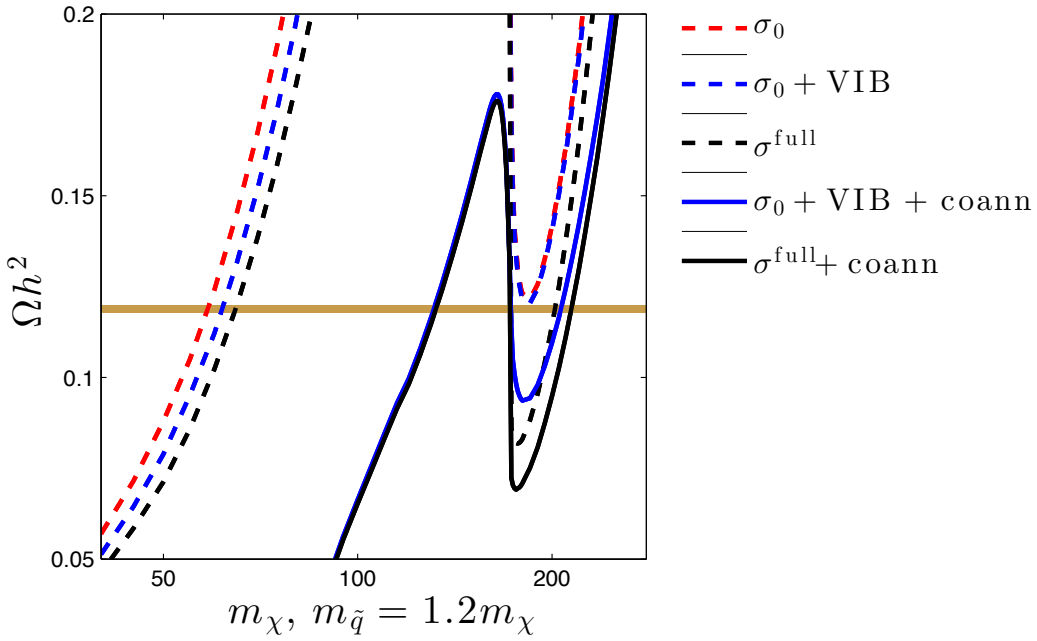

Figure 7.6: $\Omega_\chi h^2$ vs m_χ for a pure Bino model with the squark masses fixed to be $1.2m_\chi$. The brown bands shows the 1σ limits on CDM relic density [4]. Figure taken from paper I [21].

much larger effect than VIB. Thus, co-annihilations inevitably wash out the VIB enhancements and the latter are therefore not important for relic density calculations. Comparing the solid blue and black lines, we can also see that around top-threshold, QCD loop corrections ($\sigma_{\mathrm{tot}}^{\mathrm{simp}}$) are important and cannot be ignored in relic density computations. Neutralino squark co-annihilations have been studied with a lot of interest in the literature (see for example [103, 164–173]). As can be seen in the figure, co-annihilations increase the upper limit of m_χ for which a cosmologically interesting relic density is achievable, and are thus important for evading the LHC constraints for a model.

Though VIB is not an important process in setting the relic density, it is very important from the prospective of indirect detection. This is due to the fact that at very low temperatures co-annihilations become ineffective (see equation 5.11). Thus at present times due to the velocity suppressed $p-$wave and suppressed co-annihilations, gluon VIB dominates the total annihilation cross section in a degenerate squark scenario. In paper I [21], we also studied the impact of gluon

VIB on indirect detection. In addition to the two quarks, the final-state gluon also fragments into lower-energy particles. Inclusion of $\bar{q}qg$ final states improves the anti-proton and gamma-ray limits. Also, indirect detection of degenerate squark scenario is complementary to direct searches. The jets produced in LHC for an almost degenerate squark scenario will be too soft to be detected and thus constitute blind spots in direct searches. With the inclusion of $\bar{q}qg$ final states, we found that the Binos with masses upto 92 GeV can be excluded by the PAMELA data [174].

Chapter 8

SIDM and small scale problems in ΛCDM

8.1 Outline

The ΛCDM paradigm which assumes DM to be cold and collisionless, provides a very good description of our universe at scales $\gtrsim 1\,\mathrm{Mpc}$. In section 3.3.1, we discussed that there do exist some discrepancies between observations and ΛCDM predictions on sub-Mpc scales. Though astrophysical solutions for explaining these discrepancies exist (see [14] for a recent review), it is interesting to note that some of the small-scale problems can also be solved by lifting the assumption of collisionless DM [15].

Self-interacting dark matter (SIDM) [15] can alleviate two of the long standing small scale discrepancies, namely the cusp vs. core and too big to fail (TBTF) problems. SIDM is assumed to scatter via exchanging a light mediator, which we will denote by $\tilde{\gamma}$. The self scatterings ($\chi\chi \rightarrow \chi\chi$) help in transferring kinetic energy from the outer (hotter) regions to the inner (colder) regions, thus reducing the central density. This helps in solving the cusp-core and TBTF problems [175–178]. The missing satellites problem can also be addressed by suppressing structure at small scales or equivalently delaying the kinetic decoupling to sub-keV temperatures [112, 179–183]. In a SIDM framework, late kinetic decoupling can be achieved if the mediator particle scatters very efficiently with the DM ($\chi\tilde{\gamma} \rightarrow \chi\tilde{\gamma}$) and keeps it in kinetic equilibrium until sub-keV temperatures (see [181, 184–188] and paper II [22]).

For making an impact on cusp-core and TBTF problems, SIDM self scatterings should have a very large cross-section $\sigma_{\chi\chi\to\chi\chi}/m_\chi \sim 0.1 - 10\,\mathrm{cm}^2/\mathrm{g}$ on dwarf scales [176–178, 189, 190]. For a reference to how large this value is, a typical WIMP has $\sigma^{\mathrm{WIMP}}_{\chi\chi\to\chi\chi}/m_\chi \sim \alpha_W^2/m_\chi^3 \sim 10^{-14}\,\mathrm{cm}^2/\mathrm{g}$. We thus see that SIDM cannot have standard WIMP-like interactions. As we will see later, the required large cross sections can be achieved in the SIDM framework for a DM weakly coupled ($\alpha_\chi \sim 0.01$) to a light mediator ($m_{\tilde{\gamma}} \sim 100\,\mathrm{MeV}$).

Very stringent constraints exist from various astrophysical observations on the maximal allowed value of $\sigma_{\chi\chi\to\chi\chi}/m_\chi$ (see [49] for a very recent review). There is no consensus regarding the maximal allowed value of the cross section but a value of $\sigma_{\chi\chi\to\chi\chi}/m_\chi \lesssim 1\,\mathrm{cm}^2/\mathrm{g}$ on cluster scales is largely consistent with the data [190]. On dwarf scales, there is a much weaker bound of $\sigma_{\chi\chi\to\chi\chi}/m_\chi \lesssim 10\,\mathrm{cm}^2/\mathrm{g}$ [178, 189, 191]. Usually, a constant $\sigma_{\chi\chi\to\chi\chi}$ is assumed for studying the impact of SIDM on astrophysics. This however is not the usual case. For example, a Yukawa coupling between DM and a light mediator results in a very strong velocity dependence of the self-scattering cross section— yielding smaller cross sections at cluster scales (large velocities) while having larger cross sections at dwarf scales (smaller velocities). Thus, a Yukawa coupling can help evade stringent constraints at large scales while at the same time alleviate the problems on small scales [192].

The most stringent constraint on M_{cut} comes from the Lyman-α measurements, which robustly excludes $M_{\mathrm{cut}} \gtrsim 5.1 \times 10^{10} M_\odot$ [44, 45]. In this chapter, we will neglect the free-streaming effects and assume the cutoff to be generated solely by acoustic oscillations, which is typically the case for late kinetic decoupling of heavy DM.

In addition to solving the small scale problems, thermal production of DM is also possible in the SIDM paradigm. In section 8.2, we will discuss the three interactions describing the SIDM scenario: *annihilation* which sets the relic density, *self-scattering* which can solve cusp-core and TBTF problems and *scattering with the mediator* which keeps DM in kinetic equilibrium and sets the cutoff mass scale.

In paper II [22], we studied kinetic decoupling of simple SIDM models and classified the models into categories depending on whether late kinetic decoupling can occur or not. In paper III [23], we used CMB and other indirect detection

observations to constrain SIDM annihilation. In section 8.3, we will discuss the results of our paper II [22] and III [23].

8.2 SIDM interactions

As we discussed above, a Yukawa potential results in a velocity dependent self-scattering, a highly desirable quality in a model for evading constraints at large scales and helping to alleviate the small scale problems. Thus, a Yukawa coupling between DM and the mediator ($\mathcal{L} \supset -g_\chi \chi\chi\tilde{\gamma}$) has been a cornerstone in most of the SIDM models. Exceptions to this do exist. For example, in the perturbative limit, an effective quartic interaction of the type $\frac{\lambda}{4}\chi^2\tilde{\gamma}^2$ has a constant self-scattering cross section (see paper II [22]). In this chapter, we will primarily focus on the case of a Yukawa interaction between DM and the mediator and briefly comment on the extensions and other possible scenarios. The Yukawa potential is given by

$$V(r) = \pm\frac{\alpha_\chi}{r}e^{-m_{\tilde{\gamma}}r}\,, \tag{8.1}$$

where $\alpha_\chi (= g_\chi^2/4\pi)$ is the coupling constant and $+(-)$ denotes the repulsive (attractive) nature of potential. If $\tilde{\gamma}$ is a scalar, the potential is always attractive. On the other hand, for a vector $\tilde{\gamma}$ it is attractive for $\chi\bar{\chi}$ scattering and repulsive for $\chi\chi$ or $\bar{\chi}\bar{\chi}$ scattering.

8.2.1 Annihilation: $\chi\chi \to \tilde{\gamma}\tilde{\gamma}$

SIDM can be thermally produced if DM annihilates to $\tilde{\gamma}$ and the produced mediator particles subsequently decay to SM states [193]. Such a process is shown in the left panel of Fig. 8.1. The coupling of mediator particles to SM brings the dark and visible sector into thermal equilibrium and facilitates a decay which is necessary to avoid overclosing of the universe [194, 195].[1] The relic density can be calculated in the standard way as described in chapter 5.

As for typical WIMPs, SIDM will freezeout at $x_f \sim 25$, which corresponds to relative velocities of ~ 0.3. With the expanding universe, the DM speed decreases, and at very small DM velocities, the wave-function of the annihilating DM pair gets modified due to the exchange of light mediators (shown in the right

[1] The mediator particle can alternatively be coupled to a relativistic dark particle, for example, the sterile neutrinos. We will discuss this scenario in section 8.3.

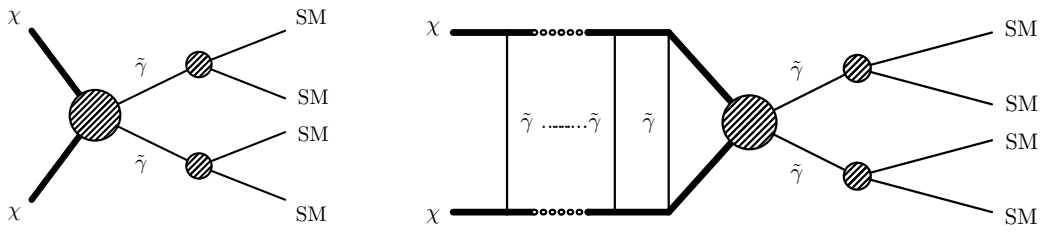

Figure 8.1: Feynman diagrams for SIDM annihilation. **Left: Early times.** DM annihilates to $\tilde{\gamma}$ and then $\tilde{\gamma}$ decays quickly to SM particles to avoid overclosing of the universe. The cross section in this limit can be calculated perturbatively. **Right: Late times.** At small relative velocities, the wave function of the annihilating DM pair gets modified due to the exchange of $\tilde{\gamma}$ particles. The cross section in this limit has to be calculated non-perturbatively [196,197].

panel of Fig. 8.1) and one needs to consider the non-perturbative effect known as *Sommerfeld* effect [196,197]. Sommerfeld effect can lead to very strong enhancements of the annihilation cross sections [197–200]. The enhancement is given by a velocity dependent Sommerfeld factor $S(v_{\rm rel})$, defined as

$$\sigma_{\chi\chi\to\tilde{\gamma}\tilde{\gamma}} v_{\rm rel} \equiv S(v_{\rm rel})\, \sigma^{\rm pert}_{\chi\chi\to\tilde{\gamma}\tilde{\gamma}} v_{\rm rel}\,, \tag{8.2}$$

where $\sigma^{\rm pert}_{\chi\chi\to\tilde{\gamma}\tilde{\gamma}}$ is the cross section in the perturbative limit.

The velocity dependence of the enhancement can be intuitively understood by considering a classical point particle colliding with an object of mass M and radius R (the example taken from [197]). In the absence of any forces, the cross section for the collision is $\sigma = \pi R^2$. Considering the gravitation potential generated by the target object will modify the cross section as $\sigma = \pi R^2 \left(1 + \frac{2GM}{Rv^2}\right)$. This behavior is expected as the test particles with large velocities can escape the potential while the particles with smaller velocities will fall more easily into the potential well. Thus the leading term for highly non-relativistic test particles has $\langle\sigma v\rangle \propto 1/v$ dependence.

In general, S has to be computed numerically by solving the Schrödinger equation [197]. For the Yukawa case, analytic expressions for S can be be found by approximating the Yukawa potential with a Hulthén potential, $V_{\text{Hulthén}} = \pm\,\alpha_\chi \dfrac{\delta e^{-\delta r}}{1 - e^{-\delta r}}$ with $\delta \sim 1.55 m_{\tilde{\gamma}}$. The Sommerfeld factor for $s-$wave annihilation is given

by [200]

$$S_s = \frac{\pi}{b}\frac{\sinh(2\pi bd)}{\cosh(2\pi bd) - \cos(2\pi\sqrt{d-b^2d^2})}\,, \tag{8.3}$$

where $b \equiv \dfrac{v_{\rm rel}}{2\alpha_\chi}$ and $d \equiv \dfrac{6\alpha_\chi m_\chi}{\pi^2 m_{\tilde{\gamma}}}$. For the $p-$wave annihilation, it is [200]

$$S_p = \frac{(d-1)^2 + 4b^2d^2}{1+2b^2d^2} \times S_s\,. \tag{8.4}$$

For this thesis there are three important points to note for the above expressions—

- **Saturation:** The Sommerfeld factors increase with decreasing $v_{\rm rel}$ and saturate when $v_{\rm rel} \lesssim v_{\rm sat} \equiv m_{\tilde{\gamma}}/2m_\chi$ for both $s-$ and $p-$wave processes. The saturated values are

$$S_s^{\rm sat} \equiv \frac{\pi^2 d}{\sin^2[\sqrt{\pi^2 d}]} \quad \text{and} \quad S_p^{\rm sat} \equiv \frac{\pi^2 d(d-1)^2}{\sin^2[\sqrt{\pi^2 d}]}\,. \tag{8.5}$$

  The saturation occurs due to the finite range of the potential. Specifically, it occurs when the deBroglie wavelength of the DM particle $(m_\chi v_\chi)^{-1}$ becomes larger than the range of interaction $m_{\tilde{\gamma}}^{-1}$ [197].

- **Resonances:** The above expressions diverge when $m_{\tilde{\gamma}} = \dfrac{6\alpha_\chi m_\chi}{\pi^2 n_{\rm res}^2}$, where $n_{\rm res}$ is an integer.[2] These resonances occur due to the potential developing quasi-bound states for these specific values of $m_{\tilde{\gamma}}$, thus leading to large enhancements [197,198].

- **Scaling:** Before saturation, the Sommerfeld factors increase as $1/v_{\rm rel}^2$ when being very close to a resonance and as $1/v_{\rm rel}$ away from the resonances.

In Fig. 8.2, we show the Sommerfeld enhanced cross section for both $s-$wave (black lines) and $p-$wave (gray lines) annihilation as a function of the relative velocity. We have fixed $m_\chi = 1$ TeV and take the value of α_χ required for thermal production from [202].[3] We use solid and dashed lines to show the off-resonance

[2] The resulting large cross sections can even violate unitarity at small velocities [201]. This is due to the approximation of Yukawa potential as Hulthén potential. See [201] for a proper treatment.

[3] In absence of non-perturbative effects, α_χ can be fixed analytically using the relation 5.6, by requiring the abundance to be equal to the observed one. Sommerfeld effect slightly decreases the required value of α_χ for $m_\chi \gtrsim 1$ TeV [202]. This roughly corresponds to an $\mathcal{O}(1)$ change in α_χ for $m_\chi \gtrsim 1$ TeV [202].

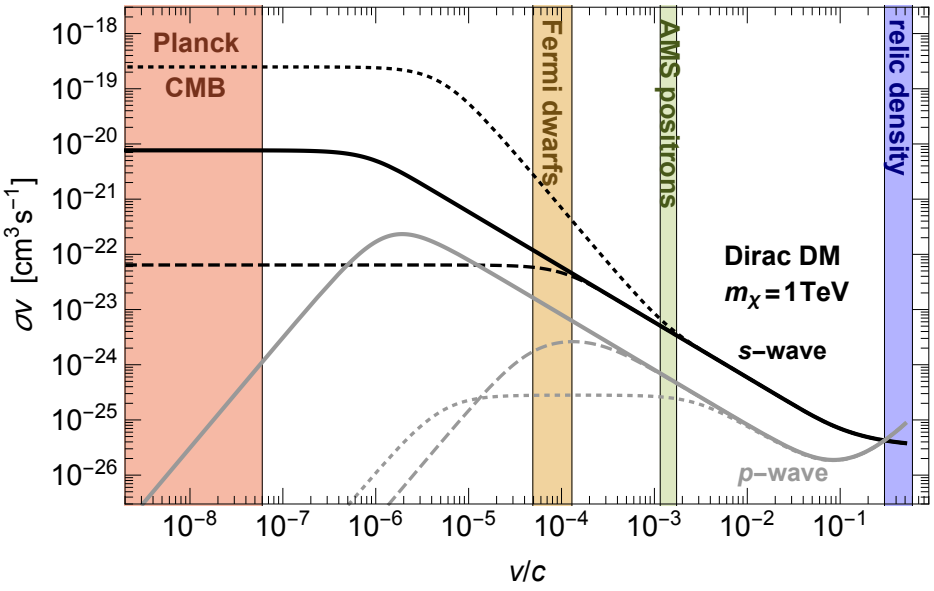

Figure 8.2: Sommerfeld enhanced s-wave and p-wave annihilation cross sections as a function of the relative velocity of the DM pair. The solid and dashed lines correspond to the fixed values of $m_{\tilde{\gamma}} = 1\,\mathrm{MeV}$ and $m_{\tilde{\gamma}} = 100\,\mathrm{MeV}$, respectively. The dotted lines show the resonant case with $m_{\tilde{\gamma}}$ tuned to 1.119 GeV (1.066 GeV) for s-wave (p-wave) annihilation. For each line, the coupling α_χ is fixed such that we get $\Omega_\chi h^2 \sim 0.12$ [4]. We also show the typical velocity ranges of different experimental probes as colored bars. Figure taken from paper III [23].

cases and thin dotted lines for the (almost) on-resonance case. On resonance, before the saturation occurs, the cross sections scale as $1/v_{\mathrm{rel}}^2$ and v_{rel}^0 for $s-$ and $p-$ wave respectively. Away from a resonance condition, the Sommerfeld factors increase as $1/v_{\mathrm{rel}}$, as mentioned above. After saturation has occurred, the cross section becomes constant for $s-$wave and starts decreasing as v_{rel}^2 for $p-$wave.

We can see that the annihilation cross sections get an enhancemnt of many orders of magnitude for the $s-$wave case. If at some point the annihilation rate becomes comparable to the Hubble rate, we can also have a second period of annihilations. Such large cross sections can be achieved for on-resonance scenarios [20, 203–205]. For such a case, we can decrease the relic abundance by many orders of magnitude. In this chapter, we do not consider such cases of being very close to a resonance. We will get back to the resonance scenario in chapter 9, when we discuss findings of our Paper IV [24]). We will also neglect bound state forma-

tion, which typically becomes important close to the unitary bounds [206, 207].

As briefly discussed in section 8.1, DM relative velocities depend on the size of the astrophysical structure. We will now consider how much the Sommerfeld factor increases the annihilation cross section in typical astrophysical structures of interest to this thesis. For doing so, we define an averaged cross section over a Maxwellian distribution

$$\langle \sigma_{\chi\chi\to\tilde{\gamma}\tilde{\gamma}} v_{\rm rel} \rangle_{v_M} \equiv \int d^3v \frac{e^{-v^2/2v_M^2}}{(\sqrt{2\pi}v_M)^3} \sigma_{\chi\chi\to\tilde{\gamma}\tilde{\gamma}} v_{\rm rel} \,, \tag{8.6}$$

where v_M is the most probable speed of a single particle in a halo of mass M. The typical most probable speeds encountered in dwarf galaxies, Milky Way size galaxies and galaxy clusters are $v_{\rm M} = 30,\ 220$ and $1000\,{\rm km/s}$, respectively.

In Fig. 8.3, we show the ratio $\frac{\langle \sigma_{\chi\chi\to\tilde{\gamma}\tilde{\gamma}} v_{\rm rel} \rangle_{v_M}}{\langle \sigma^{\rm pert}_{\chi\chi\to\tilde{\gamma}\tilde{\gamma}} v_{\rm rel} \rangle_{v_M}}$ as a function of the mediator mass for the three speeds of our interest. The peaks in the figure correspond to the values of $m_{\tilde{\gamma}}$ when the resonance condition is met. The slight shift in peak positions for $s-$ and $p-$wave cases is due to the different value of α_χ, which is fixed to get the observed relic density. The apparent larger enhancements for $p-$wave relative to $s-$wave are due to the fact that the perturbative cross section scales as v^2 for $p-$wave. As expected, for large values of $m_{\tilde{\gamma}}$, we see that there is no enhancement in the annihilation cross section at all scales. For very small mediator masses ($m_{\tilde{\gamma}} \ll m_\chi$) the enhancement factor becomes independent of the mediator mass. This is due to the fact that in the limit $m_{\tilde{\gamma}} \ll m_\chi$, we have $S_s \simeq 2\pi\alpha_\chi/v_{\rm rel}$.

We see that even away from resonances we will get significant enhancements for thermal SIDM at all scales. Such enhanced production of SM particles should thus be constrainable from indirect detection experiments. In paper III [23], we used Planck CMB data [4], gamma-ray data from Fermi-LAT [208] and positron data from AMS-02 [209, 210] to constrain annihilation in SIDM scenarios. We will now describe how CMB puts a very strong bound on the above described scenario.

Enhanced production of SM particles at late times necessarily alters the recombination history [211, 212]. CMB data from Planck [4] set a very strong limit

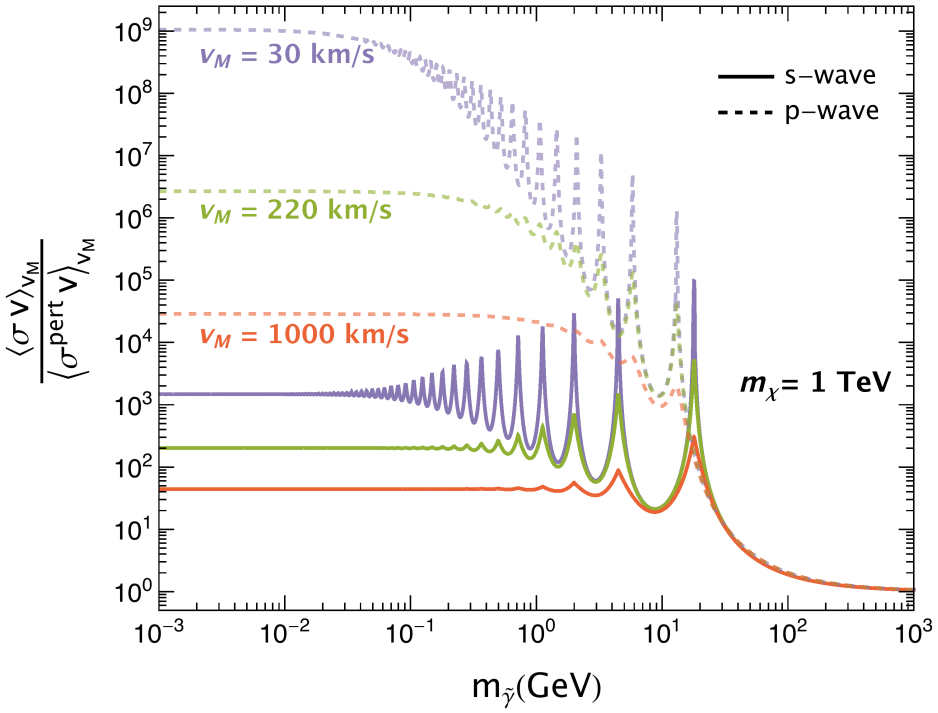

Figure 8.3: Velocity averaged Sommerfeld enhancements for the $s-$ and $p-$ wave annihilation. The chosen values of v_M are the typical most probable speeds of DM particles on dwarf galaxy scales ($v_M = 30\,\mathrm{km/s}$), Milky Way size galaxies ($v_M = 220\,\mathrm{km/s}$) and galaxy clusters ($v_M = 1000\,\mathrm{km/s}$). The value of α_χ is fixed for getting the observed relic density. See text for further details.

on the DM annihilation cross section

$$\frac{\langle\sigma_{\rm ann} v\rangle_{\rm rec}}{N_\chi} \lesssim 4\times 10^{-25}\ \mathrm{cm^3\,s^{-1}} \left(\frac{f_{\rm eff}}{0.1}\right)^{-1} \left(\frac{m_\chi}{100\,\mathrm{GeV}}\right)\,, \tag{8.7}$$

where $\langle\sigma_{\rm ann} v\rangle_{\rm rec}$ is the thermally averaged annihilation cross section at the epoch of recombination, $N_\chi = 1$ ($N_\chi = 2$) for Majorana (Dirac) DM and $f_{\rm eff}$ is the efficiency factor which models the fraction of energy injected into the intergalactic gas [213–215]. Other than neutrino final states, we have $f_{\rm eff} \gtrsim 0.1$ [215]. For a constant $\langle\sigma_{\chi\chi\to\tilde{\gamma}\tilde{\gamma}} v_{\rm rel}\rangle \sim 3\times 10^{-26}\mathrm{cm^3/s}$, the above expression implies the following upper bound on m_χ,

$$m_\chi \gtrsim 7.5 \left(\frac{f_{\rm eff}}{0.1}\right)\ \mathrm{GeV}\,. \tag{8.8}$$

Let us now investigate what the above bound (equation 8.7) implies for Sommerfeld enhanced annihilation. After kinetic decoupling, the DM velocity decreases as a^{-2} and thus the speed at the time of recombination can be calculated as

$$\langle v_\chi^2 \rangle_{\rm rec} = \frac{1}{2}\langle v_{\rm rel}^2 \rangle_{\rm rec} = \frac{3\,T_{\rm kd}}{m_\chi}\left(\frac{1+z_{\rm rec}}{1+z_{\rm kd}}\right)^2 \sim \frac{3\,T_{\rm rec}^2}{m_\chi T_{\rm kd}}\,. \tag{8.9}$$

As we mentioned in section 8.1, there exists an upper bound on $T_{\rm kd} \gtrsim 100\,{\rm eV}$ from the Lyman-α measurements [44, 45]. Using the above expression, we can thus see that the relative DM velocity at recombination has to be smaller than

$$v_{\rm rel}^{\rm rec} \lesssim 2\times 10^{-7}\left(\frac{m_\chi}{100\,{\rm GeV}}\right)^{-1/2}\,. \tag{8.10}$$

For models of our interest, the above value is much smaller than the velocities at which Sommerfeld enhancement saturates, $v_{\rm sat} = m_{\tilde\gamma}/2m_\chi$. We can now obtain the maximal allowed value for the saturated enhancement factor for $s-$wave annihilation (equation 8.5) using the above bound (equation 8.7),

$$1 \leq S_s^{\rm sat} \lesssim \frac{4}{30}\left(\frac{f_{\rm eff}}{0.1}\right)^{-1}\left(\frac{m_\chi}{1\,{\rm GeV}}\right)\,. \tag{8.11}$$

For $\alpha_\chi m_\chi/m_{\tilde\gamma} \ll 1$, we have $S^{\rm sat} \to 1$, and we recover the above limit for constant $\langle\sigma v\rangle \sim 3\times 10^{-26}{\rm cm}^3/{\rm s}$, $m_\chi \gtrsim 7.5\left(\frac{f_{\rm eff}}{0.1}\right)$ GeV. For $\alpha_\chi m_\chi/m_{\tilde\gamma} \gg 1$, the minimum value of a saturated Sommerfeld enhancement factor is $S_s^{\rm sat,min} = \pi^2 d = \frac{6\alpha_\chi m_\chi}{m_\phi}$. We can now obtain a lower bound on mediator mass in the limit $\alpha_\chi m_\chi/m_{\tilde\gamma} \gg 1$,

$$m_{\tilde\gamma} \gtrsim 0.16\left(\frac{f_{\rm eff}}{0.1}\right)\left(\frac{m_\chi}{100\,{\rm GeV}}\right)\,{\rm GeV}\,. \tag{8.12}$$

Note that this result holds for $m_\chi \gtrsim 7.5\left(\frac{f_{\rm eff}}{0.1}\right)$ GeV.

8.2.2 Self-scatterings: $\chi\chi \to \chi\chi$

As discussed in section 8.1, a large self-scattering cross section $\sigma_{\chi\chi\to\chi\chi}/m_\chi \sim 1\,{\rm cm}^2/{\rm g}$ can help in alleviating the cusp vs. core and TBTF problems. We show the Feynman diagram for self-scattering process in left panel of Fig. 8.4. In $N-$body simulations, self scattering of DM is usually implemented in terms of

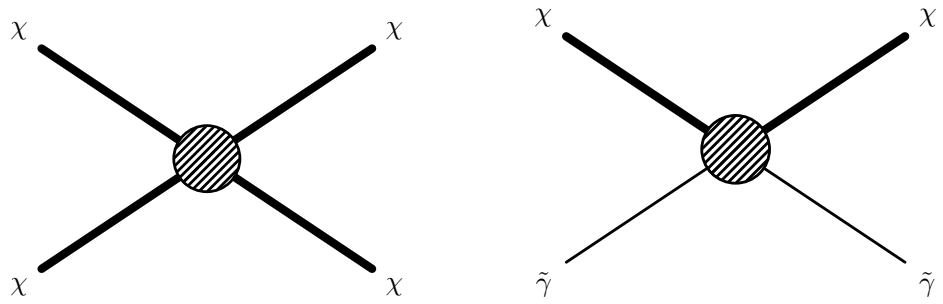

Figure 8.4: **Left:** Representative Feynman diagram for SIDM self-scattering. **Right:** Scattering of SIDM with the mediator $\tilde{\gamma}$.

the *transfer* cross section σ_T, defined as [202][4]

$$\sigma_T \equiv \int d\Omega \frac{d\sigma_{\chi\chi\to\chi\chi}}{d\Omega}(1-\cos\theta)\,, \tag{8.13}$$

where θ is the scattering angle in the COM frame. Typically, σ_T is a velocity dependent function. Like in the case of Sommerfeld effect, to study its effect on a halo of mass M, we average σ_T over a Maxwellian velocity distribution [216],

$$\langle\sigma_T\rangle_{v_{\rm M}} \equiv \int d^3v \frac{e^{-v^2/2v_{\rm M}^2}}{(\sqrt{2\pi}v_{\rm M})^3}\sigma_T(v)\,. \tag{8.14}$$

As mentioned in section 8.1, a Yukawa interaction leads to a very strong velocity dependence in σ_T. As was the case with annihilations, at small velocities the perturbative calculation of σ_T breaks down. For a Yukawa potential, we can get analytic expressions by dividing the parameter space into three regimes-

- ***Born*-limit** ($\alpha_\chi m_\chi \lesssim m_{\tilde{\gamma}}$): The parameter space $\alpha_\chi m_\chi \lesssim m_{\tilde{\gamma}}$ corresponds to a weak Yukawa potential and thus the Born approximation can be used in this regime to calculate σ_T perturbatively as [217]

$$\sigma_T^{\rm Born} = \frac{8\pi\alpha_\chi^2}{m_\chi^2 v_{\rm rel}^4}\left(\ln\left[1+\frac{m_\chi^2 v_{\rm rel}^2}{m_{\tilde{\gamma}}^2}\right] - \frac{m_\chi^2 v_{\rm rel}^2}{m_{\tilde{\gamma}}^2 + m_\chi^2 v_{\rm rel}^2}\right)\,. \tag{8.15}$$

[4]Transfer cross section σ_T does not get any contribution from the forward-scatterings ($\cos\theta \to 1$), which for our purpose are not relevant as they do not change the trajectories of scattering DM particles.

Note that the above expression is the same for both attractive and repulsive potentials.

- ***Classical*-limit** ($m_\chi v_{\rm rel} \gtrsim m_{\tilde\gamma}$): This parameter space corresponds to the region where the interaction range of the potential $(m_{\tilde\gamma}^{-1})$ is larger than the deBroglie wavelength of DM particles $(m_\chi v_\chi)^{-1}$ and thus quantum effects are sub-dominant. In this non-perturbative regime one can obtain parametric expressions for σ_T by studying classical particles moving in a Yukawa potential (see for example [218]). For an attractive potential one gets [216]

$$\sigma_T^- = \frac{\pi}{m_{\tilde\gamma}^2} \times \begin{cases} 2\,\beta^2 \ln[1+\beta^{-2}] & \beta \lesssim 10^{-2}, \\ \frac{7\beta^{1.8}+1960(\beta/10)^{10.3}}{1+1.4\beta+0.006\beta^4+160(\beta/10)^{10}} & 10^{-2} \lesssim \beta \lesssim 10^2\,, \\ 0.81\,(1+\ln\beta-(2\ln\beta)^{-1})^2 & \beta \gtrsim 10^2\,, \end{cases} \tag{8.16}$$

where $\beta \equiv 2\alpha_\chi m_{\tilde\gamma}/(m_\chi v_{\rm rel}^2)$. And for a repulsive potential we have [216]

$$\sigma_T^+ = \frac{\pi}{m_{\tilde\gamma}^2} \times \begin{cases} 2\beta^2 \ln[1+\beta^{-2}] & \beta \lesssim 10^{-2}, \\ \frac{8\beta^{1.8}}{1+5\beta^{0.9}+0.85\beta^{1.6}} & 10^{-2} \lesssim \beta \lesssim 10^4\,. \\ (\ln 2\beta - \ln\ln 2\beta)^2 & \beta \gtrsim 10^4 \end{cases} \tag{8.17}$$

- **Quantum *resonant* regime** ($m_\chi v_{\rm rel} \lesssim m_{\tilde\gamma}$ and $m_{\tilde\gamma} \lesssim \alpha_\chi m_\chi$): In this intermediate regime there are both quantum and non-perturbative effects present and we do not have an analytic result for σ_T for the Yukawa potential. Similar to the annihilation case, by approximating the Yukawa potential by a Hulthén potential we can get the following analytic expression for $L=0$ state in this regime [202] —

$$\sigma_T^{\rm Hulthén} = \frac{16\pi}{m_\chi v_{\rm rel}^2} \sin^2\left({\rm Arg}\left[\frac{i\Gamma[i\Theta v_{\rm rel}]}{\Gamma[\lambda_+]\,\Gamma[\lambda_-]}\right]\right), \tag{8.18}$$

where $\Theta \equiv \dfrac{m_\chi}{\sqrt{2\zeta(3)}m_{\tilde\gamma}}$ and $\lambda_\pm \equiv 1 + i\Theta v_{\rm rel}/2 \pm \sqrt{\alpha_\chi\Theta - \Theta^2 v_{\rm rel}^2/4}$ for an attractive potential and $\lambda_\pm \equiv 1 + i\Theta v_{\rm rel}/2 \pm i\sqrt{\alpha_\chi\Theta + \Theta^2 v_{\rm rel}^2/4}$ for a repulsive potential.

In Fig. 8.5, we show $\langle\sigma_T\rangle_{v_{\rm M}}$ as a function of $m_{\tilde\gamma}$ for three characteristic values of $v_{\rm M} = 30\,, 220\,\&\,1000\,{\rm km/s}$. In the plot, we can identify the Classical(Born)

regime as the region of smaller(larger) mediator masses. The intermediate region corresponds to the quantum-resonant regime. For an attractive potential, as in the case of Sommerfeld enhancement, we see resonances at $m_{\tilde{\gamma}} \sim \frac{6\alpha_\chi m_\chi}{\pi^2 n_{\rm res}^2}$. For the repulsive case, we have a smooth increase with a decrease in mediator mass. The blue band shows the region $\langle\sigma_T\rangle_{30}/m_\chi \sim 0.1$–$10\,{\rm cm}^2\,{\rm g}^{-1}$ which can alleviate the cusp-core and TBTF problems [177, 189]. We can see from the figure that for a TeV scale DM particle we need the mediator mass to be in the range $1 - 10\,{\rm MeV}$ for solving the small scale problems and we are in the classical regime. For smaller DM masses $\mathcal{O}({\rm GeV})$, the required σ_T will be instead be achieved in the Born regime. This is due to the steep $m_{\tilde{\gamma}}^{-4}$ scaling of the Born cross section for small velocities. For intermediate DM masses, we will find the resonant regime to give the desired σ_T. In Fig. 8.7, we show the parameter region in the m_χ vs. $m_{\tilde{\gamma}}$ plane for getting $\sigma_T/m_\chi \sim 0.1 - 10\,{\rm cm}^2/{\rm g}$ as blue bands.

8.2.3 Scattering with a relativistic partner: $\chi\tilde{\gamma} \to \chi\tilde{\gamma}$

As discussed in chapter 6, the scattering of DM with $\tilde{\gamma}$ (right panel of Fig. 8.4) keeps DM in equilibrium at early times and produces a cutoff at small scales in the matter power spectrum. For solving the Missing satellites problem, one needs to have $M_{\rm cut} \sim 10^{10} M_\odot$ [181, 219], which for the CDM/SIDM scenario (using equation 6.9) corresponds to kinetic decoupling temperatures $\sim 200\,{\rm eV}$. The required cutoff mass is many orders of magnitude larger than what one finds in the standard WIMP paradigm, $M_{\rm cut}^{\rm WIMP} = 10^{-11} M_\odot - 10^{-3} M_\odot$ [115]. We thus need very efficient scatterings between DM and the relativistic partner to keep DM in kinetic equilibrium until very small temperatures ($\sim$ sub-keV) to address the missing satellites problem. We can find an analytic expression for $M_{\rm cut}$ by using equations 6.7 and 6.9 to get

$$M_{\rm cut} \equiv M_n\, \xi^{3\frac{n+4}{n+2}} \left(\frac{c_n}{0.001}\right)^{\frac{3}{n+2}} \left(\frac{g_{\rm eff}}{3.36}\right)^{-\frac{3}{4+2n}} \left(\frac{m_\chi}{100\,{\rm GeV}}\right)^{-3\frac{n+3}{n+2}}, \qquad (8.19)$$

where M_n is a numerical constant (shown in Fig. 8.6) which depends only on n and bosonic/fermionic nature of $\tilde{\gamma}$.[5] Note that the above analytic expression is valid only for $n > -1$.

CMB observations put stringent constrains on an additional DR component, with $\Delta N_{\rm eff} > 1$ robustly excluded. For $\tilde{\gamma}$, this implies that $\rho_{\tilde{\gamma}} < \rho_{1\nu}$ or $\xi <$

[5] See the definition of γ_n used in equation 6.8.

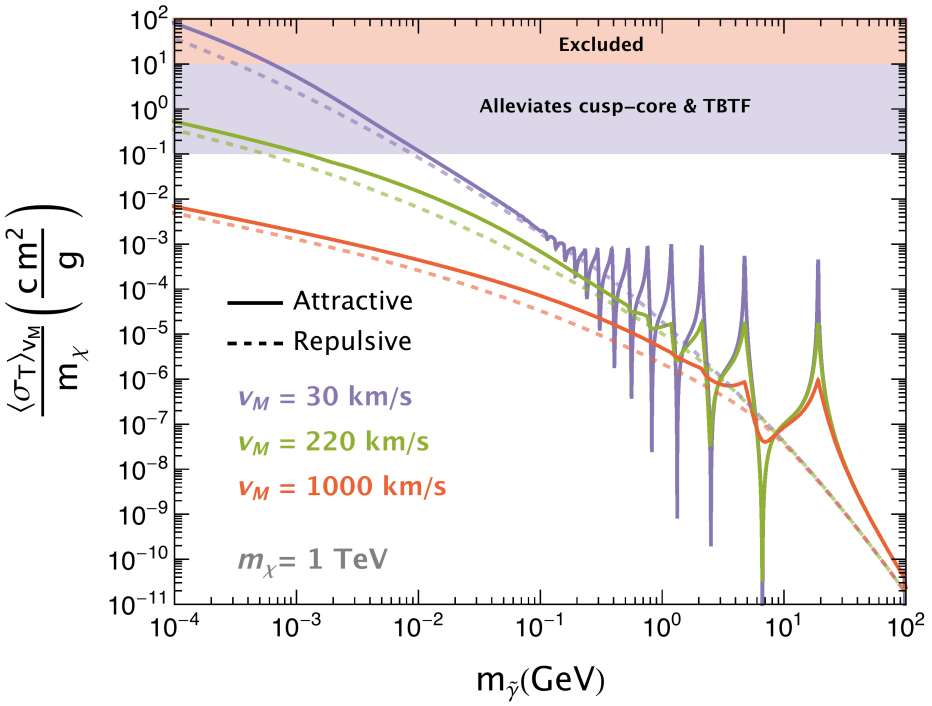

Figure 8.5: $\langle\sigma_T\rangle_{v_M}/m_\chi$ as a function of $m_{\tilde{\gamma}}$ for the three speeds of our interest $30, 220$ and $1000\,\mathrm{km/s}$ shown as blue, green and red lines, respectively. The corresponding solid(dashed) lines are for attractive(repulsive) Yukawa potential. We have fixed $m_\chi = 1\,\mathrm{TeV}$ and the coupling α_χ such that we get $\Omega_\chi h^2 \sim 0.12$. The blue band shows the values of $\langle\sigma_T\rangle_{30}/m_\chi \sim 0.1 - 10\,\mathrm{cm^2/g}$ required to alleviate cusp-core and Too big to fail (TBTF) problems [176–178, 189, 190]. The red band shows the values of cross section $\langle\sigma_T\rangle_{30}/m_\chi > 10\,\mathrm{cm^2/g}$ that are excluded by data [178, 189, 191]. See text for further details.

$0.85(0.82)/g_{\tilde{\gamma}}^{1/4}$ for a fermionic(bosonic) $\tilde{\gamma}$. Thus, $M_{\rm cut}$ is further suppressed as compared to the $\xi = 1$ case. An additional DR component also changes the effective relativistic degrees of freedom $g_{\rm eff}$. For simplicity, we fix $\xi = 1$ and $g_{\rm eff} = 3.36$ for the rest of this chapter.

The parameter c_n will depend on m_χ, $m_{\tilde{\gamma}}$ and the couplings and thus is not an independent parameter. We can put constraints on the maximal allowed values of c_n by using the inherently related annihilation and self-scattering processes. Let us first see how DM annihilation can be used to constrain c_n. Consider a simple example of scalar χ and $\tilde{\gamma}$ scattering via a point-like interaction $\mathcal{L} \supset -\frac{\lambda}{4}\chi^2\tilde{\gamma}^2$. The quartic interaction leads to a constant scattering amplitude ($|\mathcal{M}_{\chi\tilde{\gamma}\to\chi\tilde{\gamma}}|^2 = \lambda^2$) and

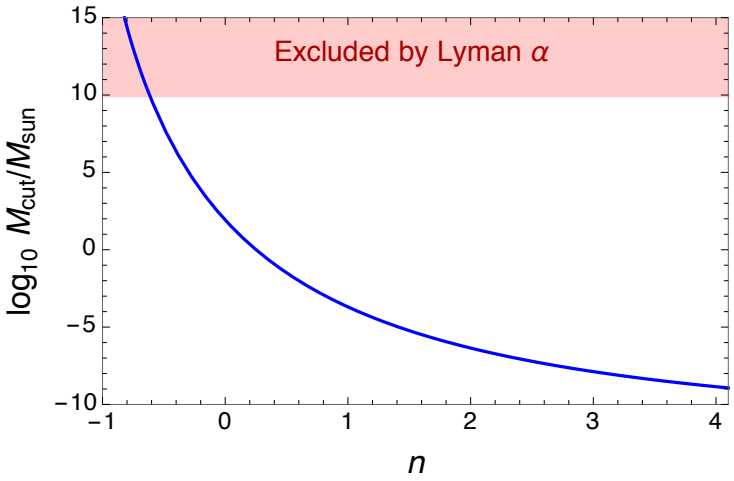

Figure 8.6: M_n as a function of n. We have fixed $c_n = 0.001$, $g_{\rm eff} = 3.36$, $\xi = 1$ and $m_\chi = 100\,\mathrm{GeV}$ in the analytic expression 8.19 for $M_{\rm cut}$ to plot M_n. We have also shown the region which is excluded by the Lyman-α data. Figure taken from paper II [22].

hence we have $n = 0$. Using expression 8.19, we get the following result for $M_{\rm cut}$

$$M_{\rm cut} \simeq 8.4 \times 10^{10} \lambda^3 \left(\frac{m_\chi}{10\,\mathrm{GeV}}\right)^{-9/2} M_\odot\,. \tag{8.20}$$

The above result implies that a GeV scale DM scattering via a quartic interaction can indeed produce the desired large cutoff. Requiring that the annihilation process ($\chi\chi \to \tilde\gamma\tilde\gamma$) produces the observed relic abundance, i.e. $\langle\sigma_{\chi\chi\to\tilde\gamma\tilde\gamma} v_{\rm rel}\rangle \sim 3 \times 10^{-26}\,\mathrm{cm}^3/\mathrm{s}$, we get

$$M^{4S}_{\rm cut} \sim 3 \times 10^{10} \left(\frac{m_\chi}{\mathrm{MeV}}\right)^{-3/2} M_\odot\,, \tag{8.21}$$

where we have used equation 5.8 and $\sigma_{\chi\chi\to\tilde\gamma\tilde\gamma} v_{\rm rel} = \lambda^2/(32\pi m_\chi^2)$ to fix the value of λ as a function of m_χ. We see that a lighter DM ($m_\chi \sim$ MeV) is needed in such a model to produce the desired cutoff. If $\tilde\gamma$ decays only to SM particles, such small DM masses are going to be ruled out by the CMB bound on DM annihilation (equation 8.8). Unless $\tilde\gamma$ is very light ($\lesssim$ eV) to avoid overclosing of the universe or it decays to even lighter dark species, such a simple model cannot have thermal production and produce large cutoff for the same parameter values.

For models with efficient self-interactions, like for the Yukawa potential between χ and $\tilde\gamma$, a stronger constraint can be put on c_n using $\langle\sigma_T\rangle_{30} \lesssim 10\,\mathrm{cm}^2/\mathrm{g}$.

As we are interested in (sub-)keV scale $m_{\tilde{\gamma}}$ and GeV DM for getting late kinetic decoupling, we can find a very simple scaling by averaging σ_T in the classical regime for the case of Yukawa potential ($\beta \lesssim 10^{-2}$ cases of equations 8.16 & 8.17),

$$\frac{\langle\sigma_T\rangle_{30}}{m_\chi} \sim 5.3 \left(\frac{\alpha_\chi}{10^{-5}}\right)^{1.5} \left(\frac{m_\chi}{100\,\mathrm{GeV}}\right)^{-2.5} \left(\frac{m_{\tilde{\gamma}}}{\mathrm{keV}}\right)^{-0.5} \frac{\mathrm{cm}^2}{\mathrm{g}}\,, \tag{8.22}$$

which we find to be a good fit for DM masses larger than

$$m_\chi \gtrsim \frac{m_{\tilde{\gamma}}}{100\,\mathrm{eV}}\ \max\left[1, \frac{1}{10^7 \alpha_\chi}\right] \mathrm{GeV}\,. \tag{8.23}$$

Using the constraint on dwarf scales $\langle\sigma_T\rangle_{30} \lesssim 10\,\mathrm{cm}^2/\mathrm{g}$, we get

$$\alpha_\chi \lesssim 4 \times 10^{-3} \left(\frac{m_{\tilde{\gamma}}}{\mathrm{keV}}\right)^{1/3} \left(\frac{m_\chi}{100\,\mathrm{GeV}}\right)^{5/3}\,. \tag{8.24}$$

We can now get the maximal allowed value of the cutoff as

$$M_{\mathrm{cut}} \lesssim M_n \left(\frac{c_n}{10^5\,\alpha_\chi^2}\right)^{\frac{3}{n+2}} \left(\frac{m_\chi}{100\,\mathrm{GeV}}\right)^{\frac{1-3n}{n+2}} \left(\frac{m_{\tilde{\gamma}}}{\mathrm{keV}}\right)^{\frac{2}{n+2}}\,. \tag{8.25}$$

Let us now apply the above constraint for the Yukawa model we described above. As we only have a $\chi\chi\tilde{\gamma}$ coupling in this model, scattering of χ with $\tilde{\gamma}$ will necessarily proceed via s/u channel exchange of χ. In terms of paper II's [22] terminology, such models fall under the *exclusive s/u channel scattering* in *2-particle models* described in the paper. For a (Dirac) fermionic DM and vector $\tilde{\gamma}$, the averaged scattering amplitude squared is

$$\langle|\mathcal{M}_{\chi\tilde{\gamma}\to\chi\tilde{\gamma}}|^2\rangle_t = \frac{1024\pi^2\alpha_\chi^2}{3}\,. \tag{8.26}$$

Using the self interaction constraint from equation 8.25, we find that the M_{cut} has to be smaller than

$$M_{\mathrm{cut}} \lesssim 2.5 \times 10^{-6} \left(\frac{m_{\tilde{\gamma}}}{\mathrm{keV}}\right) \left(\frac{m_\chi}{100\,\mathrm{GeV}}\right)^{1/2} M_\odot\,. \tag{8.27}$$

Thus, we see that a large cutoff mass cannot be achieved in the simplest possible setting of Yukawa mediated SIDM.

8.3 Discussion

In paper II [22], we classified the simplest models that can have late kinetic decoupling of DM. We considered two classes of models. Firstly, the *2-particle* models involving only two particles in the dark sector χ and $\tilde{\gamma}$. Secondly, the *3-particle* models with an additional particle mediating interactions between χ and $\tilde{\gamma}$. For DM to be stable, we assumed DM to be charged under a Z_2 symmetry and we considered only renormalizable interactions. We allowed our dark sector particles to be scalars, Dirac fermions or vector particles. We assumed a vector particle to be associated with a gauge symmetry.

In paper III [23], we considered CMB constraints on SIDM annihilation at the epoch of recombination. We found that the CMB (and partially other indirect detection) constraints on $s-$wave annihilation rule out the desired parameter space to address cusp-core and TBTF problems.

We will now briefly summarize our findings of paper II [22] and III [23] by working with a representative SIDM model with a Yukawa interaction between DM and $\tilde{\gamma}$. SIDM annihilation can proceed via $s-$wave or a $p-$wave. For example, for a fermionic DM interacting with a scalar $\tilde{\gamma}$ ($\mathcal{L} \supset -g_\chi^S \bar{\chi}\tilde{\gamma}\chi$), the annihilation will be $p-$wave. On the other hand for a vector $\tilde{\gamma}$ ($\mathcal{L} \supset -g_\chi^V \bar{\chi}\gamma^\mu\tilde{\gamma}_\mu\chi$), it will be $s-$wave annihilation. From Fig. 8.2, we can see that at the time of recombination, S_p will be typically saturated and the $p-$wave cross section will start decreasing as $1/v_{\rm rel}^2$. Thus, it is only the $s-$wave annihilation that can be constrained by the CMB bound (equation 8.7) and we will now focus on the case of a vector mediator. The mediator can interact with the SM particles, for example, via kinetic mixing with the hypercharge field strength $B^{\mu\nu}$ or via mass mixing with Z boson [220–222]—

$$\mathcal{L} \supset -g_\chi^{\rm V}\tilde{\gamma}^\mu\bar{\chi}\gamma_\mu\chi - \frac{1}{2}\sin\epsilon\, B_{\mu\nu}\tilde{\gamma}^{\mu\nu} - \delta m^2\tilde{\gamma}^\mu Z_\mu\ . \tag{8.28}$$

where ϵ and δm are the mixing parameters. In paper III [23], we covered three cases. Firstly, the coupling of mediator to SM sector is mainly via kinetic mixing, i.e. $\delta m \ll m_{\tilde{\gamma}}$. Secondly, the coupling is mainly via mass mixing, i.e. $\delta m/m_Z \gg \epsilon$ and lastly for a mediator having a different temperature than the SM heat bath, i.e. $\xi \neq 1$. In this thesis, we will mainly focus on the first case and comment on our findings for the other two cases.

In addition to the CMB bound, we also used gamma-ray data from Fermi-LAT [208] and positron from AMS-02 [209, 210]. For simplicity, we considered only leptonic decay modes $\tilde{\gamma} \to \ell\ell$, as the inclusion of other decay modes will lead to even more stringent constraints. For implementing AMS data, we used the bounds derived by Elor et al. [223] on one-step cascade annihilations, with the mediator particle decaying to e^+e^- and $\mu^+\mu^-$. The bounds extend down to masses of $m_\chi > 10\,\mathrm{GeV}$ and for the parameter space of our interest ($m_\chi \gg m_{\tilde{\gamma}}$) are independent of the mediator mass.

In Fig. 8.7, we show the preferred region in the m_χ and $m_{\tilde{\gamma}}$ plane for having $\sigma_T/m_\chi \sim 0.1 - 10\,\mathrm{cm}^2/\mathrm{g}$ as blue bands. We see that the region required to address cusp-core and TBTF problem is ruled out primarily by CMB data. For each point in the plot, we calculated the Sommerfeld enhanced annihilation cross section with the DM relative velocity set to the conservative maximal allowed value of $v_{\mathrm{rel}}^{\mathrm{rec}}$ (equation 8.10). The values of f_{eff} for each decay mode were taken from [215].

The region $m_{\tilde{\gamma}} < 2m_e$ is excluded as it will either overclose the universe or the only active decay mode $\tilde{\gamma} \to 3\gamma$ will be in conflict with the gamma ray observations [224]. The constraints on this region of parameter space can be relaxed if the mediator particles couple to neutrinos or some other very light dark species (for example sterile neutrinos). Coupling to neutrinos is possible in the case of mass-mixing and thus the region $m_{\tilde{\gamma}} < 2m_e$ will be allowed for $\delta m/m_Z \gg \epsilon$.

For the figure, we assumed DM to have thermal contact with SM sector at high temperatures. In the scenario when dark and visible sector starts to evolve differently at later times, i.e. $\xi < 1$, we found the bounds to be slightly less stringent, but the desired parameter space to achieve $\langle\sigma_T\rangle_{30}/m_\chi \sim 0.1-10\,\mathrm{cm}^2/\mathrm{g}$ is still strongly ruled out.

In subsection 8.2.3, we saw that a model with just the Yukawa coupling cannot result in a large cutoff mass (equation 8.27). This was due to the strong self interaction constraints. We will now discuss some basic extensions of this model that we considered in paper II [22]. An addition to the simple scenario is to allow for a cubic interaction of $\tilde{\gamma}$. The new coupling results in a new $t-$channel diagram with $\tilde{\gamma}$ as the mediator. This results in an enhanced scattering rate, as the t channel propagator is almost on-shell. For such models, we found $n < -1$, thus our analytic solution for M_{cut} (equation 8.19) is not applicable and we have to numerically solve equation 6.5 for T_{kd}. We found that $M_{\mathrm{cut}} = 10^{10} M_\odot$ can be achieved

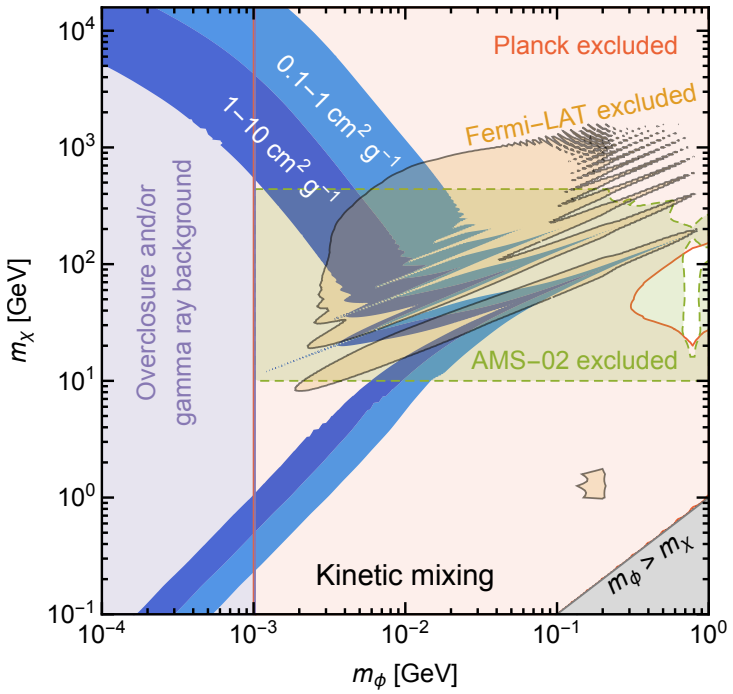

Figure 8.7: Constraints on SIDM annihilation to vector mediators from CMB [4], Fermi-LAT [208] and AMS-02 [209, 210] in the DM mass vs. mediator mass plane. The blue shaded area shows the region where we have $0.1\ \mathrm{cm}^2\,\mathrm{g}^{-1} \leq \langle\sigma_T\rangle_{30}/m_\chi \leq 10\ \mathrm{cm}^2\,\mathrm{g}^{-1}$. We see that the parameter space for solving cusp-core and too big to fail problems is ruled out by the three experiments. Figure taken from paper III [23].

even for TeV scale DM with $m_{\tilde{\gamma}} \sim \mathrm{keV}$. However, due to self-interaction constraints, the maximal allowed value of α_χ/m_χ is too small to account for the observed relic density.

We can get around this problem by adding a new particle to the model. We denote the new particle by ϕ and has the mass hierarchy $m_\chi \gg m_\phi \gg m_{\tilde{\gamma}}$. Let us take the example of χ, ϕ and $\tilde{\gamma}$ being fermion, vector and fermion, respectively. And the interactions are given by $\mathcal{L} \supset -g_\chi \phi_\mu \bar{\chi}\gamma^\mu\chi - g_{\tilde{\gamma}}\phi_\mu\bar{\tilde{\gamma}}\gamma^\mu\tilde{\gamma}$. The scattering of χ and $\tilde{\gamma}$ now proceeds via the $t-$channel exchange of ϕ and the scattering amplitude for the model is

$$\langle|\mathcal{M}_{\chi\tilde{\gamma}\to\chi\tilde{\gamma}}|^2\rangle_t = \frac{256 g_\chi^2 g_{\tilde{\gamma}}^2 m_\chi^4}{3m_\phi^4}\frac{\omega^2}{m_\chi^2}\,. \tag{8.29}$$

We see that it is a $n = 2$ case and the scattering amplitude is enhanced by the factor m_χ^4/m_ϕ^4. Using equation 8.19, we get

$$M_{\rm cut} \simeq 112\,\pi^{3/2}\alpha_{\tilde{\gamma}}^{3/4}\left(\frac{m_\phi}{\rm MeV}\right)^{-3}\left(\frac{\alpha_\chi}{m_\chi/{\rm TeV}}\right)^{3/4} 10^{10} M_\odot\,. \tag{8.30}$$

The desired $M_{\rm cut} = 10^{10} M_\odot$ can indeed be achieved in this scenario due to the additional particle. Let us now see what such models predict for σ_T and $\Omega_\chi h^2$. We can fix α_χ by requiring the process $\chi\chi \to \phi\phi$ to produce the observed relic density. Neglecting the Sommerfeld enhancement for simplicity, we have $\langle\sigma_{\chi\chi\to\phi\phi} v_{\rm rel}\rangle = \pi\alpha_\chi^2/m_\chi^2 \sim 3\times10^{-26}\,{\rm cm}^3/{\rm s}$. We can see that with this requirement, the cutoff in the model is not dependent on α_χ and m_χ,[6] and the above expression becomes

$$M_{\rm cut} \sim 66\,\alpha_{\tilde{\gamma}}^{3/4}\left(\frac{m_\phi}{\rm MeV}\right)^{-3} 10^{10} M_\odot\,. \tag{8.31}$$

We can now achieve $M_{\rm cut} = 10^{10} M_\odot$ for various parameter combinations of m_ϕ and $\alpha_{\tilde{\gamma}}$ and produce the observed relic abundance. The self-interactions in this model are mediated by ϕ. We have already seen in Fig. 8.7 that for MeV scale mediators, $\langle\sigma_T\rangle_{30}/m_\chi \sim 0.1 - 10\,{\rm cm}^2/{\rm g}$ can be achieved for wide ranges of DM masses. The coupling $\alpha_{\tilde{\gamma}}$ can thus be tuned for a given m_ϕ to get $M_{\rm cut} = 10^{10} M_\odot$ and solve the other small scale problems simultaneously. In such a model, we can also evade the CMB constraints on DM annihilation, if our scattering partner $\tilde{\gamma}$ is very light $\lesssim$ eV.

The model we just discussed has been studied before to address the small scale problems [184,185,187,188,225]. In paper II [22], we discussed that such models belong to a more general class of models that can address all the small scale issues. DM scattering with a very light particle ($m_{\tilde{\gamma}} \ll$ MeV) via $t-$channel exchange of a MeV-scale particle with $n = 2$, results in $M_{\rm cut} \sim 10^{10} M_\odot$, $\langle\sigma_T/m_\chi\rangle_{30} \sim 1\,{\rm cm}^2/{\rm g}$ and $\Omega_\chi h^2 \sim 0.12$. The other models that we found to fall in this category are with $\chi - \phi - \tilde{\gamma}$ as, scalar-vector-scalar, scalar-scalar-fermion, scalar-vector-fermion, fermion-scalar-fermion and fermion-vector-scalar.

In addition to the above described class of models, we also discussed a co-annihilation-*like* scenario, when there is an additional particle (χ') slightly heavier

[6] Equation 8.30 will have a very weak dependence on m_χ through x_f. See paper II [22] for details.

than the DM, i.e. $\frac{m_{\chi'}-m_\chi}{m_\chi} \ll 1$. Such models could also achieve $M_{\rm cut} \sim 10^{10} M_\odot$ and $\Omega_\chi h^2 \sim 0.12$ for $m_\chi \sim \mathcal{O}(\mathrm{GeV})$. However, as the mediator particle is heavy, strong self-interactions could not be achieved for such models.

For studying the effect of cutoff and self-interactions on astrophysics, one has to perform N-body simulations for specific models. This is computationally quite expensive to do on a model to model basis. In addition to the above described classification, we also computed ETHOS parameters [116, 216] for all the models we discussed in our paper. Models with the same set of values of the parameters have an identical effect on cutoff mass scale and non-linear structure formation.

Chapter 9

Cosmological constraints on non-standard dark matter evolution

9.1 Outline

In chapter 5, we saw that after the chemical freeze out, the rate of change of the DM comoving number density is negligible. For $s-$wave annihilation, the annihilation rate scales as $n_\chi^{\rm eq}\langle\sigma v_{\rm rel}\rangle \propto a^{-3}$ and for $p-$wave it decreases even faster as a^{-5}. The small relative change of $a^3 n_\chi$ is due to the fact that the Hubble rate decreases much more slowly than the DM annihilation rate, i.e. as $a^{-2}(a^{-3/2})$ in the radiation (matter) dominated universe. As long as there is no other active mechanism that can deplete DM faster than the Hubble rate, it is a good approximation to assume $n_\chi a^3$ to be constant in the universe. We will now briefly discuss two scenarios where the comoving DM density can indeed decrease.

Decaying DM: In chapter 2, we discussed that DM should be stable on cosmological timescales. If DM consists of only one kind of particle, DM's lifetime needs to be more than the current age of the universe. An alternative to this is to consider that the total DM content of the universe is formed by multiple dark particles and some of these dark particles are stable and others decay [16–19]. Assuming that the (co-)annihilation processes have become inefficient for the decaying components (denoted collectively by subscript $_{\rm dDM}$) due to the reasons mentioned above, the number density of the decaying component follows the equation [19]

$$\frac{d\rho_\chi}{da} = -\frac{3}{a}\rho_\chi - \frac{1}{aH}\sum_i \Gamma^i_{\rm decay}\rho^i_{\rm dDM}\,, \tag{9.1}$$

where $\Gamma^i_{\rm decay}$ and $\rho_{\rm dDM}$ is the decay rate and the energy density of the ith decaying component, respectively and ρ_χ is the total DM density. One can see from the above equation that the comoving number density is roughly constant as long as $H \gg \Gamma_{\rm decay}$. Once the expansion rate of the universe falls below the decay rate of the species, the decays will result in a rapid decrease in the comoving number density.

Consider a scenario where the dark sector is composed of two kinds of particles, one is stable and the other decays with the decay rate $\Gamma_{\rm decay} = 0.2 H_{\rm eq}$, where $H_{\rm eq}$ is the Hubble rate at matter-radiation equality, i.e. at $z_{\rm eq} \sim 3400$ [4]. In Fig. 9.1, we show the density evolution of such a model as a function of the scale factor (solid black line). For illustration, we have assumed the unstable component to form about 13% of the total dark content. We see that the number density of the dark sector drops very quickly as compared to cosmological scales when the decay rate becomes comparable to the Hubble rate, which for our fixed value of $\Gamma_{\rm decay}$ corresponds to $a \sim 10^{-3}$. After the unstable component has decayed completely, the dark sector again has a constant comoving number density. We thus see that for a multi-component dark sector comprising of some stable components and some unstable components, the total number density will have step-like transitions. For multiple decaying dark particles, there will be multiple steps.

On-resonance Sommerfeld enhanced DM annihilation: After kinetic decoupling the momenta of a DM particle will redshift, implying $v \propto a^{-1}$. In the previous chapter, we saw that from the onset of Sommerfeld enhancement and before its saturation, the $s-$wave annihilation scales as $1/v$ for the off-resonance case and as $1/v^2$ for the on-resonance scenario. After kinetic decoupling this corresponds to the annihilation rate scaling as a^{-1} (a^{-2}) for on(off)-resonance scenario. We thus see that the annihilation rate can catch up with the Hubble rate for the on-resonance scenario. For such a scenario, we can thus have a *period of second annihilations* [20, 203–205].

In Fig. 9.1, we show the numerical solution of equation 4.15 for Sommerfeld enhanced $s-$wave annihilation for an (almost-)resonant scenario as the dashed black line.[1] We have used the following model parameter values- $T_{\rm kd} = 1\,{\rm keV}$, $\alpha_\chi = 0.01$, $m_\chi = 200\,{\rm GeV}$ and the mass of the mediator to be $\sim 15.2\,{\rm MeV}$,

[1] In paper IV [24], we calculated the thermal average of the annihilation cross section by as-

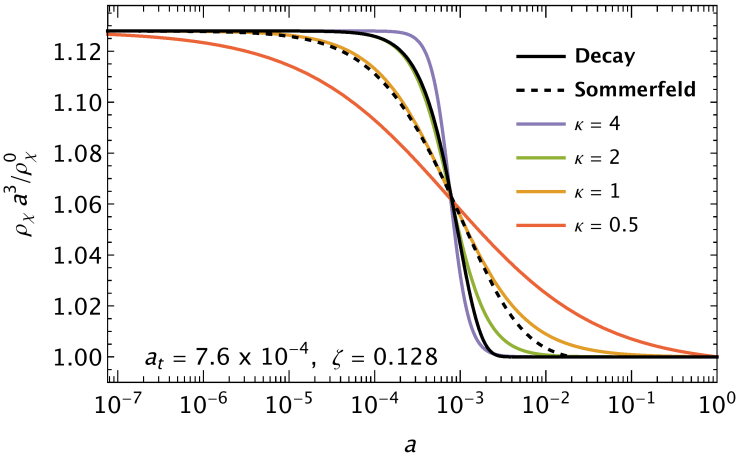

Figure 9.1: Evolution of DM comoving energy density as a function of scale factor for two illustrative examples of DM decay (solid black line) and resonant Sommerfeld annihilation (dashed black line). In addition to the two physics models, we have shown our parametrization (defined in equation 9.2) for four values of κ with ζ and a_t fixed for comparison with the shown decay and annihilation cases. We see that our simple parametrization provides a good approximation for the two physics models.

which corresponds to $n_{\rm res} = 10$. For solving the differential equation, we have used the boundary condition $\Omega_\chi^{z_{\rm rec}} h^2 = 0.1198$, where $z_{\rm rec} \equiv 1100$ is the redshift at recombination. We see that the on-resonant annihilation also results in a step-like transition in the DM comoving density. The parameter values for the decay case (solid black) and the on-resonance annihilation model (dashed black) were chosen such that the transition is centered at a similar time $a \sim 10^{-3}$ and the same amount of DM decreases $\sim$13%.

CMB probes the universe from very early to very late times and is very sensitive to the changes in the expansion rate. At times later than matter-radiation equality, CMB is also very sensitive to the amount of DM in the universe (for example through lensing effects). Thus, CMB can be used to probe the above mentioned scenarios. Unlike the case of the vanilla ΛCDM model, we do not have a simple evolution like $\rho_\chi \propto a^{-3}$ etc. For getting the constraints from CMB, one needs to solve the evolution of the dark sector on a model to model basis.

suming a Maxwellian velocity distribution. For the case of resonant annihilation, there is also a large enhancement in DM-self interactions. Thus, DM can indeed have a Maxwellian velocity distribution [20].

This means solving the coupled set of equations of particle number densities and the Hubble rate. For constraining the vanilla ΛCDM model, one has to scan over the six ΛCDM parameters (described in section 3.3). Like in the above mentioned cases of a modified cosmology, the parameter space increases even further. This becomes computationally very challenging owing to the large parameter space and solving the cosmic evolution on a model to model basis.

In paper IV [24], we proposed a parametric expression for the step-like transition, which covers the scenarios mentioned above and can be extended to even more general models. In section 9.2, we will describe our background parametrization and the resulting modified evolution of the perturbed quantities. The final products resulting from the above discussed depletions can be SM particles or some relativistic dark species. In the previous chapter we discussed that the production of SM particles at late times is strongly constrained by the CMB (see also [226]). To avoid these constraints, in paper IV [24] we assumed that DM depletes into some form of dark radiation. In section 9.3, we will describe our scanning setup and the datasets used in paper IV [24]. In section 9.4, we will summarize the findings of our paper IV [24] and discuss some of the subtleties involved in the analysis.

9.2 Phenomenological approach to varying comoving DM density

Background evolution

For modelling a step-like transition, we used the following parametrization for ρ_χ

$$\rho_\chi(a) = \frac{\rho_\chi^0}{a^3}\left[1 + \zeta\frac{1-a^\kappa}{1+(a/a_t)^\kappa}\right] , \tag{9.2}$$

where $\rho_\chi^0 \equiv \rho_\chi(1)$ is the DM density today and we have introduced three parameters a_t, κ and ζ describing *when is*, *how fast is* and the *height of* the transition, respectively. Concretely, a_t is the scale factor at which the transition of $\rho_\chi a^3$ from $(1+\zeta)\rho_\chi^0$ to ρ_χ^0 is centered and the steepness of the transition is determined by the parameter κ. In Fig. 9.1, we show the evolution of ρ_χ for four different values of κ as the four colored lines. The values of ζ and a_t shown in the plot are chosen for a direct comparison with the decay and Sommerfeld enhanced annihilation cases

we discussed above. We see that the Sommerfeld case is very well described by the $\kappa = 1$ line and decay can be modeled with $\kappa = 2$.

In the case when DM is converted to DR (denoted by ϕ), the energy densities of χ and ϕ follow the relation

$$a\frac{d\rho_\chi}{da} + 3\rho_\chi = -a\frac{d\rho_\phi}{da} - 4\rho_\phi \equiv \quad -\frac{\mathcal{Q}}{H} \tag{9.3}$$

where $\mathcal{Q} > 0$ is the momentum integrated collision term, for the case of annihilation it is $\mathcal{Q} = \langle\sigma v_{\rm rel}\rangle\rho_\chi^2/m_\chi$ and for decay it is $\mathcal{Q} = \Gamma_{\rm decay}\rho_\chi$. One can see that with our proposed parametrization, one does not need the explicit form of $\mathcal{Q}$ and H to solve equation 9.3 for ρ_ϕ. Using the boundary condition $\rho_\phi a^4 \xrightarrow{a\to 0} 0$, we find

$$\rho_\phi(a) = \frac{\zeta\rho_\chi^0}{a^3}\frac{(1+a_t^\kappa)}{(a^\kappa + a_t^\kappa)}\left((a^\kappa + a_t^\kappa)\ {}_2F_1\left[1, \frac{1}{\kappa}; 1+\frac{1}{\kappa}; -\left(\frac{a}{a_t}\right)^\kappa\right] - a_t^\kappa\right) . \tag{9.4}$$

The ordinary Hypergeometric function ${}_2F_1$ can be expressed in terms of simple analytic functions for $\kappa^{-1} = \frac{1}{2}, 1, 2, 3\ldots$. The existence of analytic expressions is highly desirable for a fast computation of such a model.

Unlike in the ΛCDM model, ρ_ϕ is a naturally varying quantity in our model. In order to facilitate a comparison with the literature we define a time-dependent quantity analogous to the constant $\Delta N_{\rm eff}$,

$$\Delta\tilde{N}_{\rm eff}(a) \equiv \frac{\rho_\phi(a)}{\rho_{1\nu}(a)} . \tag{9.5}$$

Using expression 9.4, one can see that for $\kappa > 1$, the comoving energy density $\rho_\phi a^4$ will approach a constant value for $a \gg a_t$. Thus, the above definition becomes equivalent to the conventionally used $\Delta N_{\rm eff}$ for $\kappa > 1$ & $a \gg a_t$.

In the top panel of Fig. 9.2, we show the evolution of the DR density as a function of the scale factor for the same values of a_t, ζ and κ we used in Fig. 9.1. We have also shown the corresponding values of $\tilde{N}_{\rm eff}$ on the second $y-$axis. We see that most of the DR is produced after $a \geq a_t$. In the bottom panel of the figure, we show the resulting change in the Hubble rate. For the figure, we have fixed $\Omega_\chi^0 h^2 = 0.1198$ and the remaining five ΛCDM parameters to their best fit values from [4] (see equation 3.23). We see that a smaller value of κ results in a longer period of non-standard evolution of the Hubble rate. Thus, we expect smaller values of κ to be much more constrained as compared to the larger values.

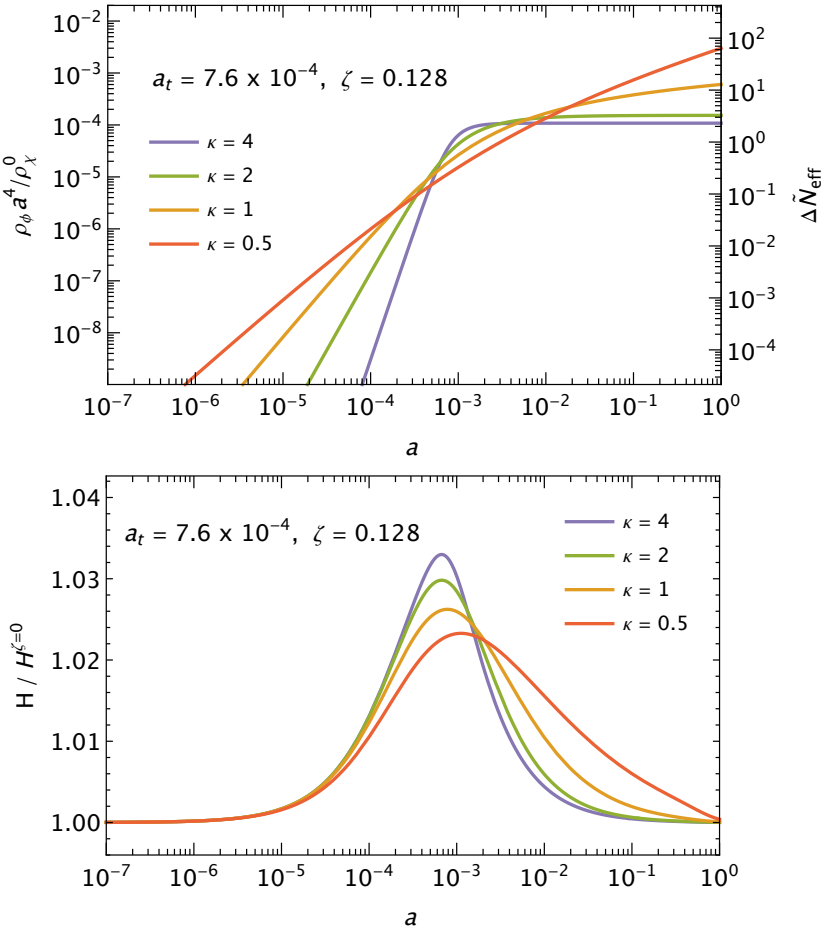

Figure 9.2: **Top:** Evolution of dark radiation energy density according to equation 9.4. **Bottom:** The resulting modification to the Hubble rate.

Perturbations

Let us now see how the density and velocity perturbation equations get modified in our scenario. The DM and DR energy momentum tensors are given by

$$T^{\chi}_{\mu\nu} = \rho_\chi u^\chi_\mu u^\chi_\nu \,, \tag{9.6}$$

$$T^{\phi}_{\mu\nu} = \frac{4}{3}\rho_\phi u^\phi_\mu u^\phi_\nu + \frac{\rho_\phi}{3} g_{\mu\nu} + \Pi^\phi_{\mu\nu} \,. \tag{9.7}$$

In our scenario, the combined energy momentum tensors of χ and ϕ are conserved, i.e. $\nabla^\nu \left(T^\chi_{\mu\nu} + T^\phi_{\mu\nu}\right) = 0$ and are related to $\mathcal{Q}$ as

$$\nabla^\nu T^\chi_{\mu\nu} = -\nabla^\nu T^\phi_{\mu\nu} \equiv -\mathcal{Q} u^\chi_\mu \,. \tag{9.8}$$

Using our derived results 3.18 and 3.19, we have at the lowest order

$$\rho'_\chi + 3\mathcal{H}\rho_\chi = -(\rho'_\phi + 4\mathcal{H}\rho_\phi) = -a\mathcal{Q}\,, \tag{9.9}$$

which is the same as the equation 9.3. At first order in perturbations, we then find

$$\delta'_\chi + \theta_\chi + \frac{1}{2}h' = \frac{a}{\rho_\chi}\left(\mathcal{Q}\delta_\chi - \delta\mathcal{Q}\right)\,, \tag{9.10}$$

$$\theta'_\chi + \mathcal{H}\theta_\chi = 0\,, \tag{9.11}$$

$$\delta'_\phi + \frac{4}{3}\theta_\phi + \frac{2}{3}h' = -\frac{a}{\rho_\phi}\left(\mathcal{Q}\delta_\phi - \delta\mathcal{Q}\right)\,, \tag{9.12}$$

$$\theta'_\phi + \frac{1}{4}\nabla^2\delta_\phi + \frac{1}{2\rho_\phi}\nabla^4\Pi^\phi = -\frac{3a}{4\rho_\phi}\mathcal{Q}\left(\frac{4}{3}\theta_\phi - \theta_\chi\right)\,, \tag{9.13}$$

where we have introduced the perturbation to the collision term as $\delta\mathcal{Q}$. The equation 9.11 admits the solution $\theta_\chi = 0$ and we can use the one residual degree of freedom to set $\theta_\chi = 0$ in the above equations. The synchronous gauge after this choice of gauge fixing is often referred as the *comoving synchronous gauge* in the literature and is widely used for numerical implementations of cosmological perturbations (see for example [227]). We can also write the above equations in Fourier space by replacing $\partial_i \to ik_i$ to get

$$\delta'_\chi + \frac{1}{2}h' = \frac{a}{\rho_\chi}\left(\mathcal{Q}\delta_\chi - \delta\mathcal{Q}\right)\,, \tag{9.14}$$

$$\delta'_\phi + \frac{4}{3}\theta_\phi + \frac{2}{3}h' = -\frac{a}{\rho_\phi}\left(\mathcal{Q}\delta_\phi - \delta\mathcal{Q}\right)\,, \tag{9.15}$$

$$\theta'_\phi - \frac{1}{4}k^2\delta_\phi + \frac{1}{2\rho_\phi}k^4\Pi^\phi = -\frac{a}{\rho_\phi}\mathcal{Q}\theta_\phi\,. \tag{9.16}$$

We see that unlike the background equations for ρ_χ and ρ_ϕ (expression 9.9), the perturbation equations are necessarily model dependent. For example, for the case of decays we have $\delta\mathcal{Q} = \delta(\Gamma_{\rm decay}\rho_\chi) = \mathcal{Q}\delta_\chi$, whereas for an annihilation we will have $\delta\mathcal{Q} = \delta\left(\frac{\langle\sigma v\rangle\rho_\chi^2}{m_\chi}\right) = \left(\frac{\delta\langle\sigma v\rangle}{\langle\sigma v\rangle} + 2\delta_\chi\right)\mathcal{Q}$.

In paper IV [24], our goal was to provide model independent constraints on DM depletion scenarios. For doing so we implemented a minimalistic prescription for describing $\delta\mathcal{Q}$. We assumed that the perturbations only affect the volume expansion and not the DM comoving density itself, which is equivalent to setting $\delta\mathcal{Q} = \mathcal{Q}\delta_\chi$ in equation 9.14. Note that our chosen prescription holds exactly for the case of DM decay. We will later discuss the impact of using the correct expression for $\delta\mathcal{Q}$ for the case of Sommerfeld enhanced annihilation in section 9.4.

9.3 Method and data

In paper IV [24], we constrained the above mentioned scenario using temperature and polarization data from Planck [228] (denoted as **CMB** in this chapter) and three post-CMB measurements (which we will collectively denote as **LSS**) —

- **Lensing**: Planck's lensing power spectrum reconstruction [71]
- **HST**: The direct measurement of the Hubble rate by the Hubble space telescope, i.e. $H_0 = 73.24 \pm 1.74\,\mathrm{km/sec/Mpc}$ [90]
- **PC**: Constraints on the matter power spectrum normalization from Planck cluster, i.e. $\sigma_8(\Omega_m/0.27)^{0.30} = 0.782 \pm 0.010$ [93].

We modified the publicly available Boltzmann code CAMB[2] [227, 229] to implement the different background and perturbation evolution of our model (equations 9.2, 9.4, 9.14–9.16). We assumed that the anisotropic stress generated by ϕ will evolve in the same way as that for an extra neutrino species.

In addition to the six ΛCDM parameters, for a fixed value of κ, we have two degrees of freedom in our model— a_t and ζ (or $\Delta N_{\rm eff}^{\rm today}$, see below). For scanning over the 8-dimensional parameter space, we used CosmoMC[3] [230, 231], a publicly available Fortran based Markov Chain Monte-Carlo sampler. We used a conservative (stopping) convergence criteria of $R - 1 < 0.01$, where R is the Gelman-Rubin criterion [232]. We used GetDist[4] [233] to analyze the chains and compute the Bayesian statistics. We provided the Bayesian exclusion limits on $\log_{10}\zeta$ as a function of $\log_{10} a_t$ for four different values of $\kappa = 0.5, 1, 2$ and 4. As

[2] https://camb.info/
[3] http://cosmologist.info/cosmomc/
[4] https://github.com/cmbant/getdist

the Bayesian limits are always dependent on the chosen priors, we complemented our Bayesian results with the frequentist estimates for the maximum allowed values of ζ as a function of a_t. For scanning, we used the following flat uniform priors for the ΛCDM parameters—

$$\begin{aligned} \Omega_b h^2 &\in (0.01,\, 0.10), & \Omega^0_\chi h^2 &\in (0.01,\, 0.50) \\ 100\theta_{\rm MC} &\in (0.8,\, 2.0), & \tau &\in (0.01,\, 0.20) \\ \ln(10^{10} A_s) &\in (2.0,\, 4.0), & n_s &\in (0.8,\, 1.2)\,. \end{aligned} \tag{9.17}$$

For our model parameters we used a more complex choice of priors. We wanted to probe transitions centered deep in the radiation dominated era ($a_t \geq 10^{-7}$) to very late times ($a_t \leq 0.1$). We thus adopted a flat prior on $\log_{10} a_t$ to scan over the parameter space. For each fixed value of κ and the considered dataset, we divided the parameter space into two scans. For large a_t, $10^{-4} \leq a_t \leq 10^{-1}$, we used ζ as our scanning parameter and for small a_t, $10^{-7} \leq a_t \leq 10^{-4}$, we scanned $\Delta\tilde{N}_{\rm eff}^{\rm today}$ (and ζ was a derived parameter in these scans). We used the following prior choices for our model parameters—

$$\begin{aligned} \text{for} \quad & \log_{10} a_t \in (-7,\, -4) & \Delta\tilde{N}_{\rm eff}^{\rm today} &\in (0.0,\, 1000.0) \\ \text{and for} \quad & \log_{10} a_t \in (-4,\, -1) & \zeta &\in (0.0,\, 1000.0)\,. \end{aligned} \tag{9.18}$$

We refer the reader to our paper IV [24] for a detailed discussion of our results. In this thesis, we will discuss some of the subtleties involved in the analysis and elaborate on our particular parameter and prior choice below.

9.4 Discussion

Choice of parameters

The latest CMB measurements from Planck [4] constrain the amount of constant comoving DR density at recombination to be $\Delta N_{\rm eff} \lesssim 0.4$ at 95% C.L. . Using the expressions 9.4 and 9.5, we can see that this corresponds to a large value ($\gtrsim \mathcal{O}(10)$) of ζ for very small a_t. On the other hand for transitions in matter dominated regime, i.e. larger a_t, we will expect the changes in the Hubble rate to be very constrained and thus expect $\zeta \ll 1$. We can thus see that a choice of using ζ as the scanned parameter is not a good one for all the points in our $\log_{10} a_t$ space, as it will lead to an extremely large range of scanned values and thus resulting in

long run times of the scans. A solution to this is to use $\log_{10}\zeta$ as the scanning parameter. With this choice, we will be scanning logarithm of the values, which will be of similar $\mathcal{O}(1)$ magnitude.

Alternatively, one can also scan $\Delta\tilde{N}_{\rm eff}^{\rm today}$ instead of ζ.[5] The equation 9.4 can be inverted to get ζ as a function of $\Delta\tilde{N}_{\rm eff}^{\rm today}$. The scanned values of $\Delta\tilde{N}_{\rm eff}^{\rm today}$ for small $a_t < a_{\rm rec}$ will now be of similar magnitude due to the $\Delta N_{\rm eff} \lesssim 0.4$ constraint at recombination. As ρ_ϕ is an increasing function of a_t, we will again have much larger allowed values of $\Delta\tilde{N}_{\rm eff}^{\rm today}$ for $a_t > a_{\rm rec}$. In order to optimize the scanning efficiency, it is thus favorable to divide our scan and use ζ to scan the parameter space for large a_t and $\Delta\tilde{N}_{\rm eff}^{\rm today}$ for small a_t. This choice will make the scanner scan values of similar magnitude, thus decreasing the computation time.

In Fig. 9.3, we show the 95% Bayesian C.L. on $\log_{10}\zeta$ as a function of $\log_{10} a_t$ using only the **CMB** dataset for the three different choice of scanning parameter we just described above. For the plot, we have set $\kappa = 2$ and fixed $\Omega_\chi^{\rm rec}h^2 = 0.1198$ and the other five ΛCDM parameters to their best-fit values [4]. Thus, it is a two-parameter scan and is meant just for the illustration of the difference in the limits from the use of different scanning parameters. The shaded green area indicates the allowed region using $\log_{10}\zeta$ as the fundamental scanning parameter. The blue area indicates the allowed region using ζ as the scanning parameter and restricting $10^{-3} \leq a_t \leq 10^{-1}$. Lastly, the orange region is for the scan with $10^{-7} \leq a_t \leq 10^{-3}$ and $\Delta\tilde{N}_{\rm eff}^{\rm today}$ as the scanning parameter.

We see that the limits are different by using logarithmic and linear parameters as fundamental scanning parameters. The limits using logarithmic scanning parameter are more stringent than the linear parameters. This is due to the fact that a uniform prior on $\log\zeta$ implies that we are using the prior probability $1/\zeta$ for the parameter ζ.[6] Thus, a scan with $\log_{10}\zeta$ generates a bias for smaller values of ζ and does not scan over the larger values well. Log priors are often useful when the order of magnitude of the parameter is unknown. In our model we know the maximum amount of DR allowed at recombination very precisely in the ΛCDM framework, i.e $\Delta N_{\rm eff} \lesssim 0.4$, and we thus need to use linear priors for an accurate comparison to the constant $\Delta N_{\rm eff}$ case. We refer the interested reader to [234] for

[5] We have fixed the reference point of the parameter to $a = 1$ to get a simple expression for ζ. One can fix the reference scale factor to any arbitrary value.

[6] The probability distribution function (pdf) of a function of a random variable can be calculated as the derivative of the cumulative distribution function of the random variable. For our case, we have $d\log x/dx = 1/x$.

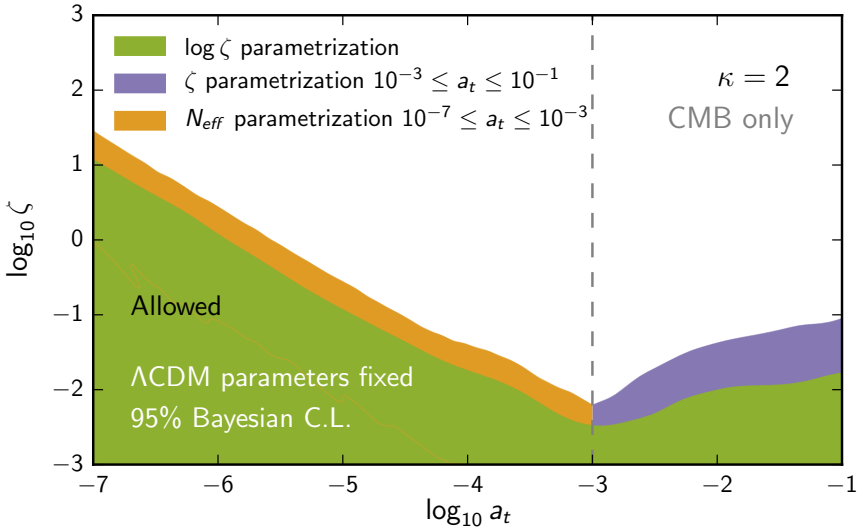

Figure 9.3: Comparison of Bayesian 95% C.L. on $\log_{10}\zeta$ for different choices of scanning parameters. For the plot we have fixed the ΛCDM parameters and varied our model parameters. The green, blue and orange areas correspond to scans with $\log_{10}\zeta$, ζ and $\tilde{N}_{\rm eff}^{\rm today}$ as scanning parameters, respectively. We see that a logarithmic scanning parameters will not efficiently scan the tails of the distribution.

a similar discussion on the use of log vs. linear priors for constraining neutrino masses.

Note that these illustrative limits are derived by fixing the ΛCDM parameters. By allowing the six ΛCDM parameters to vary, the shown limits will become less stringent due to the extra degrees of freedom available to fit the data. In the rest of this chapter, we will also vary the ΛCDM parameters (as was done in paper IV [24]).

Low-redshift observables

We will now discuss the constraints on the two low-redshift cosmological observables σ_8 and H_0 in our model framework. In Fig. 9.4, we show in the left panels the 1D-marginalized posteriors of σ_8 and in the right panels the 2D-marginalized posteriors of the parameters $\sigma_8(\Omega_m/0.27)^{0.3}$ & H_0 in our model with $\kappa = 1$ and two fixed values of $a_t = 10^{-7}, 10^{-2.5}$ shown as red and green, respectively. The top panels are results from using only the **CMB** dataset and the bottom panels

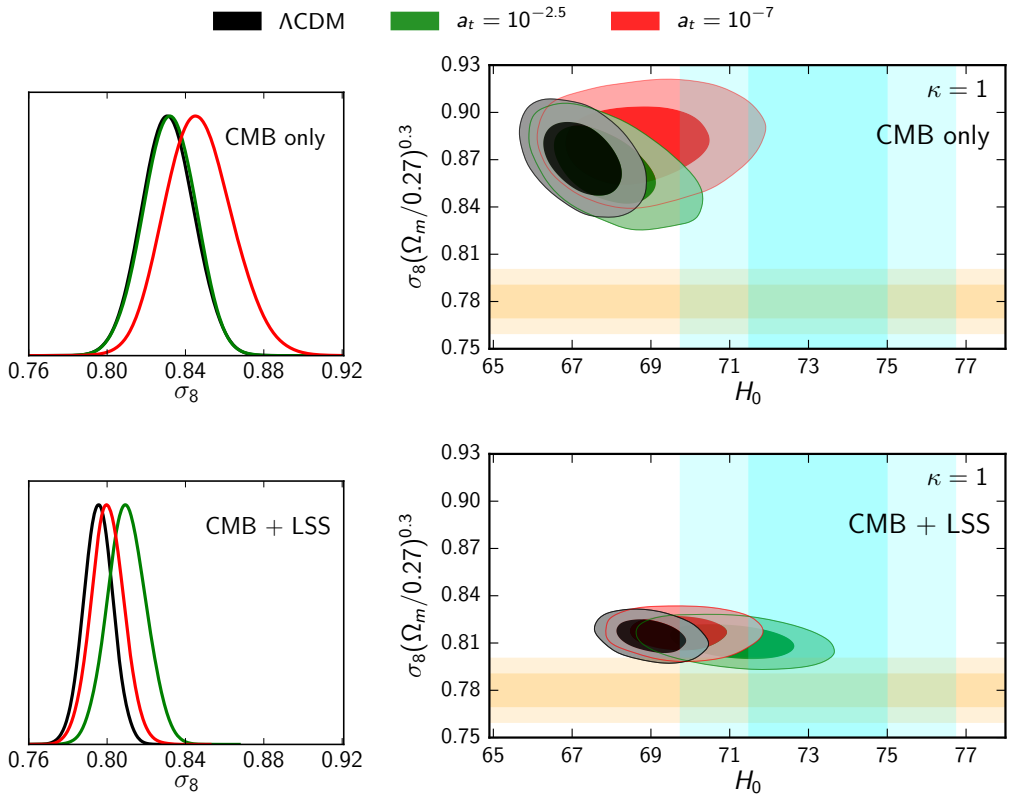

Figure 9.4: Bayesian constraints on σ_8, $\sigma_8(\Omega_m/0.27)^{0.3}$ and H_0 for our $\kappa = 1$ model using **CMB** only (top panels) and **CMB + LSS** (bottom panels) datasets. **Left panels:** 1D-marginalized posterior of σ_8 normalized to the maximum posterior probability. **Right panels:** 1σ and 2σ contours of the 2D-marginalized posterior in $\sigma_8(\Omega_m/0.27)^{0.3}$ vs. H_0 plane. For comparison, we have also shown the results in the ΛCDM model, shown as black lines/contours. The cyan and orange bands in the right panels indicate the measurements from **HST** and **PC**, respectively.

are with **CMB + LSS**. For comparison, we have also shown the constraints in the ΛCDM framework as black lines or contours. In the figure, we have also indicated the direct measurements of **HST** and **PC** as cyan and orange bands, respectively.

In the left panels of the figure, we see that our model prefers larger values of σ_8 than in the ΛCDM model. Even in the ΛCDM + constant $N_{\rm eff}$ scan of Ref. [4], the preferred value of σ_8 is larger than the vanilla ΛCDM model. This is contrary to what one will naively expect, as the Matter Power Spectrum (MPS) should be suppressed at sub-Mpc scales due to the free streaming of DR.

To understand this conundrum, we should note that the CMB spectrum and MPS are also dependent on the ΛCDM parameters, which are free parameters in our scans shown in the figure and are highly correlated with each other. Fitting our model (or the constant $N_{\rm eff}$ extension of ΛCDM) to the data changes the preferred values of the ΛCDM parameters such that we get a larger amplitude of the MPS resulting in larger σ_8. An analysis to single out the parameters responsible for increasing σ_8 is hard due to the large parameter space and high degree of correlation among the parameters and is thus beyond the scope of this thesis. We should however note that we did not find any region of parameter space (for all considered κ) where the preferred value of σ_8 is smaller than the best-fit vanilla ΛCDM value.[7]

As we discussed in subsection 3.3.2, the tension between CMB and the low redshift experiments is actually in the σ_8 vs. Ω_m plane (and not directly in σ_8). The different experiments probing low-redshift regimes [91–93] actually measure the combination $\sigma_8\Omega_m^\alpha$ (with $1 > \alpha > 0$ and α varies for different experiments). CMB experiments predict a larger value of $\sigma_8\Omega_m^\alpha$ than the ones probing low redshifts. In our model, even though the preferred value of σ_8 is larger, for the case of late transitions we can have a significantly smaller value of Ω_m than the ΛCDM. We can thus decrease the quantity $\sigma_8\Omega_m^\alpha$ in our model and reduce the tension between CMB and low redshift experiments.

In the right panel of Fig. 9.4, we see that the preferred value of $\sigma_8(\Omega_m/0.27)^{0.3}$ does indeed decrease for the green curves as compared to the ΛCDM due to the decrease in Ω_m. For the case of small a_t, Ω_m cannot decrease much as the amount of matter at recombination is strongly constrained by the CMB and we thus see an increase in $\sigma_8(\Omega_m/0.27)^{0.3}$ due to the larger value of σ_8 (shown in left panel).

We also see that the Hubble rate today does generically increase in our model as compared to ΛCDM, for both small and large a_t. This behavior of our model can be qualitatively understood. For the case of large a_t, this is due to the fact that CMB strongly constrains the amount of DM, i.e. $\rho_\chi \propto \Omega_\chi h^2$. A decrease in the the DM density parameter after recombination implies that we need to increase the late time Hubble rate to have the same amount of DM at recombination. The case of small a_t is similar to the constant $N_{\rm eff}$ extension, in which the extra DR

[7] We should note that we did not consider DM-DR scatterings in our model. Such interactions can significantly lower the value of σ_8 and can in principle change our conclusions (see for example [235]).

prior to recombination increases the size of the sound horizon at the surface of last scattering. In order to achieve the same angular size of sound horizon, which is measured very accurately by the CMB, a larger value of late time Hubble rate is required to increase the distance to the last scattering surface.

Thus, our model with late DM depletions can help alleviate the discrepancies between low-redshift data and the CMB. In the bottom panels, with combined **CMB** and **LSS** datasets, we see that the corresponding contours have moved down and towards right, i.e. towards the direct measurements. The displacement of the large a_t contour is the largest as it can help reconcile **CMB**, **HST** and **PC** measurements. In our results with **CMB + LSS**, we saw a preference for large a_t over small a_t, which we will next discuss.

Choice of a_t for dividing the parameter space

In Fig. 9.5, we show the results for our scans with the prior choices $10^{-7} \leq a_t \leq 10^{-3}$ (left panels) and $10^{-7} \leq a_t \leq 10^{-4}$ (right panels). In the top panels we have used **CMB** only data and in the bottom panels we have used **CMB + LSS**. The solid white lines in each of the panels represents the 95% Bayesian C.L. on $\Delta\tilde{N}_{\rm eff}^{\rm today}$. We see that the the limits in the top panels are almost independent of the prior choice, whereas the limits in the bottom panels are strongly dependent on the prior choice.

To understand the limits in the figure, let us first see how the limits in the Bayesian framework are usually calculated. For example, for constructing the limits on two parameters x & y, one first *marginalizes* (integrates) over all other model parameters to calculate the marginalized posterior $p(x, y)$ in x vs. y plane. Then one draws contours of equal posterior probability around the point of maximum posterior probability $(x_{\rm best}, y_{\rm best})$ and integrates over the posterior probability in the enclosed area. The 95% (99%) contours are calculated such that the value of the integral inside the contour equals 0.95 (0.99). In all the four panels of the figure we show these contours of equal posterior probabilities, with the scaling shown in the color-map on the right.

In the top panels, the position of the maximum posterior in $10^{-7} \leq a_t \leq 10^{-3}$ case is also contained in the other case $10^{-7} \leq a_t \leq 10^{-4}$.[8] Thus the limits are

[8] It is interesting to note that Ref. [19] also found a *bump* in their constraints on the fraction of unstable DM decaying before recombination, which we see around $a_t \sim 10^{-4}$ in our model using

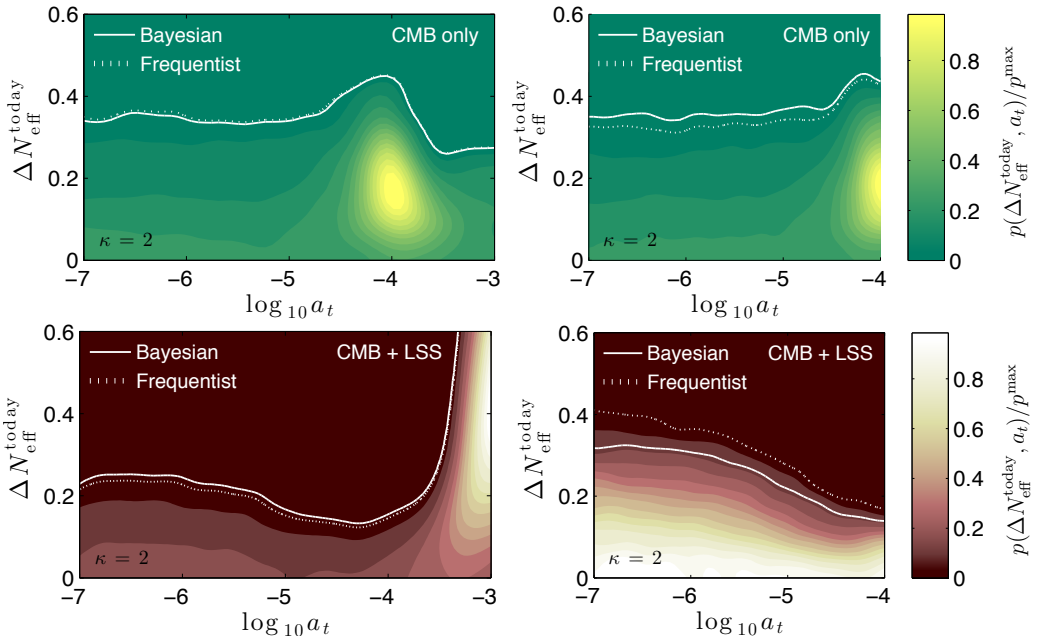

Figure 9.5: Comparison of Bayesian and Frequentist estimates of 95% limits on our $\kappa = 2$ model using **CMB** only (top panels) and **CMB + LSS** (bottom panels) datasets for two different choice of priors for $\log_{10} a_t$. The different contours of equal posterior probability are also shown in the panels, with the color scheme indicated on the right. See text for further details.

quite similar in the top panels, with a very small decrease (hardly visible at the resolution of the figures) in the left panel due to the larger area contained in the enclosing contours. Whereas, in the bottom panels due to the higher preference for large a_t in our model with **LSS** data position of the maximum posterior in the left panel is at $a_t \sim 10^{-3}$, which is not contained in the right panel. The limits in the bottom-left panel are thus more stringent as most of the contribution to the integral for limit calculation comes from the $a_t \sim 10^{-3}$ region.

Bayesian limits are always dependent on the prior choice. Since the ΛCDM parameters are tightly constrained, a choice of a wide prior is a good one and does not affect the resulting limits in the ΛCDM model in a significant way. This is not the case with our model parameter a_t. For exploring the small a_t region well, we thus divided our scans into two parts at $a_t = 10^{-4}$ to avoid the large preference

CMB data only. Note that our $\kappa = 2$ model gives a close agreement with the decaying DM model (see Fig. 9.1).

for large a_t using **LSS** data. For consistency, we also used the same division when we used only the **CMB** dataset.

To avoid the dependence of limits on the prior choice, we also presented the frequentist estimate of the limits in the paper. We calculated the limits by considering the test statistic

$$t = -2\,\Delta \log \mathcal{L} \approx -2 \log \left[\frac{p(\Delta N_{\rm eff}^{\rm today}, a_t)}{p^{\rm max}} \right] \,, \tag{9.19}$$

where we have denoted $p^{\rm max}$ as the point of maximum marginalized posterior in the plane. We assumed that t follows a χ^2 distribution with two degrees of freedom, and thus the 95% limits are given by $t = 5.99$, which corresponds to $p(\Delta N_{\rm eff}^{\rm today}, a_t) \simeq 0.05\, p^{\rm max}$. We show the frequentist estimate of 95% limits by the dotted white lines in the figure.

The frequentist and Bayesian limits are quite similar except the bottom right panel. The Bayesian limits in the bottom right panel are more stringent due to the fact that the contours for the equal posterior values are quite wide as compared to the other cases, thus the integral over the posterior values gains a larger amount for smaller values of $\Delta \tilde{N}_{\rm eff}$.

Concluding remarks

In paper IV [24], to the best of our knowledge, we presented for the first time model independent cosmological constraints on DM depletion scenarios. The constraints cannot only be applied to the often studied particle physics scenarios like DM decay (equivalent to our $\kappa \sim 2$ model) and Sommerfeld annihilation (equivalent to our $\kappa \sim 1$ model) but also to more general scenarios, for example, emission of gravitation waves from primordial black hole mergers [236, 237].

We explicitly examined the model dependence that enters at the perturbation level due to $\delta\mathcal{Q}$ for the on-resonance Sommerfeld annihilation scenario. For the case of on-resonance Sommerfeld annihilation before saturation, we have $\langle \sigma v \rangle \propto v^{-2}$. Following the prescription in Ref. [238], we should have used $\delta\mathcal{Q} = \mathcal{Q}(2\delta_\chi + h/3)$ instead of our minimalistic prescription $\delta\mathcal{Q} = \mathcal{Q}\delta_\chi$. Noting that the perturbation $\delta\mathcal{Q}$ is proportional to $\mathcal{Q}$, we found that a different treatment of $\delta\mathcal{Q}$ results in a negligible difference on the limits as the quantity $\mathcal{Q}$ is very strongly constrained by the data.

Finally, we comment on the alleviation of the small-scale problems in the context of our results presented in this chapter. In the previous chapter, we found that for a scenario where DM interacts with a MeV-mass mediator via a Yukawa interaction, can help alleviate the small scale problems of ΛCDM. Such a model also results in an enhanced annihilation rate due to Sommerfeld enhancement. As we showed in this chapter, an on-resonance Sommerfeld annihilation of DM can also help reduce the discrepancy between CMB and low-redshift observations (see Fig. 9.4). Thus, we can have a DM model which can simultaneously solve the small-scale problems and also reduce the discrepancy between CMB and low-redshift measurements. Such a solution has been qualitatively discussed before [177, 181, 184, 185, 192, 239, 240]. In paper IV [24], we for the first time did a detailed analysis with the use of Boltzmann code to confirm these claims.

Chapter 10

Summary

In this thesis, we covered a wide range of topics in DM physics. In paper I [21], we estimated the leading QCD corrections for neutralino annihilation to quark final states. The initial Majorana pair's $J = 0$ state effectively behaves as a pseudoscalar under Lorentz transformations. We used this property to approximate the annihilation process as a pseudoscalar decay. The presented calculation is computationally faster and can be generalized to any scenario with a Majorana DM candidate (see [132]). The $\mathcal{O}(\alpha_s)$ QCD corrections (equation 7.3) are very important for DM masses near the top-quark threshold and should be taken into account for such small DM masses. The $\mathcal{O}(\alpha_s)$ calculation breaks down for $m_\chi \gg m_q$ and our resummed result (equation 7.6) provides a better treatment of the QCD corrections. We found that the gluon VIB contribution to DM annihilation is a subdominant contribution from the perspective of the relic density calculation but it can have significant effects on indirect detection prospects for degenerate squark scenarios. The work done is now a part of the public DarkSUSY code [163].

The rest of the thesis focused more on the discrepancies between observations and ΛCDM predictions. In paper II [22], we classified models with minimal particle content that can allow for late kinetic decoupling of DM (see equation 6.9), thus aiding to alleviate the missing satellites problem. We also computed ETHOS parameters for relating specific particle physics models to the $N-$body simulations. We found that models with DM scattering with DR through a $t-$channel exchange of a MeV scale mediator cannot only produce a large cutoff in the matter power spectrum but also help alleviate the other two small scale problems, cusp vs. core and TBTF due to efficient self interactions.

DM interacting with a MeV scale mediator via a Yukawa coupling can natu-

rally result in large self-scattering cross sections and thus solve the cusp vs. core and TBTF problems. In this most common setting, SIDM annihilation process also gets a large enhancement at small DM velocities through Sommerfeld enhancement. The annihilation products are the mediator particles which subsequently decay to lighter states to avoid over-closing of the universe. In paper III [23], we showed that the desirable parameter space of SIDM models for addressing the cusp vs. core and TBTF problems is strongly constrained if the mediator particles decay to SM final states. We used CMB and indirect detection experiment data to constrain SIDM annihilation. The injection of highly energetic SM particles into the plasma alters recombination or reionization history and thus have a significant effect on CMB. The indirect detection experiments also independently exclude most of the parameter space for quantum resonant self scattering.

In paper IV [24], we used a very general parametrization for describing a scenario in which the comoving number density of DM decreases with time. Due to strong constraints on SM final states (paper III [23]), we assumed that the *depleted* DM gets converted to some form of non-interacting DR. Decaying DM and on-resonance Sommerfeld enhanced annihilation are two of the many possible realizations for such a kind of conversion process. We used CMB [4] and other low-redshift measurements [71, 90, 93] to constrain the scenario. We found that conversions during the matter-radiation equality are strongly constrained. Conversions at times later than recombination can help mitigate the discrepancies between CMB data and direct measurements of σ_8 and H_0. Lastly, for the first time it was shown using a Boltzmann code that models with a Yukawa interaction can simultaneously solve the small scale problems and also the σ_8 and H_0 discrepancies.

The searches for standard DM have only returned null results. This reiterates the need to look for alternative observables. The work done in this thesis is a step in this direction.

Bibliography

[1] **2DFGRS** Collaboration, M. Colless *et al.*, "The 2dF Galaxy Redshift Survey: Spectra and redshifts," *Mon. Not. Roy. Astron. Soc.* **328** (2001) 1039, arXiv:astro-ph/0106498 [astro-ph].

[2] **SDSS** Collaboration, M. Tegmark *et al.*, "The 3-D power spectrum of galaxies from the SDSS," *Astrophys. J.* **606** (2004) 702–740, arXiv:astro-ph/0310725 [astro-ph].

[3] **WMAP** Collaboration, G. Hinshaw *et al.*, "Nine-Year Wilkinson Microwave Anisotropy Probe (WMAP) Observations: Cosmological Parameter Results," *Astrophys. J. Suppl.* **208** (2013) 19, arXiv:1212.5226 [astro-ph.CO].

[4] **Planck** Collaboration, P. A. R. Ade *et al.*, "Planck 2015 results. XIII. Cosmological parameters," *Astron. Astrophys.* **594** (2016) A13, arXiv:1502.01589 [astro-ph.CO].

[5] D. Clowe, A. Gonzalez, and M. Markevitch, "Weak lensing mass reconstruction of the interacting cluster 1E0657-558: Direct evidence for the existence of dark matter," *Astrophys. J.* **604** (2004) 596–603, arXiv:astro-ph/0312273 [astro-ph].

[6] D. Clowe, M. Bradac, A. H. Gonzalez, M. Markevitch, S. W. Randall, C. Jones, and D. Zaritsky, "A direct empirical proof of the existence of dark matter," *Astrophys. J.* **648** (2006) L109–L113, arXiv:astro-ph/0608407 [astro-ph].

[7] S. D. M. White, C. S. Frenk, and M. Davis, "Clustering in a Neutrino Dominated Universe," *Astrophys. J.* **274** (1983) L1–L5. [,80(1984)].

[8] M. Davis, G. Efstathiou, C. S. Frenk, and S. D. M. White, "The Evolution of Large Scale Structure in a Universe Dominated by Cold Dark Matter," *Astrophys. J.* **292** (1985) 371–394. [,105(1985)].

[9] G. R. Blumenthal, S. M. Faber, J. R. Primack, and M. J. Rees, "Formation of galaxies and large-scale structure with cold dark matter.," *Nature* **311** (Oct., 1984) 517–525.

[10] G. Bertone, D. Hooper, and J. Silk, "Particle dark matter: Evidence, candidates and constraints," *Phys. Rept.* **405** (2005) 279–390, arXiv:hep-ph/0404175 [hep-ph].

[11] B. Herrmann, M. Klasen, and K. Kovarik, "SUSY-QCD effects on neutralino dark matter annihilation beyond scalar or gaugino mass unification," *Phys. Rev.* **D80** (2009) 085025, arXiv:0907.0030 [hep-ph].

[12] N. Baro, F. Boudjema, G. Chalons, and S. Hao, "Relic density at one-loop with gauge boson pair production," *Phys. Rev.* **D81** (2010) 015005, arXiv:0910.3293 [hep-ph].

[13] G. Efstathiou, W. J. Sutherland, and S. J. Maddox, "The cosmological constant and cold dark matter," *Nature* **348** (1990) 705–707.

[14] J. S. Bullock and M. Boylan-Kolchin, "Small-Scale Challenges to the ΛCDM Paradigm," *Ann. Rev. Astron. Astrophys.* **55** (2017) 343–387, arXiv:1707.04256 [astro-ph.CO].

[15] D. N. Spergel and P. J. Steinhardt, "Observational evidence for selfinteracting cold dark matter," *Phys. Rev. Lett.* **84** (2000) 3760–3763, arXiv:astro-ph/9909386 [astro-ph].

[16] K. Enqvist, S. Nadathur, T. Sekiguchi, and T. Takahashi, "Decaying dark matter and the tension in σ_8," *JCAP* **1509** no. 09, (2015) 067, arXiv:1505.05511 [astro-ph.CO].

[17] Z. Berezhiani, A. D. Dolgov, and I. I. Tkachev, "Reconciling Planck results with low redshift astronomical measurements," *Phys. Rev.* **D92** no. 6, (2015) 061303, arXiv:1505.03644 [astro-ph.CO].

[18] A. Chudaykin, D. Gorbunov, and I. Tkachev, "Dark matter component decaying after recombination: Lensing constraints with Planck data," *Phys. Rev.* **D94** (2016) 023528, arXiv:1602.08121 [astro-ph.CO].

[19] V. Poulin, P. D. Serpico, and J. Lesgourgues, "A fresh look at linear cosmological constraints on a decaying dark matter component," *JCAP* **1608** no. 08, (2016) 036, arXiv:1606.02073 [astro-ph.CO].

[20] L. G. van den Aarssen, T. Bringmann, and Y. C. Goedecke, "Thermal decoupling and the smallest subhalo mass in dark matter models with Sommerfeld-enhanced annihilation rates," *Phys. Rev.* **D85** (2012) 123512, arXiv:1202.5456 [hep-ph].

[21] T. Bringmann, A. J. Galea, and P. Walia, "Leading QCD Corrections for Indirect Dark Matter Searches: a Fresh Look," *Phys. Rev.* **D93** no. 4, (2016) 043529, arXiv:1510.02473 [hep-ph].

[22] T. Bringmann, H. T. Ihle, J. Kersten, and P. Walia, "Suppressing structure formation at dwarf galaxy scales and below: late kinetic decoupling as a compelling alternative to warm dark matter," *Phys. Rev.* **D94** no. 10, (2016) 103529, arXiv:1603.04884 [hep-ph].

[23] T. Bringmann, F. Kahlhoefer, K. Schmidt-Hoberg, and P. Walia, "Strong constraints on self-interacting dark matter with light mediators," *Phys. Rev. Lett.* **118** no. 14, (2017) 141802, arXiv:1612.00845 [hep-ph].

[24] T. Bringmann, F. Kahlhoefer, K. Schmidt-Hoberg, and P. Walia, "Converting non-relativistic dark matter to radiation," *Phys. Rev.* **D98** (2018) 023543, arXiv:1803.03644 [astro-ph.CO].

[25] J. H. Jeans, "The Motions of Stars in a Kapteyn Universe," *Mon. Not. Roy. Astron. Soc.* **82** (Jan., 1922) 122–132.

[26] J. H. Oort, "The force exerted by the stellar system in the direction perpendicular to the galactic plane and some related problems," *Bulletin of the Astronomical Institutes of the Netherlands* **6** (Aug., 1932) 249.

[27] F. Zwicky, "Die Rotverschiebung von extragalaktischen Nebeln," *Helv. Phys. Acta* **6** (1933) 110–127. [Gen. Rel. Grav.41,207(2009)].

[28] V. C. Rubin, W. K. Ford, Jr., and N. Thonnard, "Extended rotation curves of high-luminosity spiral galaxies. IV. Systematic dynamical properties, Sa through Sc," *Astrophys. J.* **225** (1978) L107–L111.

[29] V. C. Rubin, N. Thonnard, and W. K. Ford, Jr., "Rotational properties of 21 SC galaxies with a large range of luminosities and radii, from NGC 4605 /R = 4kpc/ to UGC 2885 /R = 122 kpc/," *Astrophys. J.* **238** (1980) 471.

[30] D. Lyth and A. Liddle, *The Primordial Density Perturbation: Cosmology, Inflation and the Origin of Structure*. Cambridge University Press, 2009. https://books.google.no/books?id=Mor_ehlYc4QC.

[31] J. Lesgourgues and S. Pastor, "Massive neutrinos and cosmology," *Phys. Rept.* **429** (2006) 307–379, arXiv:astro-ph/0603494 [astro-ph].

[32] D. J. Eisenstein, H.-j. Seo, E. Sirko, and D. Spergel, "Improving Cosmological Distance Measurements by Reconstruction of the Baryon Acoustic Peak," *Astrophys. J.* **664** (2007) 675–679, arXiv:astro-ph/0604362 [astro-ph].

[33] C. Blake *et al.*, "The WiggleZ Dark Energy Survey: mapping the distance-redshift relation with baryon acoustic oscillations," *Mon. Not. Roy. Astron. Soc.* **418** (2011) 1707–1724, arXiv:1108.2635 [astro-ph.CO].

[34] N. Padmanabhan, X. Xu, D. J. Eisenstein, R. Scalzo, A. J. Cuesta, K. T. Mehta, and E. Kazin, "A 2 per cent distance to z=0.35 by reconstructing baryon acoustic oscillations - I. Methods and application to the Sloan Digital Sky Survey," *Mon. Not. Roy. Astron. Soc.* **427** no. 3, (2012) 2132–2145, arXiv:1202.0090 [astro-ph.CO].

[35] N. G. Busca *et al.*, "Baryon Acoustic Oscillations in the Ly-α forest of BOSS quasars," *Astron. Astrophys.* **552** (2013) A96, arXiv:1211.2616 [astro-ph.CO].

[36] A. Slosar *et al.*, "Measurement of Baryon Acoustic Oscillations in the Lyman-alpha Forest Fluctuations in BOSS Data Release 9," *JCAP* **1304** (2013) 026, arXiv:1301.3459 [astro-ph.CO].

[37] J. F. Navarro, C. S. Frenk, and S. D. M. White, "The Structure of cold dark matter halos," *Astrophys. J.* **462** (1996) 563–575, arXiv:astro-ph/9508025 [astro-ph].

[38] V. Springel, S. D. M. White, A. Jenkins, C. S. Frenk, N. Yoshida, L. Gao, J. Navarro, R. Thacker, D. Croton, J. Helly, J. A. Peacock, S. Cole, P. Thomas, H. Couchman, A. Evrard, J. Colberg, and F. Pearce, "Simulations of the formation, evolution and clustering of galaxies and quasars," *Nature* **435** (June, 2005) 629–636.

[39] V. Springel *et al.*, "Simulating the joint evolution of quasars, galaxies and their large-scale distribution," *Nature* **435** (2005) 629–636, arXiv:astro-ph/0504097 [astro-ph].

[40] V. Springel, J. Wang, M. Vogelsberger, A. Ludlow, A. Jenkins, A. Helmi, J. F. Navarro, C. S. Frenk, and S. D. M. White, "The Aquarius Project: the subhalos of galactic halos," *Mon. Not. Roy. Astron. Soc.* **391** (2008) 1685–1711, arXiv:0809.0898 [astro-ph].

[41] J. M. Cline, Z. Liu, and W. Xue, "Millicharged Atomic Dark Matter," *Phys. Rev.* **D85** (2012) 101302, arXiv:1201.4858 [hep-ph].

[42] A. Coc and E. Vangioni, "Primordial nucleosynthesis," *Int. J. Mod. Phys.* **E26** no. 08, (2017) 1741002, arXiv:1707.01004 [astro-ph.CO].

[43] I. M. Oldengott, D. Boriero, and D. J. Schwarz, "Reionization and dark matter decay," *JCAP* **1608** no. 08, (2016) 054, arXiv:1605.03928 [astro-ph.CO].

[44] J. Sommer-Larsen and A. Dolgov, "Formation of disk galaxies: warm dark matter and the angular momentum problem," *Astrophys. J.* **551** (2001) 608–623, arXiv:astro-ph/9912166 [astro-ph].

[45] A. Boyarsky, J. Lesgourgues, O. Ruchayskiy, and M. Viel, "Lyman-alpha constraints on warm and on warm-plus-cold dark matter models," *JCAP* **0905** (2009) 012, arXiv:0812.0010 [astro-ph].

[46] M. Taoso, G. Bertone, and A. Masiero, "Dark Matter Candidates: A Ten-Point Test," *JCAP* **0803** (2008) 022, arXiv:0711.4996 [astro-ph].

[47] G. Jungman, M. Kamionkowski, and K. Griest, "Supersymmetric dark matter," *Phys. Rept.* **267** (1996) 195–373, arXiv:hep-ph/9506380 [hep-ph].

[48] S. Dodelson and L. M. Widrow, "Sterile-neutrinos as dark matter," *Phys. Rev. Lett.* **72** (1994) 17–20, arXiv:hep-ph/9303287 [hep-ph].

[49] S. Tulin and H.-B. Yu, "Dark Matter Self-interactions and Small Scale Structure," *Phys. Rept.* **730** (2018) 1–57, arXiv:1705.02358 [hep-ph].

[50] L. Roszkowski, E. M. Sessolo, and S. Trojanowski, "WIMP dark matter candidates and searches—current status and future prospects," *Rept. Prog. Phys.* **81** no. 6, (2018) 066201, arXiv:1707.06277 [hep-ph].

[51] M. W. Goodman and E. Witten, "Detectability of Certain Dark Matter Candidates," *Phys. Rev.* **D31** (1985) 3059. [,325(1984)].

[52] L. Bergström, "Nonbaryonic dark matter: Observational evidence and detection methods," *Rept. Prog. Phys.* **63** (2000) 793, arXiv:hep-ph/0002126 [hep-ph].

[53] T. Marrodán Undagoitia and L. Rauch, "Dark matter direct-detection experiments," *J. Phys.* **G43** no. 1, (2016) 013001, arXiv:1509.08767 [physics.ins-det].

[54] **CoGeNT** Collaboration, C. E. Aalseth *et al.*, "Results from a Search for Light-Mass Dark Matter with a P-type Point Contact Germanium Detector," *Phys. Rev. Lett.* **106** (2011) 131301, arXiv:1002.4703 [astro-ph.CO].

[55] G. Angloher *et al.*, "Results from 730 kg days of the CRESST-II Dark Matter Search," *Eur. Phys. J.* **C72** (2012) 1971, arXiv:1109.0702 [astro-ph.CO].

[56] **DAMA** Collaboration, R. Bernabei *et al.*, "First results from DAMA/LIBRA and the combined results with DAMA/NaI," *Eur. Phys. J.* **C56** (2008) 333–355, arXiv:0804.2741 [astro-ph].

[57] **CDMS** Collaboration, R. Agnese *et al.*, "Silicon Detector Dark Matter Results from the Final Exposure of CDMS II," *Phys. Rev. Lett.* **111** no. 25, (2013) 251301, arXiv:1304.4279 [hep-ex].

[58] J. M. Gaskins, "A review of indirect searches for particle dark matter," *Contemp. Phys.* **57** no. 4, (2016) 496–525, arXiv:1604.00014 [astro-ph.HE].

[59] **ATLAS** Collaboration, G. Aad *et al.*, "The ATLAS Experiment at the CERN Large Hadron Collider," *JINST* **3** (2008) S08003.

[60] **CMS** Collaboration, G. L. Bayatian *et al.*, "CMS technical design report, volume II: Physics performance," *J. Phys.* **G34** no. 6, (2007) 995–1579.

[61] F. Kahlhoefer, "Review of LHC Dark Matter Searches," *Int. J. Mod. Phys.* **A32** no. 13, (2017) 1730006, arXiv:1702.02430 [hep-ph].

[62] A. Friedmann, "Über die Krümmung des Raumes," *Zeitschrift für Physik* **10** (1922) .

[63] A. G. Lemaıtre, "A homogeneous universe of constant mass and increasing radius accounting for the radial velocity of extra-galactic nebulæ," *Monthly Notices of the Royal Astronomical Society* **91** no. 5, (1931) 483–490, http://dx.doi.org/10.1093/mnras/91.5.483.

[64] H. P. Robertson, "Kinematics and World-Structure. 3," *Astrophys. J.* **83** (1936) 257–271.

[65] E. W. Kolb and M. S. Turner, "The Early Universe," *Front. Phys.* **69** (1990) 1–547.

[66] **COBE** Collaboration, G. F. Smoot *et al.*, "Structure in the COBE differential microwave radiometer first year maps," *Astrophys. J.* **396** (1992) L1–L5.

[67] J. D. Barrow and R. Maartens, "Anisotropic stresses in inhomogeneous universes," *Phys. Rev.* **D59** (1999) 043502, arXiv:astro-ph/9808268 [astro-ph].

[68] C.-P. Ma and E. Bertschinger, "Cosmological perturbation theory in the synchronous and conformal Newtonian gauges," *Astrophys. J.* **455** (1995) 7–25, arXiv:astro-ph/9506072 [astro-ph].

[69] J. Hamann, "Evidence for extra radiation? Profile likelihood versus Bayesian posterior," *JCAP* **1203** (2012) 021, arXiv:1110.4271 [astro-ph.CO].

[70] **Planck** Collaboration, P. A. R. Ade *et al.*, "Planck 2013 results. XVI. Cosmological parameters," *Astron. Astrophys.* **571** (2014) A16, arXiv:1303.5076 [astro-ph.CO].

[71] **Planck** Collaboration, P. A. R. Ade *et al.*, "Planck 2015 results. XV. Gravitational lensing," *Astron. Astrophys.* **594** (2016) A15, arXiv:1502.01591 [astro-ph.CO].

[72] P. Bull *et al.*, "Beyond ΛCDM: Problems, solutions, and the road ahead," *Phys. Dark Univ.* **12** (2016) 56–99, arXiv:1512.05356 [astro-ph.CO].

[73] V. Springel, "The Cosmological simulation code GADGET-2," *Mon. Not. Roy. Astron. Soc.* **364** (2005) 1105–1134, arXiv:astro-ph/0505010 [astro-ph].

[74] M. Vogelsberger, S. Genel, V. Springel, P. Torrey, D. Sijacki, D. Xu, G. F. Snyder, S. Bird, D. Nelson, and L. Hernquist, "Properties of galaxies reproduced by a hydrodynamic simulation," *Nature* **509** (2014) 177–182, arXiv:1405.1418 [astro-ph.CO].

[75] G. Kauffmann, S. D. M. White, and B. Guiderdoni, "The Formation and Evolution of Galaxies Within Merging Dark Matter Haloes," *Mon. Not. Roy. Astron. Soc.* **264** (1993) 201.

[76] G. Kauffmann and S. D. M. White, "The merging history of dark matter haloes in a hierarchical universe," *Monthly Notices of the Royal Astronomical Society* **261** no. 4, (1993) 921–928. http://dx.doi.org/10.1093/mnras/261.4.921.

[77] A. A. Klypin, A. V. Kravtsov, O. Valenzuela, and F. Prada, "Where are the missing Galactic satellites?," *Astrophys. J.* **522** (1999) 82–92, arXiv:astro-ph/9901240 [astro-ph].

[78] B. Moore, S. Ghigna, F. Governato, G. Lake, T. R. Quinn, J. Stadel, and P. Tozzi, "Dark matter substructure within galactic halos," *Astrophys. J.* **524** (1999) L19–L22, arXiv:astro-ph/9907411 [astro-ph].

[79] J. Diemand, M. Kuhlen, P. Madau, M. Zemp, B. Moore, D. Potter, and J. Stadel, "Clumps and streams in the local dark matter distribution,"

Nature **454** (08, 2008) 735 EP –. http://dx.doi.org/10.1038/nature07153.

[80] **DES** Collaboration, A. Drlica-Wagner *et al.*, "Eight Ultra-faint Galaxy Candidates Discovered in Year Two of the Dark Energy Survey," *Astrophys. J.* **813** no. 2, (2015) 109, arXiv:1508.03622 [astro-ph.GA].

[81] J. F. Navarro, C. S. Frenk, and S. D. M. White, "A Universal density profile from hierarchical clustering," *Astrophys. J.* **490** (1997) 493–508, arXiv:astro-ph/9611107 [astro-ph].

[82] J. F. Navarro, A. Ludlow, V. Springel, J. Wang, M. Vogelsberger, S. D. M. White, A. Jenkins, C. S. Frenk, and A. Helmi, "The Diversity and Similarity of Cold Dark Matter Halos," *Mon. Not. Roy. Astron. Soc.* **402** (2010) 21, arXiv:0810.1522 [astro-ph].

[83] S. S. McGaugh, V. C. Rubin, and W. J. G. de Blok, "High - resolution rotation curves of low surface brightness galaxies: Data," *Astron. J.* **122** (2001) 2381–2395, arXiv:astro-ph/0107326 [astro-ph].

[84] R. Kuzio de Naray, S. S. McGaugh, and W. J. G. de Blok, "Mass Models for Low Surface Brightness Galaxies with High Resolution Optical Velocity Fields," *Astrophys. J.* **676** (2008) 920–943, arXiv:0712.0860 [astro-ph].

[85] M. G. Walker, M. Mateo, E. W. Olszewski, J. Penarrubia, N. W. Evans, and G. Gilmore, "A Universal Mass Profile for Dwarf Spheroidal Galaxies," *Astrophys. J.* **704** (2009) 1274–1287, arXiv:0906.0341 [astro-ph.CO]. [Erratum: Astrophys. J.710,886(2010)].

[86] J. Wolf, G. D. Martinez, J. S. Bullock, M. Kaplinghat, M. Geha, R. R. Munoz, J. D. Simon, and F. F. Avedo, "Accurate Masses for Dispersion-supported Galaxies," *Mon. Not. Roy. Astron. Soc.* **406** (2010) 1220, arXiv:0908.2995 [astro-ph.CO].

[87] E. J. Tollerud, M. Boylan-Kolchin, and J. S. Bullock, "M31 Satellite Masses Compared to LCDM Subhaloes," *Mon. Not. Roy. Astron. Soc.* **440** no. 4, (2014) 3511–3519, arXiv:1403.6469 [astro-ph.GA].

[88] E. N. Kirby, J. S. Bullock, M. Boylan-Kolchin, M. Kaplinghat, and J. G. Cohen, "The dynamics of isolated Local Group galaxies," *Mon. Not. Roy. Astron. Soc.* **439** no. 1, (2014) 1015–1027, arXiv:1401.1208 [astro-ph.GA].

[89] A. Pontzen and F. Governato, "How supernova feedback turns dark matter cusps into cores," *Mon. Not. Roy. Astron. Soc.* **421** (2012) 3464, arXiv:1106.0499 [astro-ph.CO].

[90] A. G. Riess *et al.*, "A 2.4% Determination of the Local Value of the Hubble Constant," *Astrophys. J.* **826** no. 1, (2016) 56, arXiv:1604.01424 [astro-ph.CO].

[91] B. A. Reid *et al.*, "Cosmological Constraints from the Clustering of the Sloan Digital Sky Survey DR7 Luminous Red Galaxies," *Mon. Not. Roy. Astron. Soc.* **404** (2010) 60–85, arXiv:0907.1659 [astro-ph.CO].

[92] C. Heymans *et al.*, "CFHTLenS tomographic weak lensing cosmological parameter constraints: Mitigating the impact of intrinsic galaxy alignments," *Mon. Not. Roy. Astron. Soc.* **432** (2013) 2433, arXiv:1303.1808 [astro-ph.CO].

[93] **Planck** Collaboration, P. A. R. Ade *et al.*, "Planck 2013 results. XX. Cosmology from Sunyaev–Zeldovich cluster counts," *Astron. Astrophys.* **571** (2014) A20, arXiv:1303.5080 [astro-ph.CO].

[94] P. Gondolo and G. Gelmini, "Cosmic abundances of stable particles: Improved analysis," *Nucl. Phys.* **B360** (1991) 145–179.

[95] L. J. Hall, K. Jedamzik, J. March-Russell, and S. M. West, "Freeze-In Production of FIMP Dark Matter," *JHEP* **03** (2010) 080, arXiv:0911.1120 [hep-ph].

[96] N. Bernal, M. Heikinheimo, T. Tenkanen, K. Tuominen, and V. Vaskonen, "The Dawn of FIMP Dark Matter: A Review of Models and Constraints," *Int. J. Mod. Phys.* **A32** no. 27, (2017) 1730023, arXiv:1706.07442 [hep-ph].

[97] H. Baer, K.-Y. Choi, J. E. Kim, and L. Roszkowski, "Dark matter production in the early Universe: beyond the thermal WIMP paradigm," *Phys. Rept.* **555** (2015) 1–60, arXiv:1407.0017 [hep-ph].

[98] J. Lesgourgues and S. Pastor, "Neutrino mass from Cosmology," *Adv. High Energy Phys.* **2012** (2012) 608515, arXiv:1212.6154 [hep-ph].

[99] O. Just, "The Partial Wave Formalism and its Application to Neutralino Dark Matter," Master's thesis, Technical University of Munich, 2008.

[100] G. Steigman, B. Dasgupta, and J. F. Beacom, "Precise Relic WIMP Abundance and its Impact on Searches for Dark Matter Annihilation," *Phys. Rev.* **D86** (2012) 023506, arXiv:1204.3622 [hep-ph].

[101] H. T. Ihle, "Late Kinetic Decoupling of Dark Matter," Master's thesis, University of Oslo, 2016.

[102] P. Binetruy, G. Girardi, and P. Salati, "Constraints on a System of Two Neutral Fermions From Cosmology," *Nucl. Phys.* **B237** (1984) 285–306.

[103] J. Edsjö, M. Schelke, P. Ullio, and P. Gondolo, "Accurate relic densities with neutralino, chargino and sfermion coannihilations in mSUGRA," *JCAP* **0304** (2003) 001, arXiv:hep-ph/0301106 [hep-ph].

[104] K. Griest and D. Seckel, "Three exceptions in the calculation of relic abundances," *Phys. Rev.* **D43** (1991) 3191–3203.

[105] J. Edsjö and P. Gondolo, "Neutralino relic density including coannihilations," *Phys. Rev.* **D56** (1997) 1879–1894, arXiv:hep-ph/9704361 [hep-ph].

[106] S. Profumo and A. Provenza, "Increasing the neutralino relic abundance with slepton coannihilations: Consequences for indirect dark matter detection," *JCAP* **0612** (2006) 019, arXiv:hep-ph/0609290 [hep-ph].

[107] N. Arkani-Hamed, A. Delgado, and G. F. Giudice, "The Well-tempered neutralino," *Nucl. Phys.* **B741** (2006) 108–130, arXiv:hep-ph/0601041 [hep-ph].

[108] T. Binder, T. Bringmann, M. Gustafsson, and A. Hryczuk, "Dark Matter Relic Density Revisited: The Case For Early Kinetic Decoupling," in *53rd Rencontres de Moriond on Electroweak Interactions and Unified Theories (Moriond EW 2018) La Thuile, Italy, March 10-17, 2018*. 2018. arXiv:1805.00526 [hep-ph]. https://inspirehep.net/record/1671095/files/1805.00526.pdf.

[109] E. Bertschinger, "The Effects of Cold Dark Matter Decoupling and Pair Annihilation on Cosmological Perturbations," *Phys. Rev.* **D74** (2006) 063509, arXiv:astro-ph/0607319 [astro-ph].

[110] T. Bringmann and S. Hofmann, "Thermal decoupling of WIMPs from first principles," *JCAP* **0704** (2007) 016, arXiv:hep-ph/0612238 [hep-ph]. [Erratum: JCAP1603,no.03,E02(2016)].

[111] J. Kasahara, *Neutralino Dark Matter: The Mass of the smallest Halo and the golden Region*. PhD thesis, University of Utah, 2009.

[112] C. Boehm, P. Fayet, and R. Schaeffer, "Constraining dark matter candidates from structure formation," *Phys. Lett.* **B518** (2001) 8–14, arXiv:astro-ph/0012504 [astro-ph].

[113] S. Hofmann, D. J. Schwarz, and H. Stoecker, "Damping scales of neutralino cold dark matter," *Phys. Rev.* **D64** (2001) 083507, arXiv:astro-ph/0104173 [astro-ph].

[114] C. Boehm and R. Schaeffer, "Constraints on dark matter interactions from structure formation: Damping lengths," *Astron. Astrophys.* **438** (2005) 419–442, arXiv:astro-ph/0410591 [astro-ph].

[115] T. Bringmann, "Particle Models and the Small-Scale Structure of Dark Matter," *New J. Phys.* **11** (2009) 105027, arXiv:0903.0189 [astro-ph.CO].

[116] M. Vogelsberger, J. Zavala, F.-Y. Cyr-Racine, C. Pfrommer, T. Bringmann, and K. Sigurdson, "ETHOS ? an effective theory of structure formation: dark matter physics as a possible explanation of the small-scale CDM problems," *Mon. Not. Roy. Astron. Soc.* **460** no. 2, (2016) 1399–1416, arXiv:1512.05349 [astro-ph.CO].

[117] S. D. M. White, M. Davis, and C. S. Frenk, "The size of clusters in a neutrino-dominated universe," *Monthly Notices of the Royal Astronomical Society* **209** no. 1, (1984) 27P–31P. http://dx.doi.org/10.1093/mnras/209.1.27P.

[118] M. Drees, G. Jungman, M. Kamionkowski, and M. M. Nojiri, "Neutralino annihilation into gluons," *Phys. Rev.* **D49** (1994) 636–647, arXiv:hep-ph/9306325 [hep-ph].

[119] B. Herrmann and M. Klasen, "SUSY-QCD Corrections to Dark Matter Annihilation in the Higgs Funnel," *Phys. Rev.* **D76** (2007) 117704, arXiv:0709.0043 [hep-ph].

[120] A. Freitas, "Radiative corrections to co-annihilation processes," *Phys. Lett.* **B652** (2007) 280–284, arXiv:0705.4027 [hep-ph].

[121] K. Kovarik and B. Herrmann, "SUSY-QCD corrections to dark matter annihilations," *AIP Conf. Proc.* **1200** (2010) 1075–1078, arXiv:0910.0941 [hep-ph].

[122] B. Herrmann, M. Klasen, and K. Kovarik, "Neutralino Annihilation into Massive Quarks with SUSY-QCD Corrections," *Phys. Rev.* **D79** (2009) 061701, arXiv:0901.0481 [hep-ph].

[123] F. Boudjema, G. Drieu La Rochelle, and S. Kulkarni, "One-loop corrections, uncertainties and approximations in neutralino annihilations: Examples," *Phys. Rev.* **D84** (2011) 116001, arXiv:1108.4291 [hep-ph].

[124] A. Chatterjee, M. Drees, and S. Kulkarni, "Radiative Corrections to the Neutralino Dark Matter Relic Density - an Effective Coupling Approach," *Phys. Rev.* **D86** (2012) 105025, arXiv:1209.2328 [hep-ph].

[125] B. Herrmann, M. Klasen, K. Kovarik, M. Meinecke, and P. Steppeler, "One-loop corrections to gaugino (co)annihilation into quarks in the MSSM," *Phys. Rev.* **D89** no. 11, (2014) 114012, arXiv:1404.2931 [hep-ph].

[126] J. Harz, B. Herrmann, M. Klasen, K. Kovarik, and P. Steppeler, "Theoretical uncertainty of the supersymmetric dark matter relic density from scheme and scale variations," *Phys. Rev.* **D93** no. 11, (2016) 114023, arXiv:1602.08103 [hep-ph].

[127] A. Djouadi, O. Lebedev, Y. Mambrini, and J. Quevillon, "Implications of LHC searches for Higgs–portal dark matter," *Phys. Lett.* **B709** (2012) 65–69, arXiv:1112.3299 [hep-ph].

[128] A. De Simone, G. F. Giudice, and A. Strumia, "Benchmarks for Dark Matter Searches at the LHC," *JHEP* **06** (2014) 081, arXiv:1402.6287 [hep-ph].

[129] J. Kearney, N. Orlofsky, and A. Pierce, "Z boson mediated dark matter beyond the effective theory," *Phys. Rev.* **D95** no. 3, (2017) 035020, arXiv:1611.05048 [hep-ph].

[130] R. Haag, J. T. Lopuszanski, and M. Sohnius, "All Possible Generators of Supersymmetries of the s Matrix," *Nucl. Phys.* **B88** (1975) 257. [,257(1974)].

[131] P. Fayet and S. Ferrara, "Supersymmetry," *Phys. Rept.* **32** (1977) 249–334.

[132] S. Colucci, F. Giacchino, M. H. G. Tytgat, and J. Vandecasteele, "On Radiative Corrections to Vector-like Portal Dark Matter," arXiv:1805.10173 [hep-ph].

[133] P. Fayet, "Supersymmetry and Weak, Electromagnetic and Strong Interactions," *Phys. Lett.* **64B** (1976) 159.

[134] P. Fayet, "Spontaneously Broken Supersymmetric Theories of Weak, Electromagnetic and Strong Interactions," *Phys. Lett.* **69B** (1977) 489.

[135] P. Fayet, "Relations Between the Masses of the Superpartners of Leptons and Quarks, the Goldstino Couplings and the Neutral Currents," *Phys. Lett.* **84B** (1979) 416.

[136] H. E. Haber and G. L. Kane, "The Search for Supersymmetry: Probing Physics Beyond the Standard Model," *Phys. Rept.* **117** (1985) 75–263.

[137] H. Muller-Kirsten and A. Wiedemann, *Introduction to Supersymmetry*. World Scientific lecture notes in physics. World Scientific, 2010. https://books.google.no/books?id=RU-hsrWp9isC.

[138] S. P. Martin, "A Supersymmetry primer," arXiv:hep-ph/9709356 [hep-ph]. [Adv. Ser. Direct. High Energy Phys.18,1(1998)].

[139] P. Binetruy, *Supersymmetry:Theory, Experiment, and Cosmology: Theory, Experiment, and Cosmology*. Oxford Graduate Texts. OUP Oxford, 2006. https://books.google.no/books?id=StDjdRnT72AC.

[140] **ATLAS** Collaboration, G. Aad *et al.*, "Observation of a new particle in the search for the Standard Model Higgs boson with the ATLAS detector at the LHC," *Phys. Lett.* **B716** (2012) 1–29, arXiv:1207.7214 [hep-ex].

[141] **CMS** Collaboration, S. Chatrchyan *et al.*, "Observation of a new boson at a mass of 125 GeV with the CMS experiment at the LHC," *Phys. Lett.* **B716** (2012) 30–61, arXiv:1207.7235 [hep-ex].

[142] P. Bechtle, S. Heinemeyer, O. Stål, T. Stefaniak, G. Weiglein, and L. Zeune, "MSSM Interpretations of the LHC Discovery: Light or Heavy Higgs?," *Eur. Phys. J.* **C73** no. 4, (2013) 2354, arXiv:1211.1955 [hep-ph].

[143] M. Carena, S. Heinemeyer, O. Stål, C. E. M. Wagner, and G. Weiglein, "MSSM Higgs Boson Searches at the LHC: Benchmark Scenarios after the Discovery of a Higgs-like Particle," *Eur. Phys. J.* **C73** no. 9, (2013) 2552, arXiv:1302.7033 [hep-ph].

[144] R. Barbier *et al.*, "R-parity violating supersymmetry," *Phys. Rept.* **420** (2005) 1–202, arXiv:hep-ph/0406039 [hep-ph].

[145] H. Goldberg, "Constraint on the Photino Mass from Cosmology," *Phys. Rev. Lett.* **50** (1983) 1419. [,219(1983)].

[146] J. R. Ellis, J. S. Hagelin, D. V. Nanopoulos, K. A. Olive, and M. Srednicki, "Supersymmetric Relics from the Big Bang," *Nucl. Phys.* **B238** (1984) 453–476. [,223(1983)].

[147] T. Bringmann, F. Calore, A. Galea, and M. Garny, "Electroweak and Higgs Boson Internal Bremsstrahlung: General considerations for Majorana dark matter annihilation and application to MSSM neutralinos," *JHEP* **09** (2017) 041, arXiv:1705.03466 [hep-ph].

[148] C. Strege, G. Bertone, G. J. Besjes, S. Caron, R. Ruiz de Austri, A. Strubig, and R. Trotta, "Profile likelihood maps of a 15-dimensional MSSM," *JHEP* **09** (2014) 081, arXiv:1405.0622 [hep-ph].

[149] K. J. de Vries *et al.*, "The pMSSM10 after LHC Run 1," *Eur. Phys. J.* **C75** no. 9, (2015) 422, arXiv:1504.03260 [hep-ph].

[150] **ATLAS** Collaboration, G. Aad *et al.*, "Summary of the ATLAS experiment?s sensitivity to supersymmetry after LHC Run 1 ? interpreted in the phenomenological MSSM," *JHEP* **10** (2015) 134, arXiv:1508.06608 [hep-ex].

[151] **GAMBIT** Collaboration, P. Athron *et al.*, "Global fits of GUT-scale SUSY models with GAMBIT," *Eur. Phys. J.* **C77** no. 12, (2017) 824, arXiv:1705.07935 [hep-ph].

[152] M. Drees and M. M. Nojiri, "The Neutralino relic density in minimal $N = 1$ supergravity," *Phys. Rev.* **D47** (1993) 376–408, arXiv:hep-ph/9207234 [hep-ph].

[153] L. Bergstr"om, "Radiative Processes in Dark Matter Photino Annihilation," *Phys. Lett.* **B225** (1989) 372–380.

[154] R. Flores, K. A. Olive, and S. Rudaz, "Radiative Processes in Lsp Annihilation," *Phys. Lett.* **B232** (1989) 377–382.

[155] T. Bringmann, L. Bergstr"om, and J. Edsjö, "New Gamma-Ray Contributions to Supersymmetric Dark Matter Annihilation," *JHEP* **01** (2008) 049, arXiv:0710.3169 [hep-ph].

[156] P. Ciafaloni, M. Cirelli, D. Comelli, A. De Simone, A. Riotto, and A. Urbano, "On the Importance of Electroweak Corrections for Majorana Dark Matter Indirect Detection," *JCAP* **1106** (2011) 018, arXiv:1104.2996 [hep-ph].

[157] L. Bergstr"om, T. Bringmann, and J. Edsjö, "New Positron Spectral Features from Supersymmetric Dark Matter - a Way to Explain the PAMELA Data?," *Phys. Rev.* **D78** (2008) 103520, arXiv:0808.3725 [astro-ph].

[158] T. Bringmann, X. Huang, A. Ibarra, S. Vogl, and C. Weniger, "Fermi LAT Search for Internal Bremsstrahlung Signatures from Dark Matter Annihilation," *JCAP* **1207** (2012) 054, arXiv:1203.1312 [hep-ph].

[159] F. Calore, *Unveiling Dark Matter through Gamma Rays: Spectral Features, Spatial Signatures and Astrophysical Backgrounds*. PhD thesis, Hamburg U., Inst. Theor. Phys. II, 2013. https://inspirehep.net/record/1291594/files/Dissertation.pdf.

[160] M. Cahill-Rowley, R. Cotta, A. Drlica-Wagner, S. Funk, J. Hewett, A. Ismail, T. Rizzo, and M. Wood, "Complementarity of dark matter searches in the phenomenological MSSM," *Phys. Rev.* **D91** no. 5, (2015) 055011, arXiv:1405.6716 [hep-ph].

[161] E. Braaten and J. P. Leveille, "Higgs-boson decay and the running mass," *Phys. Rev. D* **22** (Aug, 1980) 715–721. https://link.aps.org/doi/10.1103/PhysRevD.22.715.

[162] M. Drees and K.-i. Hikasa, "NOTE ON QCD CORRECTIONS TO HADRONIC HIGGS DECAY," *Phys. Lett.* **B240** (1990) 455. [Erratum: Phys. Lett.B262,497(1991)].

[163] T. Bringmann, J. Edsjö, P. Gondolo, P. Ullio, and L. Bergström, "DarkSUSY 6 : An Advanced Tool to Compute Dark Matter Properties Numerically," arXiv:1802.03399 [hep-ph].

[164] C. Boehm, A. Djouadi, and M. Drees, "Light scalar top quarks and supersymmetric dark matter," *Phys. Rev.* **D62** (2000) 035012, arXiv:hep-ph/9911496 [hep-ph].

[165] J. R. Ellis, K. A. Olive, and Y. Santoso, "Calculations of neutralino stop coannihilation in the CMSSM," *Astropart. Phys.* **18** (2003) 395–432, arXiv:hep-ph/0112113 [hep-ph].

[166] V. A. Bednyakov, H. V. Klapdor-Kleingrothaus, and V. Gronewold, "Squark, slepton and neutralino chargino coannihilation effects in the low-energy effective MSSM," *Phys. Rev.* **D66** (2002) 115005, arXiv:hep-ph/0208178 [hep-ph].

[167] Y. Santoso, "Neutralino stop coannihilation in the CMSSM," *Nucl. Phys. Proc. Suppl.* **124** (2003) 166–169, arXiv:hep-ph/0205026 [hep-ph]. [,166(2002)].

[168] H. Baer, C. Balazs, and A. Belyaev, "Neutralino relic density in minimal supergravity with coannihilations," *JHEP* **03** (2002) 042, arXiv:hep-ph/0202076 [hep-ph].

[169] M. A. Ajaib, T. Li, and Q. Shafi, "Stop-Neutralino Coannihilation in the Light of LHC," *Phys. Rev.* **D85** (2012) 055021, arXiv:1111.4467 [hep-ph].

[170] J. L. Diaz-Cruz, J. R. Ellis, K. A. Olive, and Y. Santoso, "On the Feasibility of a Stop NLSP in Gravitino Dark Matter Scenarios," *JHEP* **05** (2007) 003, arXiv:hep-ph/0701229 [HEP-PH].

[171] K. Huitu, L. Leinonen, and J. Laamanen, "Stop as a next-to-lightest supersymmetric particle in constrained MSSM," *Phys. Rev.* **D84** (2011) 075021, arXiv:1107.2128 [hep-ph].

[172] J. Ellis, K. A. Olive, and J. Zheng, "The Extent of the Stop Coannihilation Strip," *Eur. Phys. J.* **C74** (2014) 2947, arXiv:1404.5571 [hep-ph].

[173] A. Ibarra, A. Pierce, N. R. Shah, and S. Vogl, "Anatomy of Coannihilation with a Scalar Top Partner," *Phys. Rev.* **D91** no. 9, (2015) 095018, arXiv:1501.03164 [hep-ph].

[174] O. Adriani *et al.*, "Measurement of the flux of primary cosmic ray antiprotons with energies of 60-MeV to 350-GeV in the PAMELA experiment," *JETP Lett.* **96** (2013) 621–627. [Pisma Zh. Eksp. Teor. Fiz.96,693(2012)].

[175] A. Burkert, "The Structure and evolution of weakly selfinteracting cold dark matter halos," *Astrophys. J.* **534** (2000) L143–L146, arXiv:astro-ph/0002409 [astro-ph].

[176] R. Davé, D. N. Spergel, P. J. Steinhardt, and B. D. Wandelt, "Halo properties in cosmological simulations of selfinteracting cold dark matter," *Astrophys. J.* **547** (2001) 574–589, arXiv:astro-ph/0006218 [astro-ph].

[177] M. Vogelsberger, J. Zavala, and A. Loeb, "Subhaloes in Self-Interacting Galactic Dark Matter Haloes," *Mon. Not. Roy. Astron. Soc.* **423** (2012) 3740, arXiv:1201.5892 [astro-ph.CO].

[178] M. Rocha, A. H. G. Peter, J. S. Bullock, M. Kaplinghat, S. Garrison-Kimmel, J. Onorbe, and L. A. Moustakas, "Cosmological Simulations with Self-Interacting Dark Matter I: Constant Density Cores and Substructure," *Mon. Not. Roy. Astron. Soc.* **430** (2013) 81–104, arXiv:1208.3025 [astro-ph.CO].

[179] C. Boehm, A. Riazuelo, S. H. Hansen, and R. Schaeffer, "Interacting dark matter disguised as warm dark matter," *Phys. Rev.* **D66** (2002) 083505, arXiv:astro-ph/0112522 [astro-ph].

[180] D. Hooper, M. Kaplinghat, L. E. Strigari, and K. M. Zurek, "MeV Dark Matter and Small Scale Structure," *Phys. Rev.* **D76** (2007) 103515, arXiv:0704.2558 [astro-ph].

[181] L. G. van den Aarssen, T. Bringmann, and C. Pfrommer, "Is dark matter with long-range interactions a solution to all small-scale problems of Λ CDM cosmology?," *Phys. Rev. Lett.* **109** (2012) 231301, arXiv:1205.5809 [astro-ph.CO].

[182] C. Boehm, J. A. Schewtschenko, R. J. Wilkinson, C. M. Baugh, and S. Pascoli, "Using the Milky Way satellites to study interactions between cold dark matter and radiation," *Mon. Not. Roy. Astron. Soc.* **445** (2014) L31–L35, arXiv:1404.7012 [astro-ph.CO].

[183] X.-l. Chen, M. Kamionkowski, and X.-m. Zhang, "Kinetic decoupling of neutralino dark matter," *Phys. Rev.* **D64** (2001) 021302, arXiv:astro-ph/0103452 [astro-ph].

[184] T. Bringmann, J. Hasenkamp, and J. Kersten, "Tight bonds between sterile neutrinos and dark matter," *JCAP* **1407** (2014) 042, arXiv:1312.4947 [hep-ph].

[185] B. Dasgupta and J. Kopp, "Cosmologically Safe eV-Scale Sterile Neutrinos and Improved Dark Matter Structure," *Phys. Rev. Lett.* **112** no. 3, (2014) 031803, arXiv:1310.6337 [hep-ph].

[186] X. Chu and B. Dasgupta, "Dark Radiation Alleviates Problems with Dark Matter Halos," *Phys. Rev. Lett.* **113** no. 16, (2014) 161301, arXiv:1404.6127 [hep-ph].

[187] P. Ko and Y. Tang, "$\nu\Lambda$MDM: A model for sterile neutrino and dark matter reconciles cosmological and neutrino oscillation data after BICEP2," *Phys. Lett.* **B739** (2014) 62–67, arXiv:1404.0236 [hep-ph].

[188] T. Binder, L. Covi, A. Kamada, H. Murayama, T. Takahashi, and N. Yoshida, "Matter Power Spectrum in Hidden Neutrino Interacting Dark Matter Models: A Closer Look at the Collision Term," *JCAP* **1611** (2016) 043, arXiv:1602.07624 [hep-ph].

[189] J. Zavala, M. Vogelsberger, and M. G. Walker, "Constraining Self-Interacting Dark Matter with the Milky Way's dwarf spheroidals,"

Mon. Not. Roy. Astron. Soc. **431** (2013) L20–L24, arXiv:1211.6426 [astro-ph.CO].

[190] A. H. G. Peter, M. Rocha, J. S. Bullock, and M. Kaplinghat, "Cosmological Simulations with Self-Interacting Dark Matter II: Halo Shapes vs. Observations," *Mon. Not. Roy. Astron. Soc.* **430** (2013) 105, arXiv:1208.3026 [astro-ph.CO].

[191] M. Kaplinghat, S. Tulin, and H.-B. Yu, "Dark Matter Halos as Particle Colliders: Unified Solution to Small-Scale Structure Puzzles from Dwarfs to Clusters," *Phys. Rev. Lett.* **116** no. 4, (2016) 041302, arXiv:1508.03339 [astro-ph.CO].

[192] A. Loeb and N. Weiner, "Cores in Dwarf Galaxies from Dark Matter with a Yukawa Potential," *Phys. Rev. Lett.* **106** (2011) 171302, arXiv:1011.6374 [astro-ph.CO].

[193] M. Pospelov, A. Ritz, and M. B. Voloshin, "Secluded WIMP Dark Matter," *Phys. Lett.* **B662** (2008) 53–61, arXiv:0711.4866 [hep-ph].

[194] M. Kaplinghat, S. Tulin, and H.-B. Yu, "Direct Detection Portals for Self-interacting Dark Matter," *Phys. Rev.* **D89** no. 3, (2014) 035009, arXiv:1310.7945 [hep-ph].

[195] E. Del Nobile, M. Kaplinghat, and H.-B. Yu, "Direct Detection Signatures of Self-Interacting Dark Matter with a Light Mediator," *JCAP* **1510** no. 10, (2015) 055, arXiv:1507.04007 [hep-ph].

[196] A. Sommerfeld, "Über die Beugung und Bremsung der Elektronen," *Annalen der Physik* **403** (1931) 207.

[197] N. Arkani-Hamed, D. P. Finkbeiner, T. R. Slatyer, and N. Weiner, "A Theory of Dark Matter," *Phys. Rev.* **D79** (2009) 015014, arXiv:0810.0713 [hep-ph].

[198] S. Cassel, "Sommerfeld factor for arbitrary partial wave processes," *J. Phys.* **G37** (2010) 105009, arXiv:0903.5307 [hep-ph].

[199] R. Iengo, "Sommerfeld enhancement: General results from field theory diagrams," *JHEP* **05** (2009) 024, arXiv:0902.0688 [hep-ph].

[200] T. R. Slatyer, "The Sommerfeld enhancement for dark matter with an excited state," *JCAP* **1002** (2010) 028, arXiv:0910.5713 [hep-ph].

[201] K. Blum, R. Sato, and T. R. Slatyer, "Self-consistent Calculation of the Sommerfeld Enhancement," *JCAP* **1606** no. 06, (2016) 021, arXiv:1603.01383 [hep-ph].

[202] S. Tulin, H.-B. Yu, and K. M. Zurek, "Beyond Collisionless Dark Matter: Particle Physics Dynamics for Dark Matter Halo Structure," *Phys. Rev.* **D87** no. 11, (2013) 115007, arXiv:1302.3898 [hep-ph].

[203] J. B. Dent, S. Dutta, and R. J. Scherrer, "Thermal Relic Abundances of Particles with Velocity-Dependent Interactions," *Phys. Lett.* **B687** (2010) 275–279, arXiv:0909.4128 [astro-ph.CO].

[204] J. Zavala, M. Vogelsberger, and S. D. M. White, "Relic density and CMB constraints on dark matter annihilation with Sommerfeld enhancement," *Phys. Rev.* **D81** (2010) 083502, arXiv:0910.5221 [astro-ph.CO].

[205] J. L. Feng, M. Kaplinghat, and H.-B. Yu, "Sommerfeld Enhancements for Thermal Relic Dark Matter," *Phys. Rev.* **D82** (2010) 083525, arXiv:1005.4678 [hep-ph].

[206] B. von Harling and K. Petraki, "Bound-state formation for thermal relic dark matter and unitarity," *JCAP* **1412** (2014) 033, arXiv:1407.7874 [hep-ph].

[207] M. Cirelli, P. Panci, K. Petraki, F. Sala, and M. Taoso, "Dark Matter's secret liaisons: phenomenology of a dark U(1) sector with bound states," *JCAP* **1705** no. 05, (2017) 036, arXiv:1612.07295 [hep-ph].

[208] **Fermi-LAT** Collaboration, M. Ackermann *et al.*, "Searching for Dark Matter Annihilation from Milky Way Dwarf Spheroidal Galaxies with Six Years of Fermi Large Area Telescope Data," *Phys. Rev. Lett.* **115** no. 23, (2015) 231301, arXiv:1503.02641 [astro-ph.HE].

[209] **AMS** Collaboration, L. Accardo *et al.*, "High Statistics Measurement of the Positron Fraction in Primary Cosmic Rays of 0.5?500 GeV with the Alpha Magnetic Spectrometer on the International Space Station," *Phys. Rev. Lett.* **113** (2014) 121101.

[210] **AMS** Collaboration, M. Aguilar *et al.*, "Electron and Positron Fluxes in Primary Cosmic Rays Measured with the Alpha Magnetic Spectrometer on the International Space Station," *Phys. Rev. Lett.* **113** (2014) 121102.

[211] X.-L. Chen and M. Kamionkowski, "Particle decays during the cosmic dark ages," *Phys. Rev.* **D70** (2004) 043502, arXiv:astro-ph/0310473 [astro-ph].

[212] N. Padmanabhan and D. P. Finkbeiner, "Detecting dark matter annihilation with CMB polarization: Signatures and experimental prospects," *Phys. Rev.* **D72** (2005) 023508, arXiv:astro-ph/0503486 [astro-ph].

[213] M. Valdes, C. Evoli, and A. Ferrara, "Particle energy cascade in the Intergalactic Medium," *Mon. Not. Roy. Astron. Soc.* **404** (2010) 1569–1582, arXiv:0911.1125 [astro-ph.CO].

[214] G. Hutsi, J. Chluba, A. Hektor, and M. Raidal, "WMAP7 and future CMB constraints on annihilating dark matter: implications on GeV-scale WIMPs," *Astron. Astrophys.* **535** (2011) A26, arXiv:1103.2766 [astro-ph.CO].

[215] T. R. Slatyer, "Indirect dark matter signatures in the cosmic dark ages. I. Generalizing the bound on s-wave dark matter annihilation from Planck results," *Phys. Rev.* **D93** no. 2, (2016) 023527, arXiv:1506.03811 [hep-ph].

[216] F.-Y. Cyr-Racine, K. Sigurdson, J. Zavala, T. Bringmann, M. Vogelsberger, and C. Pfrommer, "ETHOS?an effective theory of structure formation: From dark particle physics to the matter distribution of the Universe," *Phys. Rev.* **D93** no. 12, (2016) 123527, arXiv:1512.05344 [astro-ph.CO].

[217] J. L. Feng, M. Kaplinghat, and H.-B. Yu, "Halo Shape and Relic Density Exclusions of Sommerfeld-Enhanced Dark Matter Explanations of Cosmic Ray Excesses," *Phys. Rev. Lett.* **104** (2010) 151301, arXiv:0911.0422 [hep-ph].

[218] S. A. Khrapak, A. V. Ivlev, G. E. Morfill, and S. K. Zhdanov, "Scattering in the Attractive Yukawa Potential in the Limit of Strong Interaction," *Phys. Rev. Lett.* **90** (June, 2003) 225002.

[219] A. V. Maccio and F. Fontanot, "How cold is Dark Matter? Constraints from Milky Way Satellites," *Mon. Not. Roy. Astron. Soc.* **404** (2010) 16, arXiv:0910.2460 [astro-ph.CO].

[220] D. Feldman, B. Kors, and P. Nath, "Extra-weakly Interacting Dark Matter," *Phys. Rev.* **D75** (2007) 023503, arXiv:hep-ph/0610133 [hep-ph].

[221] M. T. Frandsen, F. Kahlhoefer, S. Sarkar, and K. Schmidt-Hoberg, "Direct detection of dark matter in models with a light Z'," *JHEP* **09** (2011) 128, arXiv:1107.2118 [hep-ph].

[222] X. Chu, C. Garcia-Cely, and T. Hambye, "Can the relic density of self-interacting dark matter be due to annihilations into Standard Model particles?," *JHEP* **11** (2016) 048, arXiv:1609.00399 [hep-ph].

[223] G. Elor, N. L. Rodd, T. R. Slatyer, and W. Xue, "Model-Independent Indirect Detection Constraints on Hidden Sector Dark Matter," *JCAP* **1606** no. 06, (2016) 024, arXiv:1511.08787 [hep-ph].

[224] J. Redondo and M. Postma, "Massive hidden photons as lukewarm dark matter," *JCAP* **0902** (2009) 005, arXiv:0811.0326 [hep-ph].

[225] J. F. Cherry, A. Friedland, and I. M. Shoemaker, "Neutrino Portal Dark Matter: From Dwarf Galaxies to IceCube," arXiv:1411.1071 [hep-ph].

[226] T. R. Slatyer and C.-L. Wu, "General Constraints on Dark Matter Decay from the Cosmic Microwave Background," *Phys. Rev.* **D95** no. 2, (2017) 023010, arXiv:1610.06933 [astro-ph.CO].

[227] A. Lewis, A. Challinor, and A. Lasenby, "Efficient computation of CMB anisotropies in closed FRW models," *Astrophys. J.* **538** (2000) 473–476, arXiv:astro-ph/9911177 [astro-ph].

[228] **Planck** Collaboration, N. Aghanim *et al.*, "Planck 2015 results. XI. CMB power spectra, likelihoods, and robustness of parameters," *Astron. Astrophys.* **594** (2016) A11, arXiv:1507.02704 [astro-ph.CO].

[229] C. Howlett, A. Lewis, A. Hall, and A. Challinor, "CMB power spectrum parameter degeneracies in the era of precision cosmology," *JCAP* **1204** (2012) 027, arXiv:1201.3654 [astro-ph.CO].

[230] A. Lewis and S. Bridle, "Cosmological parameters from CMB and other data: A Monte Carlo approach," *Phys. Rev.* **D66** (2002) 103511, arXiv:astro-ph/0205436 [astro-ph].

[231] A. Lewis, "Efficient sampling of fast and slow cosmological parameters," *Phys. Rev.* **D87** (2013) 103529, arXiv:1304.4473 [astro-ph.CO].

[232] A. Gelman and D. B. Rubin, "Inference from Iterative Simulation Using Multiple Sequences," *Statist. Sci.* **7** (1992) 457–472.

[233] A. Lewis, "GetDist Notes." https://cosmologist.info/notes/GetDist.pdf.

[234] S. Gariazzo, M. Archidiacono, P. F. de Salas, O. Mena, C. A. Ternes, and M. Tórtola, "Neutrino masses and their ordering: Global Data, Priors and Models," *JCAP* **1803** no. 03, (2018) 011, arXiv:1801.04946 [hep-ph].

[235] M. A. Buen-Abad, M. Schmaltz, J. Lesgourgues, and T. Brinckmann, "Interacting Dark Sector and Precision Cosmology," *JCAP* **1801** no. 01, (2018) 008, arXiv:1708.09406 [astro-ph.CO].

[236] T. Nakamura, M. Sasaki, T. Tanaka, and K. S. Thorne, "Gravitational waves from coalescing black hole MACHO binaries," *Astrophys. J.* **487** (1997) L139–L142, arXiv:astro-ph/9708060 [astro-ph].

[237] M. Raidal, V. Vaskonen, and H. Veermae, "Gravitational Waves from Primordial Black Hole Mergers," *JCAP* **1709** (2017) 037, arXiv:1707.01480 [astro-ph.CO].

[238] C. Armendariz-Picon and J. T. Neelakanta, "Structure Formation Constraints on Sommerfeld-Enhanced Dark Matter Annihilation," *JCAP* **1212** (2012) 009, arXiv:1210.3017 [astro-ph.CO].

[239] R. Huo, M. Kaplinghat, Z. Pan, and H.-B. Yu, "Signatures of Self-Interacting Dark Matter in the Matter Power Spectrum and the CMB," arXiv:1709.09717 [hep-ph].

[240] T. Binder, M. Gustafsson, A. Kamada, S. M. R. Sandner, and M. Wiesner, "Reannihilation of self-interacting dark matter," arXiv:1712.01246 [astro-ph.CO].

Part V

Papers

Paper I

Leading QCD Corrections for Indirect Dark Matter Searches: a Fresh Look

Paper II

Suppressing structure formation at dwarf galaxy scales and below: late kinetic decoupling as a compelling alternative to warm dark matter

Paper III

Strong constraints on self-interacting dark matter with light mediators

Paper IV

Converting non-relativistic dark matter to radiation